5-14-2023

Advanced Manufacturing of Multilayer Ceramic Composites for Application in Solid Oxide Fuel Cells

Alexander Ryan Hartwell
Syracuse University

Abstract

This thesis investigates advanced techniques to control multilayer ceramic composite (MCC) 3D geometry and layer architecture. MCCs have tremendous potential to significantly change a variety of fields due to their ability to withstand extreme environments. However, our limited ability to shape them into complex objects impedes these efforts. To address this issue, two techniques have been introduced: fill coating and bilayer shrinkage driven self-shaping. Central to both techniques is the control of residual stresses experienced by MCCs during sintering. In the case of fill coating and the control of layer architecture, these residual stresses needed to be reduced to prevent the fracture of the novel internal cathode tubular solid oxide fuel cell (IC-tSOFC). This was achieved with the adoption of extended sintering procedures which promoted plastic deformation processes like creep stress relaxation. The novel fill coating technique used to produce IC-tSOFCs was then investigated using scanning electron microscopy (SEM) to ensure that the deposited films were highly uniform and comparable to films deposited using the more mature dip coating technique. The electrochemical performance of the IC-tSOFC was then thoroughly evaluated on a variety of fuel streams including pure hydrogen, dilute hydrogen, simulated exhaust from a boiler, and simulated exhaust from a two-stroke internal combustion engine.

The second focus of this thesis takes advantage of the residual stresses that complicated IC-tSOFC development rather than dissipating them. By using the mismatch in the thermal expansion coefficient between adjacent layers within planar MCCs, curvature may be introduced. Substrates were produced using tape casting and a thin film was then added to this substrate using aerosol spray deposition. By controlling the thickness of the substrate and film, as well as the 2D shape of the substrate and pattern of the applied film, the curvature and shape of the final self-

formed part was controlled. Beyond demonstration of this novel manufacturing technique, investigation into curvature and shape prediction using analytical and finite element method (FEM) modeling enabled the development of a methodology to design parts using self-shaping.

Initial investigations focused on predicting curvature. Though a disagreement between modeling and experiment was observed, an experimental TEC was introduced to replicate experimental results in FEM modeling. This understanding of the 2D curvature was then extended to three dimensions to analyze shape. Predictions regarding bifurcation between cap-like and tube-like deformation modes was applied to the ceramic system using FEM modeling and experiment. These predictions were shown to be consistent with theoretical understanding. Similarly, bending direction for tube-like deformation was shown to be generally consistent with theoretical understanding, but here FEM modeling struggled to reliably predict the final 3D geometry of shapes with high degrees of symmetry, and experimental samples experienced misorientation of bending, indicating that models may need to be expanded to include a greater variety of forces controlling deformation.

Overall, this thesis shows successful development of novel manufacturing techniques to enable wider application of ceramic materials. While the IC-tSOFC introduces new combined heat and power-SOFC systems to be explored, self-shaping ceramics introduces a variety of fundamental questions regarding the underlying mechanism driving bilayer shrinkage within MCCs as well as full understanding of the interaction between 2D substrate shape and film pattern at any scale.

Advanced Manufacturing of Multilayer Ceramic Composites for Application in Solid Oxide Fuel Cells

By

Alexander R. Hartwell

B.S. State University of New York Polytechnic Institute, May 2018

M.S. Syracuse University, December 2020

Dissertation

Submitted in partial fulfillment of the requirements for the degree of Doctor of Philosophy in Mechanical and Aerospace Engineering

Syracuse University

May 2023

Acknowledgements

The experimental work presented in this study was carried out at the Combustion and Energy Research Laboratory (COMER) in the Department of Mechanical and Aerospace Engineering at Syracuse University. Many of the experimental samples were produced by Nathaniel Slabaugh. The finite element model was developed by Dr. Zhao Qin and Saifeldeen K. Elsayed. This material is partially based upon work supported by an agreement with Syracuse University awarded by its Syracuse Center of Excellence in Environmental and Energy Systems with funding under prime award number DE-EE0006031 from the US Department of Energy and matching funding under award number 53367 from the New York State Energy Research and Development Authority and under NYSERDA contract 61736. This research is also based upon work supported by the Syracuse University Center of Excellence in Environmental and Energy Systems Faculty Fellows Program.

Thank you, Dr. Ahn, for sharing in my joy and helping me through my struggles. I am proud to be a part of this academic family, and hope to become a leader like you as I begin my own work as an assistant professor.

To my dissertation committee, Dr. Zhao Qin, Dr. Joseph Paulsen, and Dr. Quinn Qiao, thank you for your patience and flexibility as scheduling was hastily completed.

To my parents, Andrea and Dan, and to my sister Abby, you have made me who I am. You have supported me through every part of this arduous process and always reminded me to take a breath.

To my grandparents, Maxine, Walter, Stanley, and Doris as well as all my extended family, thank you for always believing in me and encouraging me to follow my dreams.

To my fellow COMER lab members, thank you for being a part of the team. Few labs work together and laugh together like we do. I am proud of whatever small role I have played in helping you all achieve great things.

To my friends in academia, it would have been impossible to get here without all of you.

Finally, to my past teachers and advisors, I will never be able to thank you enough for everything you have done. The best thanks I can give is to try to follow in your footsteps.

Imagining something may be the first step in making it happen, but it takes the real time and real efforts of real people to learn things, make things, turn thoughts into deeds, or visions into inventions – Fred Rogers

Contents

1. INTRODUCTION 1

1.1 Background 1

1.2 Objectives 5

1.3 Research Scope 6

1.4 Dissertation Organization 7

2. LITERATURE REVIEW 9

2.1.1 SOFC Architecture 9

2.1.2 Flame-Assisted Fuel Cell 12

2.2 Survey of Ceramics Forming Methods for Solid Oxide Fuel Cells 15

2.2.1 Tape Casting 16

2.2.2 Extrusion 18

2.2.3 Dry Pressing 19

2.2.4 Aerosol Spray Deposition 20

2.2.5 Dip Coating 21

2.2.6 3D Printing of Ceramics 22

2.2.7 Sintering of Ceramic Composites 24

2.3 Self-Shaping Materials 25

2.3.1 Soft Materials 26

2.3.2 Ceramic Materials....30

3. THE INTERNAL CATHODE TUBULAR SOLID OXIDE FUEL CELL....34

3.1 Development of the IC-tSOFC....34

3.1.1 Motivation for Development of the IC-tSOFC....34

3.1.2 SOFC operation within a combustion chamber....37

3.1.3 IC-tSOFC Manufacturing....40

3.1.4 Performance Testing Methods....43

3.1.5 SEM Evaluation Methods....45

3.1.6 Cell Morphology Results and Discussion....46

3.1.7 Cell Performance Testing Results and Discussion....50

3.2 IC-tSOFC Performance on Simulated Exhaust....55

3.2.1 IC-tSOFC Performance on Methane Exhaust....55

3.2.2 IC-tSOFC Performance on Simulated Two-Stroke Internal Combustion Engine Exhaust 63

3.3 Defects Complicating Development of the IC-tSOFC....66

3.3.1 Identification of Defect....66

3.3.2 Identifying the Cause of Fracture....68

4. DEVELOPMENT OF SELF-SHAPING CERAMICS....72

4.1 Observation of Bilayer Shrinkage in Ceramics....72

4.2 Motivation for Forming Self-Shaping Ceramics....74

4.3 Method for Producing Self-Shaping Ceramics....76

4.3.1 Method for Producing and Analyzing Canonical Shapes Experiencing Homogeneous Bilayer Shrinkage....78

4.4 FEM Modeling of Self-Shaping Ceramics....81

4.4.1 2D and 3D Solid FEM Modeling....82

4.4.2 Composite Shell FEM Modeling....84

4.5 Understanding the Behavior of Ceramic Composites Experiencing Bilayer Shrinkage 86

4.5.1 Prediction of Curvature with Stoney Model....87

4.5.2 Prediction of Curvature Using Timoshenko Model....89

4.5.3 Comparison Between Experiment and Prediction for Curvature....91

4.5.4 Predicting Mode of Deformation....94

4.5.5 Predicting Deformation Direction....98

5. CONCLUSIONS AND FUTURE WORK....106

5.1 Conclusions....106

5.2 Future work....109

6. REFERENCES....111

7. CURRICULUM VITAE....133

Abbreviations, Nomenclature, and Variables

Abbreviations and Nomenclature	
BSCF	Barium Strontium Cobalt Ferrite
CEA	Chemical Equilibrium Analysis
Cermet	Ceramic Metal
CHP	Combined Heat and Power
CNC	Computer Numerical Control
COMER	Combustion and Energy Research
DFFC	Direct Flame Fuel Cell
EC-tSOFC	External Cathode Tubular Solid Oxide Fuel Cell
EDS	Energy Dispersive Spectroscopy
EIS	Electrical Impedance Spectroscopy
FEA	Finite Element Analysis
FEM	Finite Element Method
FFC	Flame Assisted Fuel Cell
GDC	Gadolinium Doped Ceria
HVAC	Heating, Ventilation, and Air Conditioning
IC-tSOFC	Internal Cathode Tubular Solid Oxide Fuel Cell
LNC	Lanthanum Nickel Cobaltite
LSCF	Lanthanum Strontium Cobalt Ferrite
LSM	Lanthanum Strontium Manganite
MCC	Multilayer Ceramic Composite

MEMS	Micro-Electro-Mechanical Systems
NiO	Nickel Oxide
OCV	Open Circuit Voltage
ORR	Oxygen Reduction Reaction
PDC	Polymer Derived Ceramic
PZT	Lead Zirconate Titanate
RFQL	Rich-Burn, Flame Assisted Fuel Cell, Quick-Mix, Lean-Burn
SDC	Samarium Doped Ceria
SEM	Scanning Electron Microscopy
SOEC	Solid Oxide Electrolyzer Cell
SOFC	Solid Oxide Fuel Cell
SORC	Solid Oxide Reaction Chamber
Syngas	Synthesis Gas
TEC	Thermal Expansion Coefficient
tSOFC	Tubular Solid Oxide Fuel Cell
XAS	X-Ray Absorption Spectroscopy
XRD	X-Ray Diffractometry
YSZ	Yttria Stabilized Zirconia

List of Tables

Table 1: Material properties of SOFC components 25

Table 2: Gas flow rates for all simulated combustion exhaust and dilute hydrogen baseline tests. Equivalence ratio refers to the combustion reaction producing the set of exhaust mixtures. Adapted from [52]. 56

Table 3: Simulated exhaust, dilute baseline, and pure baseline gas mixtures for testing of IC-tSOFC with two-stroke ICE. Adapted from [160]. 64

List of Figures

Figure 1.1: Schematic of SOFC showing routing of fuel and oxidant (air) streams, path of oxygen ions, oxidation of fuel species, path of electrons, and cell layers. Adapted from [15]. 3

Figure 2.1: Schematic of SOFC showing bilayer cathode to improve electrical conductivity. Routing of ions, gases, and electrons also shown. 11

Figure 2.2: Schematic of no-chamber direct flame fuel cell. Adapted from [15]. 13

Figure 2.3: Schematic of flame-assisted fuel cell. Adapted from [20]. 14

Figure 2.4: Schematic of combustor fuel-rich fuel-lean combustor with FFC stack. Adapted from [22]. 15

Figure 3.1: FFC-Boiler CHP System with fuel cell stack in green placed between the radial burner and heat exchanger. Adapted from [145]. 36

Figure 3.2: Cross-section schematic of traditional EC-tSOFC (left) and novel IC-tSOFC (right). 36

Figure 3.3: NASA CEA plot for combustion of pure methane at equivalence ratios of 0.1 – 5.5. 38

Figure 3.4: Process diagram of fill coating procedure adapted from [64]. 41

Figure 3.5: Computer aided design of IC-tSOFC with cutaway. The inset image of actual IC-tSOFC shows internal current collector, external current collector and the three locations used in SEM analysis of the fill coated films adapted from [64]. 43

Figure 3.6: Schematic showing mounting and gas delivery for testing of IC-tSOFCs adapted from [49] 45

Figure 3.7: SEM images of IC-tSOFC. A-C show cross sections and D shows cathode surface. adapted from [49]. 47
Figure 3.8: Comparison of IC-tSOFC and EC-tSOFC morphologies. Adapted from [49]....48
Figure 3.9: Bar graphs showing longitudinal and radial variation of electrolyte thickness and longitudinal variation of electrolyte and cathode. The inset image shows cross section location. Adapted from [49]....50
Figure 3.10: Power and polarization curves for IC-tSOFC with hydrogen and air flow rates of 100 $mL \cdot min^{-1}$ and 235 $mL \cdot min^{-1}$respectively. Adapted from [49]. 52
Figure 3.11: Power and polarization curves for IC-tSOFC operating at 800 ^oC and 235 $mL \cdot min^{-1}$ air flow rate with varying hydrogen flow rate. Legend indicates hydrogen flow rate in $mL \cdot min^{-1}$. Adapted from [49]....53
Figure 3.12: Power density and polarization curve for EC-tSOFC operating at 800 ^oC supplied with 235 $mL \cdot min^{-1}$ and 100 $mL \cdot min^{-1}$ flow rates of air and hydrogen respectively. Adapted from [49]. 54
Figure 3.13: Power and polarization curves for IC-tSOFC operating on simulated combustion exhaust and dilute hydrogen. Adapted from [51]....59
Figure 3.14: OCV and peak power densities for all simulated combustion exhaust and dilute hydrogen baseline tests with IC-tSOFC. Adapted from [51]....62
Figure 3.15: Power and polarization curves for IC-tSOFC operating on model (simulated) exhaust from two-stroke ICE, dilute baseline, and pure hydrogen baseline tests at 800 ^oC. Adapted from [164]. 65
Figure 3.16: SEM image showing longitudinal fracture of IC-tSOFC going through anode, electrolyte, and cathode layers. Adapted from [168] 67

Figure 3.17: SEM image showing cross-section of IC-tSOFC with contact between cathode and anode labeled. Adapted from [168].....68
Figure 3.18: FEM models of IC-tSOFC (top) and EC-tSOFC (bottom) colored with magnitude of $\boldsymbol{\sigma 11}$.....70
Figure 3.19: Bar plot showing fracture rate of IC-tSOFCs with increasing electrolyte thickness. 71
Figure 4.1: SEM image showing IC-tSOFC with YSZ-GDC buffer layer electrolyte. As a result of mismatched TECs, the electrolyte has deformed in the direction of the GDC.....73
Figure 4.2: Image of wave cell produced using bilayer shrinkage driven self-shaping.....76
Figure 4.3: Flow diagram showing manufacturing of self-shaping ceramics. Substrate is shown in green, film is shown in red, and mask is shown in blue. Provisional patent SU#2023-007 – Bilayer Shrinkage to Assemble Complex Ceramic Shapes. Adapted from [175]. 78
Figure 4.4: Flow diagram showing process for forming homogeneous bilayer shrinkage driven self-shaping ceramics. Curvature $\boldsymbol{\kappa}$ is shown in addition to measure quantities including chord length $\boldsymbol{l}$, arc length $\boldsymbol{s}$ and thickness of the film and substrate respectively $\boldsymbol{t1}, \boldsymbol{t2}$. Adapted from [178]. 80
Figure 4.5: SEM image of bilayer composite used to obtain substrate and film thickness.....81
Figure 4.6 Top: dimensions of two-dimensional finite element analysis bilayer test structure. Bottom: mesh of bilayer showing coarse mesh within substrate and fine mesh in film. 83
Figure 4.7 top: Image showing rectangular mesh for 25 x 10 mm rectangle ABAQUS model. Bottom: Image showing boundary conditions for rectangular samples. 85
Figure 4.8: Image showing boundary conditions for disk ABAQUS models.....86

Figure 4.9: Plot showing curvature obtained in 2D solid FEM models versus parameter $\boldsymbol{\tau}$ obtained from Stoney's prediction for curvature of bimaterial composites. Adapted from [175]. 89

Figure 4.10: Plot showing curvature for Timoshenko analytical model, 2D FEM model, and 3D FEM model for varying film thickness. 91

Figure 4.11: Compilation of all experimental curvatures, analytical models, 2D FEM models, and 3D FEM models. 93

Figure 4.12: Plot showing analytical models with TEC_{exp} determined from experiment and curvature from experimental samples. 94

Figure 4.13 Top: Solid 3D FEM model showing bimaterial composite deforming into cap-like shape. Bottom: Dry pressed SOFC deformed into cap-like shape after sintering. 96

Figure 4.14 Top: 3D composite shell FEM model of 25 x 10 mm rectangle. Bottom: Image of experimentally obtained 25 x 10 mm rectangle sample replicating FEM model. 98

Figure 4.15: Diagrams of analytical predictions for bending direction which show 2D shape with blue dashed line indicating principal axis which will bend. Inset images show experimentally produced samples with bending direction consistent with theoretical predictions. Disks are 5 mm radius and 10 mm radius (left), squares have side lengths of 20 mm and 10 mm (right), and rectangle have dimensions 10 mm x 20 mm (bottom). Substrate thickness is 150 μm and film thickness is 20 μm. Scale bar is 5 mm. Adapted from [178]. 100

Figure 4.16: SOFC MCCs showing unexpected behaviors. 90^{o} misoriented deformation direction (A, C). Varying local deformation (B, C, D). ~45^{o} misoriented deformation direction (E). 101

Figure 4.17: Deformed square composite shell FEM model. Adapted from [178]. 102

Figure 4.18 Top: Rectangle with aspect ratio of 1.064. Bottom: Rectangle with aspect ratio of 1.042. Both are colored by Von Mises stress at point of bifurcation. 103

Figure 4.19: Deformed circular composite shell FEM model. Adapted from [178]. 104

Figure 4.20: Deformed wave composite shell FEM model. Inset image shows comparable experimental sample. Adapted from [178]. 105

Figure 5.1: MCCs formed using bilayer shrinkage driven self-shaping. 108

Figure 5.2: Composite shell FEM model of self-shaping ceramic crane. 110

1. Introduction

Multilayer ceramic composites (MCCs) including solid oxide fuel cells (SOFCs), solid oxide electrolyzer cells (SOECs), solid-state batteries, and solid oxide reaction chambers (SORCs) have tremendous potential to improve our ability to generate and store energy, reduce emissions, and produce clean fuels. Unfortunately, the difficulties associated with the manufacturing of complex ceramic objects limit their application. This has motivated the development of novel film deposition and self-shaping techniques to improve our ability to customize MCC geometry for its intended applications.

The work presented in this dissertation focuses on the development of a technique to coat the inside of a tubular ceramic support with a uniform, microscale film. The stress-state experienced by the MCC during sintering initially resulted in fracture, but after modifying the sintering process, the deposition technique and development of the internal cathode tubular SOFC (IC-tSOFC) was ultimately successful. Though initially an obstacle, the residual stresses observed hinted at the ability to develop an advanced manufacturing method where the mismatched thermal expansion coefficients (TECs) between adjacent layers of the MCC could be used to control the deformation of ceramic sheets, enabling the production of complex 3D geometries. In addition to developing the manufacturing process itself, significant work was necessary to be able to reliably predict the final shape of any given combination of 2D sheet shape and film pattern utilizing finite element method (FEM) modeling, theoretical analysis, and experiment.

1.1 Background

Ceramic materials possess a unique set of thermal, mechanical, and chemical properties which motivate their usage in a wide variety of fields including aerospace [1], power

generation/storage [2], electronics [3], micro-electro-mechanical systems [4], and even medical implants [5]. However, forming complex high-definition ceramic structures is difficult and, in some cases, impossible (as with hinges, encapsulated structures, and chains). Manufacturing is further complicated by the drastic shrinkage, cracking, and warpage that occurs when the ceramic green body is sintered [6–9]. For MCCs the available geometries are further limited to only tubular and planar forms often with restricted layer architectures, e.g., the inability to internally deposit thin films in tubular substrates.

The SOFC is an MCC designed for energy conversion which can use a greater variety of fuels than the more common proton exchange membrane fuel cell (PEMFC) by utilizing high temperature ceramic materials. Hydrogen and carbon monoxide can be used directly as fuels while hydrocarbons such as methane, ethane, and butane can be used indirectly through internal reforming within the anode of the SOFC [10,11] or with external reformers [12–14]. This flexibility is largely due to the key difference between PEMFCs and SOFCs. PEMFCs transport hydrogen ions through the electrolyte whereas SOFCs transport oxygen ions as shown in Figure 1.1. This allows for the direct oxidation of fuel species, giving a high fuel flexibility and impurity tolerance.

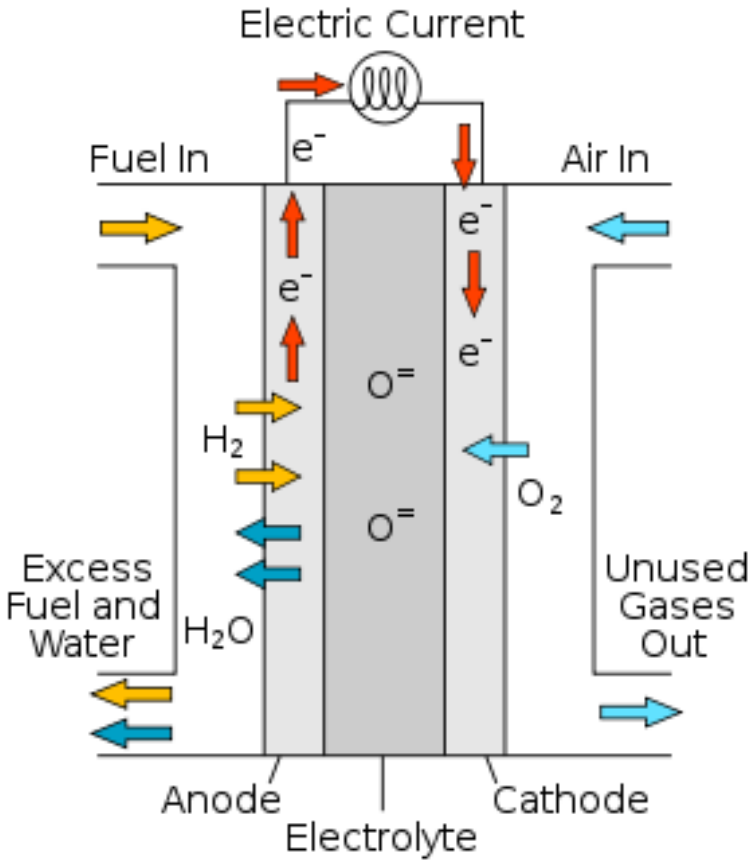

Figure 1.1: *Schematic of SOFC showing routing of fuel and oxidant (air) streams, path of oxygen ions, oxidation of fuel species, path of electrons, and cell layers. Adapted from* [15].

While SOFCs benefit from their flexibility in fuel choice and purity, they are often limited in application by available cell geometries. For example, combustion chambers provide heat and fuel reformation [16–20] which are necessary for SOFC operation, but currently available tSOFC geometries require significant modifications to the existing combustion system for integration [21,22]. Rather than focusing on altering these systems, the goal arises to tailor the tSOFC geometry to enable easy integration into combustion chambers with the development of novel manufacturing techniques. This has prompted the development of fill coating, a process where the interior of a tubular ceramic support is coated with electrolyte and cathode films, achieving the desired IC-tSOFC geometry and architecture.

However, this development was delayed by the high fracture rate experienced by IC-tSOFCs. While the traditional external cathode tSOFC (EC-tSOFC) consisted of the same materials and layer thicknesses as the IC-tSOFC, the change in architecture imposed a nontrivial change in the stress state of the cell. As opposed to the electrolyte layer contracting onto the anode substrate in the case of the EC-tSOFC, the internal electrolyte of the IC-tSOFC exerted a tensile stress on the anode support, increasing the Von Mises stress beyond critical levels resulting in fracture as will be discussed in detail in Chapter 3. While this can be resolved by extending the sintering cooldown procedure to promote plastic deformation mechanisms such as creep stress relaxation [23–25], it offers the potential to serve as a currently unexplored self-shaping mechanism for MCCs.

Self-shaping is a well-explored topic within the world of soft matter physics and has been executed in polymer [26–30] and metallic [31,32] material systems with some recent work beginning to look at ceramic and glass systems [33–36]. The general goal is to form flat sheets into intricately shaped objects without the need for time-intensive 3D printing and with the potential to actuate the final structure [37,38]. For ceramic materials, self-shaping offers a much greater variety of 3D geometries not available with traditional manufacturing methods such as tape casting, dip coating, extrusion, or shell casting and are not restricted by the material limitations associated with 3D printing. Current methods, however, have been restricted by the operative mechanism chosen. For example, by printing filamentous sheets intricate shapes may be formed, but the sheet itself is highly permeable, limiting final application [34,35]. Other methods can produce a dense final part by aligning oblong pore formers on the surface of the ceramic sheet, but this limits the process to anisotropic global deformation [33]. Very recent work offers flexibility in highly controllable local isotropic shrinkage, but because the substrates are formed using 3D

printing, the difficulties associated with 3D printing apply here as well [36]. A method to circumvent many of these limitations is to create a composite where a substrate is coated with a film of different TEC. By controlling the 2D sheet shape and film pattern various combinations of global and local isotropic or anisotropic shrinkage can be used to form fully dense ceramic parts. The work presented here uses experiment, theory, and computational modeling to understand this self-shaping process. As a result, complex MCCs can now be produced enabling SOFC adoption into a wide variety of untouched applications.

1.2 Objectives

The objective of the present research was to develop advanced manufacturing techniques to produce currently inaccessible MCC geometries. This work involves the deposition of ceramic films through the novel fill-coating process and a modified aerosol spray deposition technique to produce novel tubular MCC architectures as well as invoke self-shaping of planar forms. Though each technique was relatively simple to execute, developing procedures to control and utilize the significant residual stresses present within MCCs proved to be the more research-intensive task, necessitating a full understanding of the behavior of ceramic materials during sintering through literature review, experimental analysis of various MCCs, FEM modeling of MCCs, and a comparison against current understanding of the behavior of canonical shapes experiencing self-shaping. To address these needs, the following objectives are given:

- Develop and evaluate a method for internally depositing a uniform microscale film within tubular substrates using scanning electron microscopy (SEM) and electrochemical performance analysis
- Develop method to apply patterned microscale film to planar substrates

- Analyze behavior of experimentally produced self-shaping ceramic composites with homogeneous deposited films with canonical shapes 2D sheet shapes including squares, rectangles, and circles
- Determine bending preference for disks, rectangles, and other canonical shapes
- Develop 3D finite element model of ceramic composite experiencing bilayer shrinkage

1.3 Research Scope

The scope of this work is to develop two novel film deposition techniques combined with modification of sintering procedures to produce currently unavailable geometries of MCCs. A combination of literature review, experimental manufacturing, physical characterization using SEM and mechanical testing, electrochemical performance analysis, and computational modeling are used to achieve this goal.

First, a novel process, fill coating, which is similar to dip coating was used to deposit an electrolyte film inside of a tubular support yielding IC-tSOFCs. This film is examined and compared to films produced using dip coating via SEM and electrochemical performance analysis. The electrochemical performance analysis looks at performance in hydrogen fuel streams to identify the peak power production capabilities as well as simulated combustion exhaust to evaluate efficacy in the intended application of integration into combustion systems. FEM is then used to understand why the IC-tSOFC geometry was uniquely susceptible to fracture during sintering.

Second, the process for depositing a patterned film onto a planar substrate is examined through experimental work and FEM modeling. This again involves the use of SEM to analyze physical characteristics of the film and substrate. The deformation of the entire structure is then

determined for a variety of substrate and film thicknesses and 2D sheet shapes. An FEM model is developed to predict the bilayer self-shaping process. These experiments and models are compared against analytical models developed from previous work by S. Timoshenko [39], G. G. Stoney [40] Pezzula et al. [41], and Alben et al. [42] to determine to what extent current understanding of bilayer shrinkage driven self-shaping may be directly applied to the ceramic system and to identify unique behaviors worthy of further investigation.

1.4 Dissertation Organization

Chapter 1 introduces the history, background, and motivation for developing advanced manufacturing of MCCs. A summary of currently underexplored material systems and deformation mechanisms is offered to motivate the research carried out for this dissertation.

Chapter 2 is a literature review of previous work that supports the investigation into fill coating and the development of the IC-tSOFC by analyzing ceramics manufacturing processes with a focus on behaviors exhibited during sintering. This is then extended to utilize the residual stresses that develop during sintering to self-shape ceramic sheets. Finally, current understanding of the relationships between 2D sheet shape, film pattern, and final 3D geometry is explored.

Chapter 3 presents the development of the IC-tSOFC. Behaviors unique to this geometry of cell are addressed as well as thorough analysis of the mechanical and electrochemical properties of the deposited film. Mechanical analysis is carried out with SEM surveying of experimental samples and electrochemical performance analysis is performed using benchtop testing with various fuel mixtures obtained from analysis of combustion chamber exhaust and chemical equilibrium analysis (CEA). Finally, FEM modeling is used to understand the defect which plagued initial development of the IC-tSOFC.

Chapter 4 describes experimental work associated with the development of the method to form self-shaping MCCs using bilayer shrinkage. Analysis of MCC layer characteristics is performed using SEM and 3D geometry of self-shaped samples is presented and classified. This experimental work is compared against 2D and 3D FEM models of MCCs to predict curvature and shape.

Chapter 5 gives conclusions and future work with a focus on fundamental questions that can be explored with self-shaping ceramics.

2. Literature Review

2.1.1 SOFC Architecture

SOFCs consist of three active layers which transport gases, oxygen ions, and electrons while catalyzing the reactions necessary for SOFC operation. The anode accepts fuel species and catalyzes the breakdown and subsequent oxidation of the fuel ions. Most commonly it is a NiO cermet (ceramic metal) with $(ZrO_2)_{0.92} + (Y_2O_3)_{0.08}$ (yttria-stabilized zirconia, YSZ). The NiO is reduced by the presence of hydrogen into Ni metal before SOFC power generation begins. The Ni metal then catalyzes the breakdown of fuel species into reactive ions while the YSZ transports oxygen ions produced at the cathode to the fuel ions. These species combine and release electrons which travel through the Ni metal to external circuitry, providing electrical power. The formation of bonds between the fuel ions and oxygen ions also releases thermal energy. Interestingly, reactions only occur in the volume where pores containing gaseous fuels, oxygen ion conductors (YSZ), and electron conductors (Ni) converge, known as the triple phase boundary [15]. This region is at the interface between the dense electrolyte and porous anode and extends ~10 μm into the anode as determined experimentally using X-ray absorption spectroscopy (XAS) [43,44]. The microstructure of the anode is especially important as gaseous fuel species and exhaust species must be able to rapidly enter and exit this layer to maintain high power densities. At high current densities, these transport processes limit the power production of the cell contributing to mass concentration losses. Despite these potential issues, it is easy and inexpensive to make highly porous anodes which are also highly electrically conductive, so this layer frequently also provides the mechanical support for the cell with thicknesses ranging from ~500 μm to ~100 μm [45].

The electrolyte plays a much simpler role in the SOFC, maintaining separation between the oxidant and fuel streams, and preventing the passage of electrons while permitting the passage of oxygen ions. To minimize the ohmic resistance caused by the transport of oxygen ions, this layer is designed to be highly dense, but extremely thin often with thicknesses of ~20 μm. This layer must be uniform to prevent the formation of hot spots due to locally high ionic conductance [46,47]. This layer normally consists of only YSZ, but some work has shown increased power production with the use of a buffer layer between the YSZ electrolyte and alternative cathode materials. This buffer layer consists of doped ceria, usually $(CeO_2)_x + (Sm_2O_3)_{1-x}$ (Samaria-doped ceria, SDC) with a $Ba_{0.5}Sr_{0.5}Co_{0.8}Fe_{0.2}O_{3-\delta}$ (BSCF) cathode [48]. BSCF is generally a higher performing cathode than the $LaMnO_3$ (LSM) cathode, but BSCF and YSZ form an insulative barrier consisting of interspecies compounds like $BaZrO_2$ which significantly degrade performance [48,49]. This prevents BSCF from being directly used with YSZ electrolytes. The addition of SDC prevents direct contact between YSZ and BSCF, preventing the formation of this barrier. In addition to material selection, operation at high temperatures can improve SOFC power generation. These high temperatures are necessary to ensure sufficient ionic conductivity of the electrolyte ultimately requiring SOFC systems to obtain cell temperatures in excess of 700 ^oC with peak power generation often occurring at 850 ^oC or 900 ^oC [50–52].

Finally, the cathode catalyzes the formation of oxygen ions with the supply of electrons generated at the anode from the external circuitry. As described above, this layer consists of perovskite type materials such as LSM or BSCF combined with electrolyte material as in the anode to form a triple phase boundary where incoming gaseous oxidant, ion-conducting material, and electron-conducting material intersect. The triple phase boundary in the cathode is smaller than in the anode, typically penetrating only ~5 μm into the cathode [44,53,54]. Cathode materials also

tend to be less electrically conductive than the Ni anode partially due to the highly oxidative environment of the cathode, necessitating the usage of current collecting layers such as a thin film of silver. Alternative materials such as $La_{0.95}Ni_{0.60}Co_{0.40}O_3$ (LNC) can be used to improve electrical conductivity, but as with LSCF, there is potential to form insulative interspecies compounds prompting the use of multilayered cathodes where the LNC does not make direct contact with YSZ. An SOFC schematic with this multilayer cathode is shown in Figure 2.1

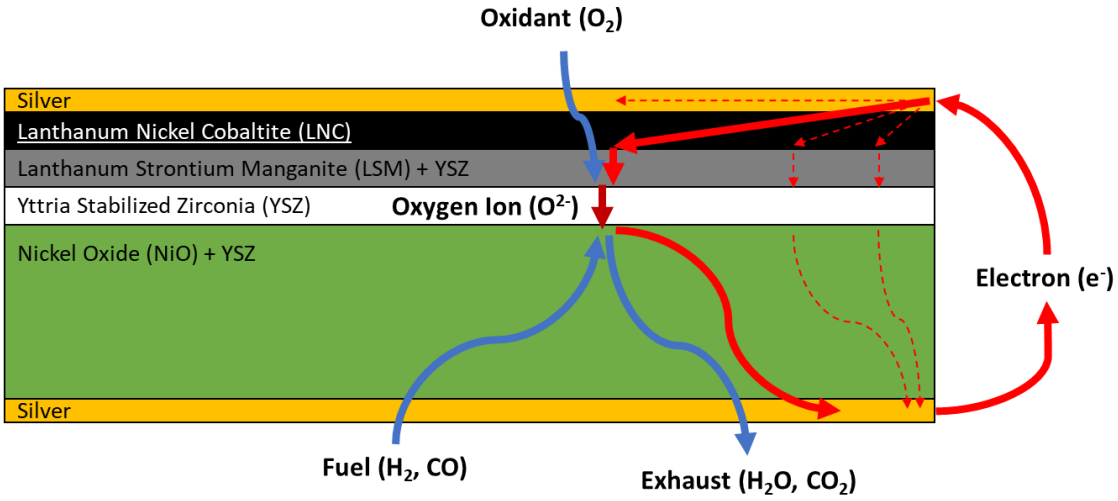

Figure 2.1: *Schematic of SOFC showing bilayer cathode to improve electrical conductivity. Routing of ions, gases, and electrons is also shown.*

Often SOFCs are used in planar stacks where tape casted SOFCs are separated by interconnects which provide electrical connection and gas routing to the cell [15]. This design is very effective for stable, stationary power generation. Due to the high amount of ceramic sealant needed, these stacks can run into leakage issues when operated under high thermal cycling [55]. As such, tSOFCs are often used in mobile and high cycling applications because of their minimal sealant usage [18,56,57]. This cell geometry enables the development of FFCs which utilize the heat and exhaust gases produced by a combustion reaction to generate electrical power.

2.1.2 Flame-Assisted Fuel Cell

Given the above temperature requirement for SOFC operation and the need for the reformation of larger hydrocarbons, a system that already meets both these requirements is ideal for SOFC application. Conveniently, combustion systems produce temperatures that are ideal for SOFC operation. When combustion is completed in fuel-rich conditions high concentrations of hydrogen and carbon monoxide (collectively referred to as synthesis gas or syngas) are produced. Also, these systems need retrofitting to meet the strict emissions goals of modern-day engineering. The resulting combined heat and power (CHP) system can offer many benefits over the heating system itself including increased overall efficiency, removal of harmful gases like carbon monoxide from exhaust, and resilience during extreme weather events [21,22,52,58,59].

There are a variety of different designs for SOFC-CHP systems. The simplest is to place a planar SOFC into a flame as shown in Figure 2.2. This arrangement, referred to as a direct flame fuel cell (DFFC), has achieved high power densities, but often experiences issues with power instability as a result of variations in oxidant supply to the cathode [60–62]. This arrangement has also shown low fuel utilization and electrical efficiency as well as high sensitivity to the location relative to the combustion reaction.

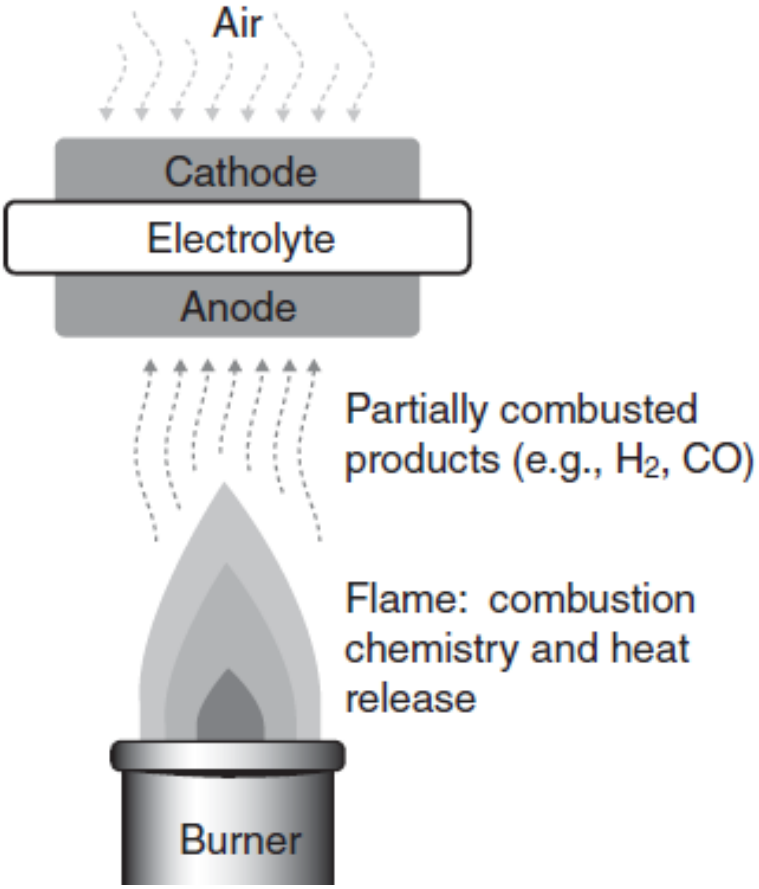

Figure 2.2: *Schematic of no-chamber direct flame fuel cell. Adapted from* [15].

Higher stability in power production as well as higher peak power densities can be achieved by utilizing a flame-assisted fuel cell (FFC) arrangement. Again, a combustion reaction is used to produce heat and syngas, but the SOFC is placed outside of the actual flame as shown in Figure 2.3. High power densities as well as highly stable power production has been achieved with FFCs operating with methane, propane, and butane as fuels [16,20,59]. With less sensitivity to the location relative to the combustion reaction, temperature and fuel/oxidant supply to the cell can be better controlled and more predictable performance can be obtained. FFC systems have also used porous media combustors to promote high efficiency reformation of methane into syngas for SOFC operation [63,64].

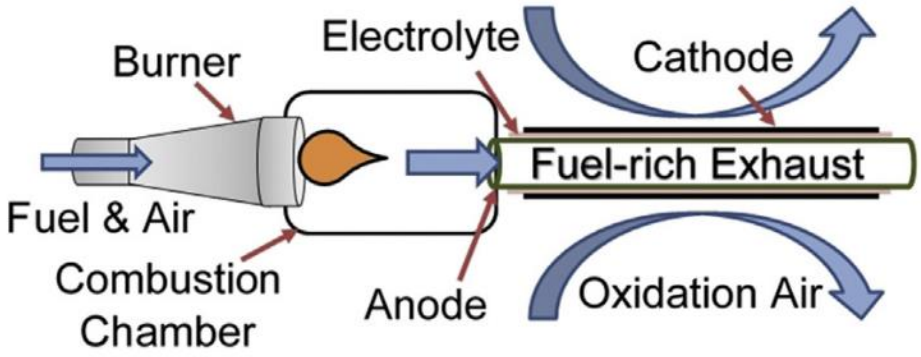

Figure 2.3: *Schematic of flame-assisted fuel cell. Adapted from* [20].

In the FFC arrangement developed by Milcarek et al. [16,20,59], an initial fuel-rich chamber was used to support SOFC operation, and then a fuel-lean chamber downstream of the SOFC stack reacted with any remaining combustible species to ensure high overall system efficiency in a rich-burn quick mix fuel-lean burn (RFQL) chamber [17]. This chamber was ultimately limited by the available fuel cell geometries. In particular, the need to route the fuel containing exhaust through the inside of the cell caused the need to form separate chambers within the combustor. Though this was an effective solution, integration into systems like boilers which use a radial burner surrounded by a concentric heat exchanger cannot adopt this dual-chamber design. Also, retrofitting existing systems was complicated by the need to significantly change existing exhaust routing. As such, recent work has investigated another SOFC-CHP geometry that uses an FFC arrangement without the dual-stage combustion previously necessary as shown in Figure 2.3 [50]. The resulting geometry has the physical support provided by the anode, but the cathode layer is deposited inside the tube. This internal cathode tSOFC (IC-tSOFC) allows oxidant to be routed internally, and the entire cell can be placed directly in a combustion reaction or fed exhaust from a combustion reaction. This eliminates the complex geometry requirements associated with tSOFCs with an external cathode (EC-tSOFCs) and allows for a greater variety of SOFC-CHP system geometries.

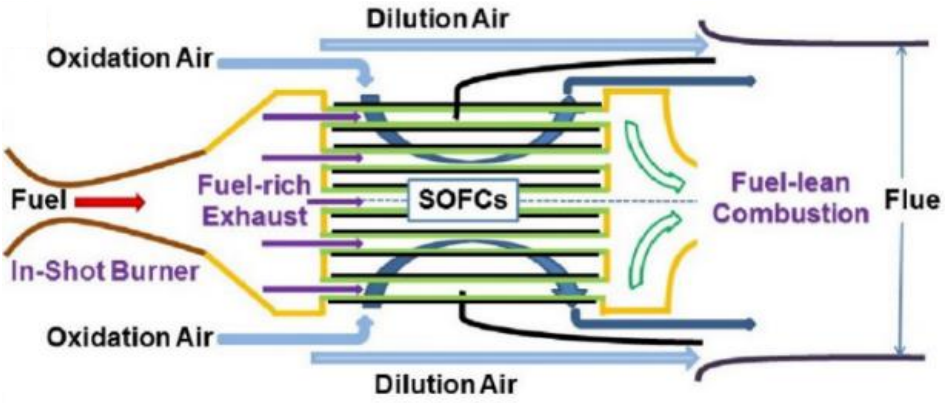

Figure 2.4: *Schematic of combustor fuel-rich fuel-lean combustor with FFC stack. Adapted from* [22].

2.2 Survey of Ceramics Forming Methods for Solid Oxide Fuel Cells

One possible strategy to categorize various ceramic forming methods is whether the material being formed is in a liquid/gel suspension or is a compacted powder/clay. As such, tape casting, dip coating, spray deposition, and slip casting fall under the first category while dry pressing and extrusion fall under the second category. 3D printing will also be discussed as it is a promising modern method for forming ceramics into complex objects, though the limitations associated with 3D printing motivating the development of alternative techniques such as self-shaping will be described in detail.

Mohamed Rahaman in his book *Ceramic Processing* [65] points out the ease with which liquid forming methods can be used to create large ceramic objects easily. Unfortunately, there are many limitations associated with these methods. These methods use a colloidal suspension of ceramic particles, and shape that suspension through the deposition of thin films or coating of molds. This applied film/coating is then dried and sintered to form a solid ceramic object. Drying the deposited film is a major limiting factor in the application of this technique. Uniform drying of the film is necessary to avoid defects such as the formation of mud cracks [66,67]. To promote

uniform drying, the thickness of the film must remain at less than ~1 mm and the temperature, humidity, and composition of the drying atmosphere often must be controlled. Many of the solvents used in liquid processing such as toluene also pose significant health threats requiring drying to be performed in fume hoods or ventilated chambers. Finally, the high concentration of solvent/binder/plasticizer in liquid forming methods causes significant shrinkage from the original casted film to the green body to the final ceramic object making obtaining precise final dimensions of the ceramic part hard to obtain [65,68].

In contrast, solid forming methods are less numerous and have limited application. Dry pressing is primarily used in initial experimental investigations which focus on the ease with which dry pressing may be done with novel materials. Extrusion on the other hand is more commercially viable, capable of producing high volumes of SOFC physical support layers with relative ease. However, geometry is limited to tubular forms with this method and high ratios of wall thickness to cross-sectional area are needed to avoid collapse of the green body during drying.

2.2.1 Tape Casting

Tape casting is well-suited for SOFC production and is therefore one of the most common commercial techniques [69]. Often, the physical support for the cell, whether it be electrolyte or anode supported, is produced via tape casting. In this process a colloidal suspension with relatively low viscosity on the order of tens or single Pa·s is vigorously ball-milled often in stages with the entire mixing process lasting for longer than 76 hours to ensure a homogeneous mixture. A bottomless hopper with two doctor blades placed on top of a polymer sheet is filled with this mixture. The polymer sheet is then pulled underneath the hopper at a constant rate while the doctor blades control the thickness of the casted film, often with the first doctor blade set at twice the

height of the second blade to improve the uniformity of the final film. The wet tape is then pulled into a drying chamber where initial drying causes an ~60% reduction in the thickness of the cast film. Once dry, the tape can be rolled and stored for later use or cut into the desired final shape. This method is often used to form the anode and electrolyte, but alternative methods are frequently used to deposit the cathode such as aerosol spray deposition to ensure this layer is sufficiently thin.

For the sake of this work, two topics are of interest, what processing parameters determine the thickness of tape, and how to avoid common defects. Regarding the first topic, a simple expression has been given in the literature [65] providing the tape cast slurry is well approximated as a Newtonian viscous liquid. The height of the dry, cast tape h_d may be given by:

$$h_d = \frac{\alpha\beta}{2}\frac{\rho_w}{\rho_d}\, h_0 \left(1 + \frac{h_0^2 \Delta p}{6\eta U L}\right) \qquad (2.1)$$

in relation to correction factors α, β, densities of the slurry and dried tape ρ_w, ρ_d length and height of the doctor blade L, h_0, viscosity of the slurry η, pressure difference between the hopper and exit of doctor blade Δp, and the relative speed of the doctor blade to the tape U. This relationship can be simplified so that the height of dry tape h_d is directly proportional only to the height of the doctor blade h_0 if the second term in the brackets is small, as is the case for relatively thin tapes (<200 μm) processed with "normal" parameters (15 – 50 cm·min^{-1} speed, ~30 % organic concentration in slurry, and commercially available tape casting equipment). This relationship demonstrates the ease with which the process can be used to reliably produce tapes of well-controlled thickness. Even for larger tapes, empirically determining the thickness produced for a given set of parameters is simple and repeatable.

The primary limitation that arises with utilizing this process is the above-mentioned drying of the cast film. In addition to the overall shrinkage of the green body, further defects and warping

may occur as a result of nonuniform drying and segregation of particles. Drying that is too rapid may cause cavities within the tape to form. Drying that is too slow can allow large particles which more rapidly come out of suspension to settle at the bottom of the tape introducing anisotropy in particle size perpendicular to the tape. During sintering, this can cause a variation in shrinkage through the thickness of the tape causing warpage. Interestingly, this effect has been used to controllably deform the structure as will be discussed in 2.3.2 based on work from Ding et al. [36]. Similarly, the binder may segregate to the top surface of the tape due to its relatively low density. This enhances particle segregation and therefore increases warpage during sintering.

Despite these issues, if a tape of appropriate thickness (between 10 μm and 1000 μm) is dried at an appropriate rate large planar sheets of ceramic may be formed. These are then ready to be laminated together by hot-pressing or by spraying with subsequent materials. As we will see, this planar substrate is also perfect for executing advanced manufacturing techniques by altering the processes through which materials are added to this basic form.

2.2.2 Extrusion

Extrusion is a much more common technique with wide commercial application and is one of the only commonly found dry forming methods. This method enables the creation of a wide variety of tubular forms including hollow tubes with various external and internal cross-sectional geometries. These forms are particularly useful for SOFCs. The high operating temperatures needed for SOFC operation impose significant thermal stresses which cause mechanically inferior components of the SOFC stack such as the sealant rapidly degrading [55,70]. Tubular forms are almost entirely self-sealing and can continue operation even with minor degradation of the sealant. As a result, tSOFCs have shown impressive robustness to aggressive thermal cycling, withstanding

3,000 rapid thermal cycles, and even showing improved performance after this testing program [57]. This has motivated their usage in a wide variety of DFFC and FFC systems and investigations [16,18,20,22,45,59,64,71–82]. The limiting factor here, however, is that the extruded tube is relatively thick (>300 μm) motivating the anode to be the physical support that is extruded due to the favorable properties described in 2.1.1. The subsequent dip coating processes used to apply the electrolyte and cathode is described in section 2.2.5. then force the anode to be the internal tube surface and the cathode to be the external tube surface. This imposes the need to route fuel species internally, a system constraint that complicates integration into combustion chambers or other fuel containing environments. Work that addressed this geometric limitation will be described in chapter 3.

2.2.3 Dry Pressing

The other common dry forming method, dry pressing, is not used extensively in the commercial production of SOFCs, but it is frequently used at the research and development stage thanks to the absence of additives to the ceramic powder being pressed. Dry pressing is a simple method where ceramic powder is placed into a die and compacted via a hydraulic press. The resulting structure is limited in size due to the exponentially increasing pressure needed to sufficiently compact increasing diameters of dye. Also, the green body is extremely fragile due to the absence of binders, often fracturing during removal from the dye, preventing the production of thin green bodies. These limitations demotivate application within the commercial sense but the inherent lab-scale size and purity of green body enabling insensitivity to the use of novel materials make this technique well-suited to research. Some of the first experiments with DFFCs utilized dry pressed cells [60] similarly much of the initial work investigated SOFC materials as alternative

catalytic converters utilized dry pressed cells to facilitate the use of novel materials for which more advanced manufacturing recipes did not exist [83].

2.2.4 Aerosol Spray Deposition

Whether it be through tape casting, dry pressing, or extrusion, the physical support needs to be coated with two more active films. These additional layers need not provide mechanical strength for the cell, so their thickness may be specifically designed to be optimal for cell performance. As mentioned above, the electrolyte should ideally be 10-20 μm while the cathode can be as thin as 5 μm. One of the best ways to deposit these extremely thin films (and films even thinner than these) while maintaining uniformity is aerosol spray deposition. In this method, a small amount of ceramic powder, typically less than 5 %wt. is added to a solvent with a small addition of dispersant to minimize droplet formation of the deposited film [84]. After ball milling, this slurry is passed through a spray atomizer and coated onto the substrate. In its simplest iteration, this process can be carried out using a commonly available hobby spray gun. Again, this methodology can have issues with nonuniform drying resulting in cracking due to the relatively high thickness of material being deposited. For the cathode, this is unimportant as the cathode primarily serves to catalyze the breakdown of oxygen. However, for the electrolyte this is an unacceptable defect. Furthermore, the deposited film is not highly uniform due to the application procedure being carried out by humans. Again, this is a deformity which cannot occur with the electrolyte.

To circumvent both these issues, much more complex machinery exists to deposit smaller spray particles in a more controlled manner while depositing significantly less material per coating. These methods also use significantly higher air velocities and therefore particle velocities,

allowing for the ceramic particle to impact and then strongly adhere to the substrate surface forming highly dense and uniform films [85]. This is done by using a syringe pump actuated by a stepper motor to control volumetric flow rate of the ceramic slurry, high pressure compressed air as "impact air," and most importantly a nozzle which combines a linear stream of this impact air flowing over the exit of the slurry line with ultrasonic vibration of the slurry line to enhance separation of droplets and breakdown any cohered particles [86]. The resulting film has all the desired properties. The possibility to apply even thinner layers also exists, a particularly useful ability when using multilayered electrolytes with buffer layers with thicknesses of 0.40 μm to 2.3 μm [48].

2.2.5 Dip Coating

There is a major limitation of aerosol spray deposition, and that is time. Spray deposition can require the application of 400+ individual layers to form a 20 μm film. This can take hours and require large volumes of compressed air. For tubular cells this is a greater issue because each cell must be sprayed while mounted onto a rotating fixture. Instead, for tubular cells, dip coating may be used, a process where a ceramic substrate is dipped into a slurry and then pulled out at a constant rate. Again, though simple in general methodology, control of thickness and consideration of defects complicates this process. Several factors are pointed out by Rahaman as contributing to the formation and control of this film including viscous drag on the slurry by the upwardly moving substrate, gravity, surface tension and gradient of surface tension of the slurry, inertia of the slurry as it enters the deposition region far above the surface of the slurry bath, and finally the disjoining/conjoining pressure [65]. Though expressions exist to predict the interaction of these forces to determine a final film thickness, the accuracy of these predictions is low [87] instead

suggesting the desire to empirically determine the thickness of the film deposited for a given set of operation parameters.

2.2.6 3D Printing of Ceramics

Beyond the mature techniques used to form ceramic parts, much attention within the field of ceramics and glass manufacturing in addition to virtually every other material system has been given to 3D printing. Undeniably, this is an extremely potent technique capable of producing highly complex parts which would have been impossible just decades ago. Unfortunately, ceramics are one of the materials least suited to this shaping strategy. The two primary 3D printing strategies, stereolithography and filament extrusion or robocasting encounter various limitations in material selection and part geometry due to the issues associated with drying/removal of binders and sintering mentioned above as well as the mechanism used to print the final parts. Both strategies are primarily carried out with polymer derived ceramics (PDCs). Robocasting methods have been carried out with SiOC [34] by mixing the precursor solution as recommended by the manufacturer and then extruding via a syringe. A simple yet effective method, but one that is limited to the small class of PDCs. Seeing this limitation, Zhang et al. [88] mixed YSZ powder into a photocurable resin and proceeded to robocast this suspension. The resulting parts were further able to be manipulated and folded before sintering like sheet metal to form complex parts. Both studies, however, produced grid-like sheets instead of dense plates limiting application in fields like aerodynamic surfaces or SOFCs.

Dense parts have been formed using the other key 3D printing strategy, stereolithography, with the same PDC [89] and photocurable suspensions [90–93]. These strategies have been highly effective at forming a variety of intricate 3D ceramic parts, but material selection limitations still

exist. The use of photocurable resins imparts optical transparency limitations on the ceramic additive. Alumina, zirconia, and silica have been used, but to this author's knowledge, SOFC materials such as NiO and LSM have not been used, both materials which absorb substantially lighter than any of the above materials. The limitations described above regarding drying/removal of binders and sintering are especially present here due to the high concentrations of solvents and binders. Again, solutions have been found by using a liquid desiccant [90] and vacuum-based binder removal processes but these processes become increasingly complex and time consuming to avoid the underlying issue of the anisotropic composition of the ceramic green body before and during sintering. As a result, forming any large complex object with a high volume to surface area ratio is difficult regardless of the manufacturing method.

Even more recent work has introduced the idea of 3D printing multimaterial ceramic composites [94–96]. This enables the creation of biomimetic structures which combined regions of high hardness and low hardness [94] as is seen in structures like lobster shells [97], obtaining mechanically superior performance to homogenous ceramic parts. Combinations of multiple ceramic materials have also been produced such as multiple zirconias [95] and combinations of $MoSi_2$ with zirconias and aluminas. This enables the separation of electrically conductive and insulative regions to produce heating elements, or again mechanically complex parts. Unfortunately, at this time MCCs with highly dense and uniform ultrathin films have not been produced using these methods preventing application with SOFCs, SOECS, etc. Overall, these are extremely promising techniques with the potential to significantly change how ceramics manufacturing is approached, but there are remaining limitations that can be addressed through alternative strategies.

2.2.7 Sintering of Ceramic Composites

The methods above all describe different methods to form a green body, a collection of ceramic particles held together by binders, interparticle friction, and Van der Waals forces [65]. As a result, green bodies are very fragile and do not possess the robust properties we often associate with ceramics. To transition to extremely hard ceramic parts, the green body must be sintered, or as it is known colloquially, "fired." Sintering is a process where the green body is heated to temperatures above ~50% of that material's melting temperature [68]. At this point, the material on the outer surface which is not as strongly bonded as the material within the particle can begin to migrate. The thin pool of mobile ceramic coating each particle then begins to form bridges between adjacent particles forming a connection that at room temperature gives ceramics very high hardness and strength. The driving force for this movement is the minimization of the overall system energy. This is done by reducing the overall exposed area in addition to reducing curvature. In an idealized system of spherical particles contained within a cubic lattice with 50 % pore volume and 50 % ceramic volume, the sintered shape would approach that of the Schwarz P surface [98]. Reality, however, is far from this idealized scenario with inhomogeneous particle size and distribution. The location of adjacent particles is also not constrained. This introduces the ability for particles to decrease their relative distance. Globally this results in densification/shrinkage where the pore network reduces in volume. This occurs primarily at the peak sintering temperature in a sigmoidal relationship. Depending on the temperature and particle size, and therefore the amount of the particle that can melt, the porosity of the green body can be maintained as is desired for anode supports by using large particles with added pore former, or any minor porosity can be eliminated as desired for the electrolyte by using extremely small particles with no added material to create voids.

With MCCs, after the peak sintering temperature hold, the composite still must return to room temperature from a temperature of 1350 ^{o}C. Now a solid object, the differing thermal expansion coefficients can introduce substantial residual stresses resulting in various forms of fracture or deformation. The material properties of common SOFC MCCs are given in Table 1 below from various sources [99–106] These properties can be used in FEM modeling to predict the stresses and deformation experienced during and after sintering, an ability which will be particularly useful in the following chapters.

Table 1: *Material properties of SOFC components.*

Material	Temperature (K)	Thermal Expansion Coefficeint (x 10^{-6} K^{-1})	Young's Modulus (GPa)
NiO-YSZ	300	3.8	183
	600	5.9	176
	900	8.0	181
	1200	-	181
YSZ	300	7.9	215
	600	9.2	185
	900	10.4	156
	1200	-	157
GDC	300	9.1	195
	600	11.3	187
	900	12.7	154
	1200	-	-

2.3 Self-Shaping Materials

While the manufacturing methods described above are robust and well-understood, they are limited. As discussed, film thicknesses are limited due to drying behaviors, geometries are limited due to extruder dyes or mechanical fragility, and the complex stress state that occurs during

sintering combined with shrinkage and other warpage severely complicates the production of complex ceramic parts. Rather than fight these challenges, a novel strategy is to make use of them. Within the world of soft materials like polymers and metals (at least within the context of thin metal films) this strategy has been explored increasingly within the last few decades with explorations ranging from a fundamental understanding of the deformation mechanism, bilayer shrinkage [39–41,107] to direct application in complex systems [32,108–111]. An overview of the current studies within soft materials is given as well as a brief introduction to current progress in applying this methodology to ceramic systems.

2.3.1 Soft Materials

The underlying mechanism used in many self-shaping techniques is commonly referred to as bilayer shrinkage, a phenomenon in which two materials are stacked on top of each other either with comparable thicknesses as in bimetal thermostats [39] or with a much thinner applied film than substrate as with electroplating [40]. These two material stacks, or "plates," deform as a result of differential swelling or shrinking. Analysis of bimaterial plates experiencing bilayer shrinkage are generally divided between analysis of curvature and analysis of shape. G. G. Stoney in his analysis of electroplating gives an analytically derived expression relating tension within a film σ_1 and the curvature of the composite κ_0 [40]. In addition to material parameters including the film and substrate thicknesses t_1 and t_2 respectively, the substrate Young's modulus E_2, and the Poisson ratio of the substrate ν_2, this relationship may be given as follows:

$$\sigma_1 = \frac{E_2 t_2^2}{6(1-\nu_2)t_1}\kappa_0 \qquad (2.1)$$

For films with thicknesses less than ~10% the substrate thickness this has been shown to be accurate, with improved accuracy of the film and substrate Young's moduli are similar as is the case for NiO-YSZ and YSZ. If the assumption is made that the tension in the film is constant, as is supported by Stoney's experimental observations, a simplified relationship may be given to relate the film and substrate thicknesses to the composite curvature:

$$\frac{1}{\kappa_0} = r \propto \frac{t_2^2}{t_1} \equiv \tau \qquad (2.2)$$

This relationship was used to study initial 2D models of ceramic materials experiencing bilayer shrinkage, but continuing work instead used S. Timoshenko's model [39]. Timoshenko's model is better suited to the shaping mechanism actually driving self-shaping ceramics which is the shrinkage of materials as temperature changes. Again, the curvature κ_0 is given in relation to physical characteristics of the materials being examined, but here no tension within the film is used:

$$\kappa_0 = \frac{6(\alpha_2-\alpha_1)(T-T_0)\left(1+\frac{t_1}{t_2}\right)^2}{(t_1+t_2)\left(3\left(1+\frac{t_1}{t_2}\right)^2+\left(1+\frac{t_1E_1}{t_2E_2}+\frac{1}{\frac{t_1E_1}{t_2E_2}}\right)\right)} \qquad (2.3)$$

α is the TEC, T and T_0 refer to the final and initial temperature of the composite, and other parameters are consistent with the Stoney model. Here, fewer assumptions are made, allowing for varying Young's moduli of the substrate and film to differ. Unfortunately, the material properties used are assumed to be constant in temperature, which for the wide range of temperatures experienced during sintering is not true. Instead, an average was used to apply the Timoshenko model to ceramics.

Beyond these initial application driven investigations, much more recent work has analyzed the behaviors of isotropically shrinking bilayer composites for a variety of fundamental and application oriented purposes [28,107,112]. Disks and regular polygons exhibit well defined and predictable behaviors [41,113] while more complex 2D sheet shapes and anisotropic shrinkage/residual stresses can produce stunning forms such as letters and flowers [114–118]. Predicting the final form of sheets with complex 2D shape as well as complicated film patterns remains a significant open challenge. By prescribing metrics which describe the stress-free sheet configuration as a non-Euclidian surface, a modified definition of strain can be obtained allowing for predictions of the final state [112,114,119,120], but developing these analytical solutions is exceedingly difficult as the sheet complexity increases [121]. Experimentally driven simplified analytical models which predict overall deformation mode by using characteristic areas and lengths can be used to circumvent the difficulties with analytical work as done with simple sheets and films [41,113,115]. However, much work is needed to expand these simplified models into more complex systems. Despite these difficulties, bilayer shrinkage has been used to great effect with soft materials [28,30,38,114,117,122–125] and to a lesser extent semiconductors and metals [32,111].

This underlying mechanism is clearly a topic of much interest and given the complexities associated with this mechanism, the deformation prediction of even simple shapes like symmetric disks offers substantial knowledge currently being explored. Pezzulla et al. for example have investigated a polymer bilayer composite experiencing bilayer shrinkage [41] and identified two key behaviors associated with this phenomenon. The first is a bifurcation between two distinct deformation modes. The second is geometry-controlled deformation orientation.

The first behavior, bifurcation, is a result of the minimization of energy within the sheet either through bending or stretching. Within some regimes, it is energetically favorable to stretch the sheet, particularly when the sheet is "thick" relative to its two-dimensional area; within other regimes, it is favorable to bend the sheet, particularly when the sheet is "thin" relative to its area. The transition between these behaviors can be predicted using simple scaling laws which compare the natural curvature, that is the curvature obtained by a two-dimensional strip experiencing bilayer shrinkage, and the characteristic curvature which is a ratio of the characteristic sheet area to its thickness. Another distinction between these two energy-resolving forms is the conservation of Gaussian curvature [126]:

$$K = \kappa_1 \kappa_2 \tag{2.4}$$

where κ_1 and κ_2 are the curvature along orthogonal directions along the surface of the sheet. The sheet begins with zero Gaussian curvature. When it experiences stretching, the Gaussian curvature will become nonzero, whereas when bending, the Gaussian curvature remains zero. It is important to note that though the Gaussian curvature remains zero while bending, the curvature is not necessarily zero in all-directions, that is $\kappa_1 \neq 0, \kappa_2 = 0$. By necessity, the sheet must remain curvature free in the direction perpendicular to its' bend. This offers rigidity for the sheet in this direction, a phenomenon often utilized to facilitate eating pizza without the tip bending down.

The stretching (U_s) and bending (U_b) energies of a disk may be described as follows:

$$U_s \sim Eh \int_A (R\kappa_0)^2 \, dA \tag{2.5}$$

$$\boldsymbol{U_b \sim Eh^3 \int_A \kappa_0^2 \, dA} \tag{2.6}$$

where *E* is the Young's modulus, *h* is the substrate thickness, *R* is the sheet radius, κ_0 is the natural curvature, and *A* is the sheet area. By comparing these two energies, it can be seen that the

transition from one deformation mode to another is determined by a comparison of the natural curvature κ_0 and the characteristic curvature $\frac{h}{R^2}$. When the natural curvature is greater than the characteristic curvature, bending dominates, while for high characteristic curvatures stretching dominates.

For sheets experiencing bending, where the Gaussian curvature remains zero, the direction of the sheet bend can be determined from the two-dimensional sheet shape. Simply put, the longest length of the sheet will bend. A circular disk will have no preferred bending direction, while an ellipse will bend along its longer axis. A square, interestingly, will bend along the diagonal line reaching from corner to corner, while a rectangle will bend along its longer axis such that the two shorter sides approach each other forming a short, thick tube [41]. There is a question of how complex two-dimensional sheet shapes, for example, annuli and concave shapes like stars and crosses, resolve this energetic battle. Some explorations have investigated this problem, or related ones such as frustrated ribbons with complex reference geometries [127], strained single crystal silicon films which form into spheres [111], and annuli with radially varying shrinkage [112]. There are still many unexplored geometries and influences of shaping mechanisms on geometric resolution.

2.3.2 Ceramic Materials

In the ceramic medium bilayer shrinkage can be best executed by depositing a thin film on a substrate, sintering, and then cooling. As the composite cools, the film expands or shrinks relative to the substrate due to mismatched TECs as shown in Table 1, causing the composite to deform. While it would be expected that the material would have limited impact on the behaviors presented, this has not been the case. Though Pezzulla et al. [41] predict the bending of the longest length of

the sheet, many ceramic sheets have instead shown a desire to bend their shorter edges. Work by Pezzulla et al. [41] as well as Alben et al. [42] shows that for rectangular sheets, the thick tube has lower strain energy than the long tube. The formation of these tubes, however, is heavily impacted by starting conditions. Also, the difference in strain energy between the two shapes is small, often leading to a high prevalence of nonideal final deformation orientations [128,129]. In simulations performed by Alben et al. [42], when sheet deformation began with no initial curvature in any direction, the thick tube was formed exclusively. When a small curvature was imposed on the shorter axis, a thin tube was formed. To transition from this initial bend of the shorter axis to bending the longer axis, the sheet must either transition through a state of non-zero Gaussian curvature or through a state where the sheet is entirely flat, neither of which are feasible transitions [42].

With an understanding of fundamental phenomena related to isotropic bilayer shrinkage comes questions about exceptions to these rules. One idea is that of scale. Sheets, especially larger ones, experience wrinkling and crumpling when area becomes much larger than thickness [130–133]. Although it may be energetically favorable to form one uniform curvature across the sheet, the susceptibility to nonideal starting conditions as exhibited by the rule-breaking tube roll-up has an immense impact on this problem. Previous work concerning this problem has often been limited to relatively “small” sheets where clear deformation patterns were observed. Also, body forces like gravity were not accounted for. As sheets become larger, the force of lifting a large amount of material will become comparable to the high energies associated with deformation. The ceramic medium and the manufacturing methods used here facilitate the exploration of increasingly large and therefore complex sheets where a multitude of behaviors are expected to be seen such as

wrinkling and folding, mechanisms common when sheets resolve geometric mismatches not through global deformation but through local stress relaxation [129,132–139].

Despite the complexities experienced in developing self-shaping mechanisms for ceramic materials, some work has been completed exploring a wide variety of possible techniques. Recently, two methods of ceramic self-shaping where anisotropic shrinkage are imposed on the composite have been investigated; one using magnetically aligned micro-platelets which alter the ceramic microstructure [33], and the other where aligned 3D printed filament sheets control deformation [34]. Though powerful, these techniques represent only a small display of the potential of ceramic self-shaping. Bilayer shrinkage has a greater variety of controllable parameters such as variable film thickness and patterning which can result in complex isotropic and anisotropic shrinkage producing a seemingly limitless catalog of achievable forms. To this author's knowledge, only one attempt has been made at executing isotropic bilayer shrinkage driven self-shaping with ceramic materials. By 3D printing ceramic sheets with varying ceramic concentration, the warping described in the discussion of tape casting may occur. This work by Ding et al. [36] successfully demonstrated the power of isotropic bilayer shrinkage, but the reliance on 3D printing to control the ceramic concentration then introduces all the limitations previously described with 3D printing of ceramics.

This same phenomenon is observed with SOFCs though it has traditionally been seen as a hindrance [9,140]. SOFCs often consist of a thick nickel oxide-yttria stabilized zirconia (NiO-YSZ) anode substrate with a thin YSZ electrolyte film deposited on top. While cooling from sintering, the film shrinks relative to the substrate due to its greater TEC. As a result, the composite warps in the direction of the film, just as in the soft matter system and initial attempts to produce self-shaping ceramics. Instead of a problem, it is proposed this behavior can be utilized as an

advanced manufacturing technique for use with thermally resilient, structural materials circumventing current limitations experienced in ceramics manufacturing.

3. The Internal Cathode Tubular Solid Oxide Fuel Cell

3.1 Development of the IC-tSOFC

The following work is adapted from *The Anode Supported Internal Cathode Tubular Solid Oxide Fuel Cell: Novel Production of a Cell Geometry for Combined Heat and Power Applications* published in the International Journal of Hydrogen Energy 46 (2021) [50].

3.1.1 Motivation for Development of the IC-tSOFC

Producing novel cell architectures is in many ways more straight-forward than controlling entire cell geometries. As such, we will begin by exploring this idea within the context of the development of the novel anode supported internal cathode tSOFC (IC-tSOFC). Development of this cell unlocked many otherwise unavailable applications, while revealing how powerful the interplay between different layers of MCCs can be.

As discussed in section 2.1.2, combustion chambers are uniquely suited for SOFC operation. Unfortunately, tSOFCs are limited by geometry in attaining direct integration into these environments. The necessity to have the cathode layer on the outside of the cell requires fuel to be routed to the inside of the cell, a major hindrance in the case of furnaces and an impossibility in the case of boilers. As can be seen in Figure 3.1, the radial burner is surrounded by the heat exchanger. The SOFC stack must be placed in between these two components, but there is no way to effectively route the exhaust gases through the inside of the cells. The only option is to develop a cell geometry where the fuel-accepting anode surface is on the outside of the tube, and the cathode is the internal surface.

A further constraint is imposed as described in 2.1.1. To obtain the highest possible cell performance, physical support must be provided by the anode. This further limits the cell geometry to an anode supported cell with thin electrolyte and cathode films sequentially applied to the inner surface of the anode tube. No techniques existed to produce this cell geometry, so fill coating was developed. Unfortunately, though this coating technique was effective, it unveiled a vulnerability to fracture during sintering unique to this cell geometry. As will be described in detail, the mismatched TECs between the anode and electrolyte films contributed to critical residual stresses resulting in cracking. This was remedied through the adoption of altered sintering techniques which leveraged plastic deformation processes like creep stress relaxation to dissipate these stresses. This issue, however, was the genesis of the idea to actively use these residual stresses to controllably deform MCCs.

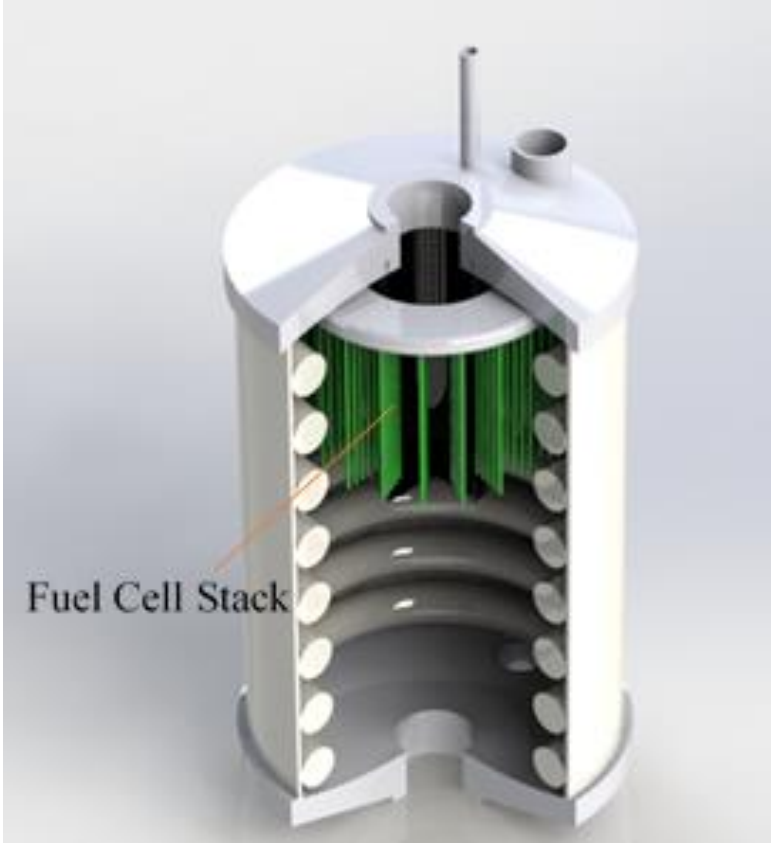

Figure 3.1: *FFC-Boiler CHP System with fuel cell stack in green placed between the radial burner and heat exchanger. Adapted from* [141].

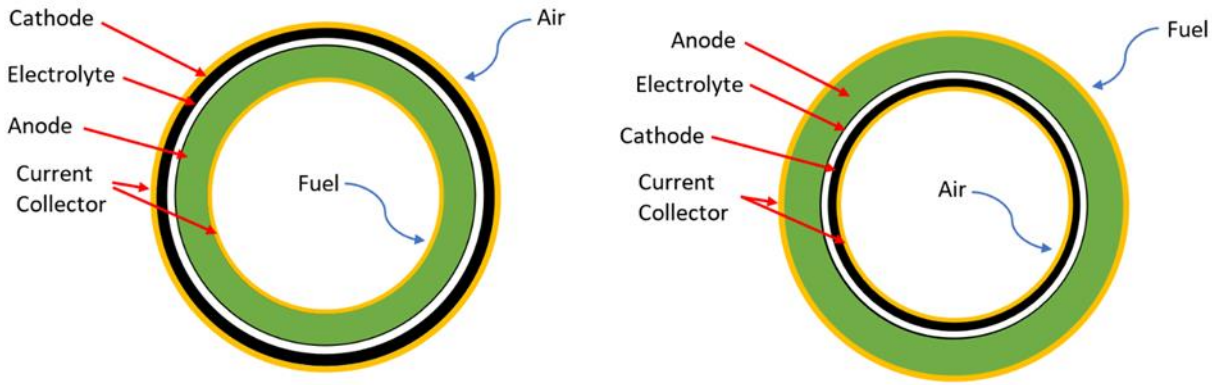

Figure 3.2: *Cross-section schematic of traditional EC-tSOFC (left) and novel IC-tSOFC (right). Adapted from* [50].

3.1.2 SOFC operation within a combustion chamber

Beyond the heat and fuel species that are present in a combustion chamber, the ability to control both aspects is very important for SOFC operation. This can be done by varying the equivalence ratio of the initial combustion reaction. NASA's Chemical Equilibrium Analysis tool can be used to accurately predict the temperature and concentration of various products within a combustion reaction. For an adiabatic reaction, the temperature of the exhaust or the "burned" products T_b can be easily predicted from the incoming reactant temperatures T_u, the number of moles of species i n_i, the heat of formation of species i, Δh_f which can be obtained from literature, and the heat capacity of species i c_{pi}. This yields the equation:

$$T_b = T_u + \frac{\sum_{unburned} n_i \Delta h_{fi,ref} - \sum_{burned} n_i \Delta h_{fi,ref}}{\sum_{burned} n_i c_{pi}} \quad (3.1)$$

The maximum temperature is obtained near stoichiometric conditions, or slightly above at equivalence ratios of 1 – 1.1. At these conditions, no excess reactants are present, minimizing unneeded heating as seen by the minimization of the term $\sum_{unburned} n_i c_{pi}$. This has been confirmed with experiment within the residential boiler intended for IC-tSOFC integration [141]. The flame temperatures achieved in an adiabatic reaction are well in excess of those necessary for SOFC operation, but of course combustion reactions within a combustion chamber are not adiabatic and experimentation has shown that the temperatures present between the burner and heat exchanger are well suited for operation [141,142]. With the rise of higher performance low and intermediate temperature cells, it may also soon become possible to place fuel cells much further downstream of the combustion reaction possibly avoiding alteration of the combustion chamber altogether. These technologies, however, are still at the beginning of development [143–148].

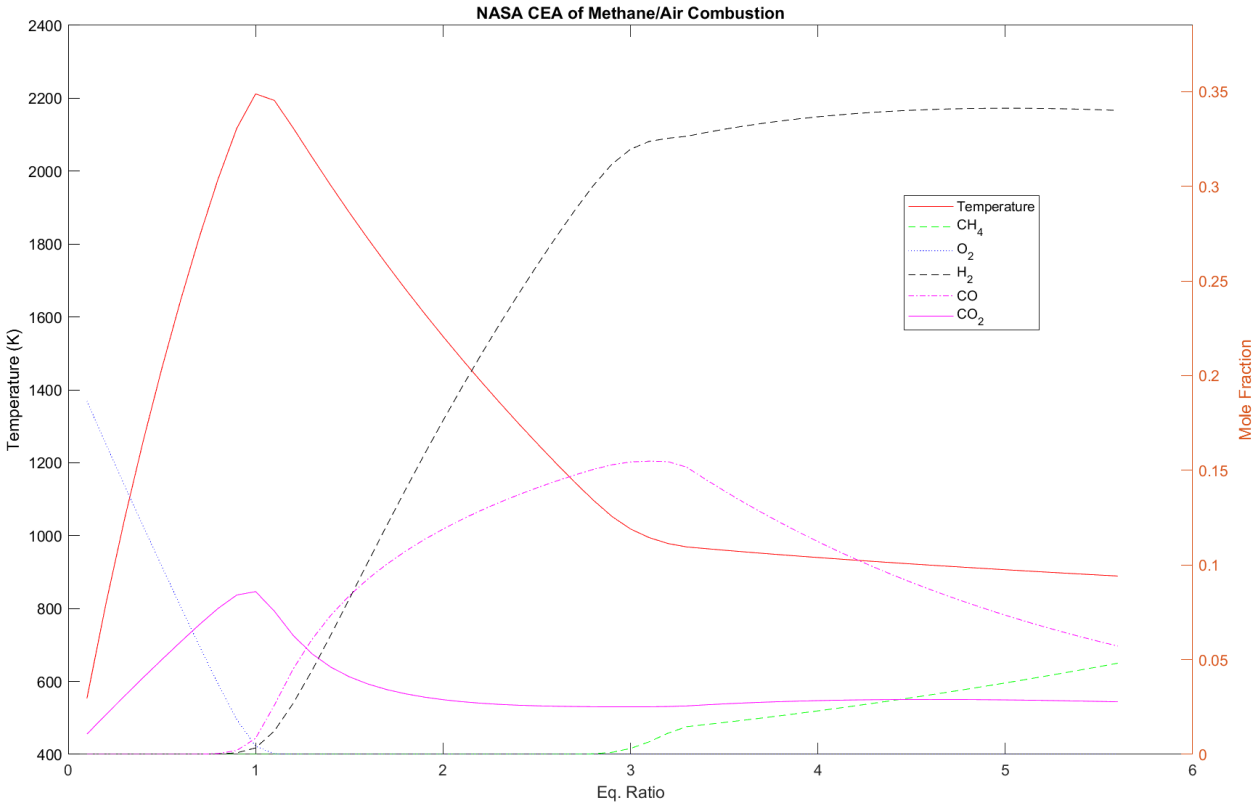

Figure 3.3: *NASA CEA plot for combustion of pure methane at equivalence ratios of 0.1 – 5.5.*

Insight into the ideal reaction conditions for FFC operation can also be observed in Figure 3.3. In increasingly fuel-rich conditions (high equivalence ratio) higher concentrations of syngas become available until an equivalence ratio of approximately 3 where unreacted methane begins to enter the exhaust stream. The flame temperature also rapidly decreases until this limit, indicating that an ideal operation condition is somewhere between equivalence ratios of 1 and 3.

Another limiting factor, however, is the upper flammability limit of methane. Though NASA CEA simulations may give us theoretical results for extraordinarily high equivalence ratios, these are not possible without the addition of porous media combustors or other alterations. There are further factors that affect the upper flammability limit such as reactant temperature, chamber pressure, and chamber geometry, but a general limit of 15 %vol can be given for methane [149].

To determine the corresponding equivalence ratio for this volumetric concentration of methane the following equations can be used:

$$\phi_{ufl} = \frac{v(1+D)UFL}{1-UFL} \quad (3.2)$$

Where UFL refers to the upper flammability limit in %vol, v is the coefficient for oxygen in the stoichiometric combustion reaction, and D is the dilution of oxygen in nitrogen for air. Ultimately, the upper flammability limit in terms of equivalence ratio is $\phi_{ufl} = 1.68$. In experimental work, it has been confirmed that flames became unstable and often extinguish above this limit [141]. As such, a stable equivalence ratio of 1.6 with high syngas concentration was chosen for much of IC-tSOFC testing.

As has been shown in subsequent work investigating the impacts of dilution and unfavorable reaction kinetics associated with syngas [52], SOFC operation is lowered when compared to operation on pure hydrogen. This can be predicted by the Nernst potential:

$$E = E^0 + \frac{\Delta\hat{s}}{nF}(T - T_0) - \frac{RT}{nF}\ln\frac{\prod a_{products}^{v_i}}{\prod a_{reactants}^{v_i}} \quad (3.3)$$

where the variation from the hydrogen-air standard electrode potential, E_0, can be given in relation to the temperature difference from the standard temperature, $T - T_0$, the change in entropy of the reaction, $\Delta\hat{s}$, the moles of electrons participating in the reaction, n, and the Faraday constant, F. The change in cell potential as a result of concentration is given by the third term where R is the gas constant, a is the activity of product and reactant species, and v_i is the number of moles of each species i.

3.1.3 IC-tSOFC Manufacturing

The materials used with IC-tSOFCs were the standard NiO-YSZ cermet anode, dense YSZ electrolyte, and LSM-YSZ cathode. Manufacturing began with an extruded anode support as described in 2.2.2. After extrusion, drying, and presintering, the internal and external diamters of the tubes were 2.4 mm and 3.2 mm respectively. Control cells were produced using the standard dip coating process described in 2.2.5 resulting in external electrolyte and cathode layers. The IC-tSOFCs, however necessitated the development of fill coating. This process is shown in Figure 3.4. In contrast to dip coating where the cell is immersed into a ceramic slurry, in fill coating the slurry is injected into the tube. This is done while the tube is held approxmately horizontally and then rolled to obtain a uniform coverage of the internal surface of the cell. The tubes were then placed vertically onto a paper towel to absorb excess slurry. To dry this film, the cells were placed into a 100 ^{o}C oven for 15 minutes. They were then taken out and the process was repeated. In total, four layers were applied to the inner tube surface. To further promote uniformity of the final film, the slurry was injected from alternating ends of the tube. The film thickness and uniformity was a function of a variety of complicated parameters as described in relation to dip coating. As described in relation to many ceramics manufacturing proceses, in place of difficult to use and ultimately inaccurate analytical predictions of deposition processes, empirical rules were used to understand this novel process. Furthermore, to ensure this process produces a comparably uniform film, comprehensive characterization was carried out using SEM as will be described in the following sections. Ultimately it was determined that each deposition results in an ~5 μm thick layer of electorlyte, so four depositions will produce a 20 μm thick electrolyte as confirmed in Figure 3.9.

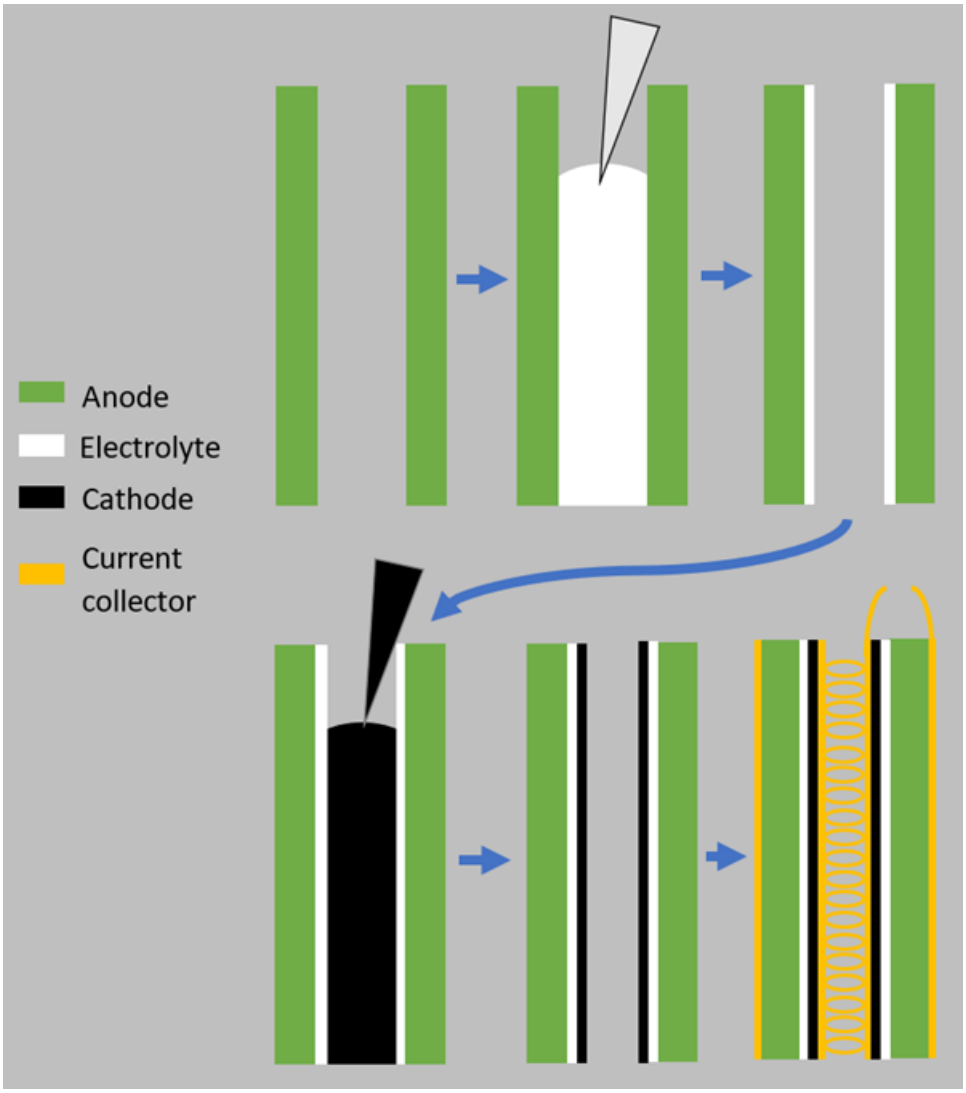

Figure 3.4: *Process diagram of fill coating procedure. Adapted from* [50].

After fill coating of the electrolyte, the cells needed to be sintered. As was discovered during the development of the IC-tSOFC which will be described in detail in the section 3.3, the standard sintering procedure used for tSOFCs resulted in consistent fracture of the IC-tSOFC as a result of critical residual stresses within the cell. This issue was remedied by introducing a substantially altered sintering procedure where cells were heated to a peak temperature of 1350 ^{o}C at a rate of 2 ^{o}C·min^{-1} then cooled at a relatively slow rate below 0.5 ^{o}C·min^{-1}. Holds were also added at 800 ^{o}C and 600 ^{o}C for fourteen and twelve ours respectively. Combined, this cooldown

procedure promoted plastic deformation processes which relieved critical stresses within the IC-tSOFC. In particular, creep stress relaxation was expected to be a major source of stress relaxation within the cell. Previously it has been studied to relieve curvature in planar cells (a fact which will be utilized heavily in following sections) [9,140,150] as well as to improve sealant durability [25,151]. During the process of creep stress relaxation, sufficient thermal energy is present to allow for the shifting of atomic lattices as well as larger grain structures when loads are applied to crystalline structured. Dislocations and vacancies are allowed to diffuse throughout the lattice resulting in plastic deformation of the individual ceramic grains while larger grain boundaries are also able to diffuse, slightly altering the ceramic microstructure. As a result, small amounts of strain occur reducing the residual stresses within the MCC [23,152,153]. Interestingly, EC-tSOFCs do not experience this issue as will be investigated using FEM in section 3.3.2, so this modified sintering procedure was not used.

The cathode was then added on top of the sintered electrolyte film, again using the fill coating procedure, but this time with only one coating to ensure a sufficiently thin cathode as dscribed in 2.1.1. The standard two hour 1100 ^{o}C sinter was used for the cathode, however, for IC-tSOFCs heating and cooling rates were maintained at 1 ^{o}C·min^{-1} again to avoid the development of critical residual stresses. Six-hour holds were also added at 600 ^{o}C and 800 ^{o}C. For EC-tSOFCs, standard sintering procedures were used.

The fully sintered cells still needed to be mounted to quartz tubes for testing and electrical connections needed to be made to both the anode and cathode surfaces. Full details are given in [50], but the key novel step that will be discussed here was the need for an internal current collector for the IC-tSOFC cells. LSM-YSZ has a relatively low electrical conductivity of between 40 to 460 S·cm^{-1} at 1000 ^{o}C [154], so connection to external circuity must be made to the entire

cathode surface. This is done with a thin coating of silver paste and wrapping of steel and silver wire. For IC-tSOFCs, the typical wire wrapping procedure is not possible, so instead the steel and silver wire was wound around a 2.2 mm diameter dowel to form spirals. These spirals were then coated with silver paste and pulled through the center of the IC-tSOFC simultaneously coating the interior cathode surface with silver while attaching the external circuitry wires. This is all shown in Figure 3.5.

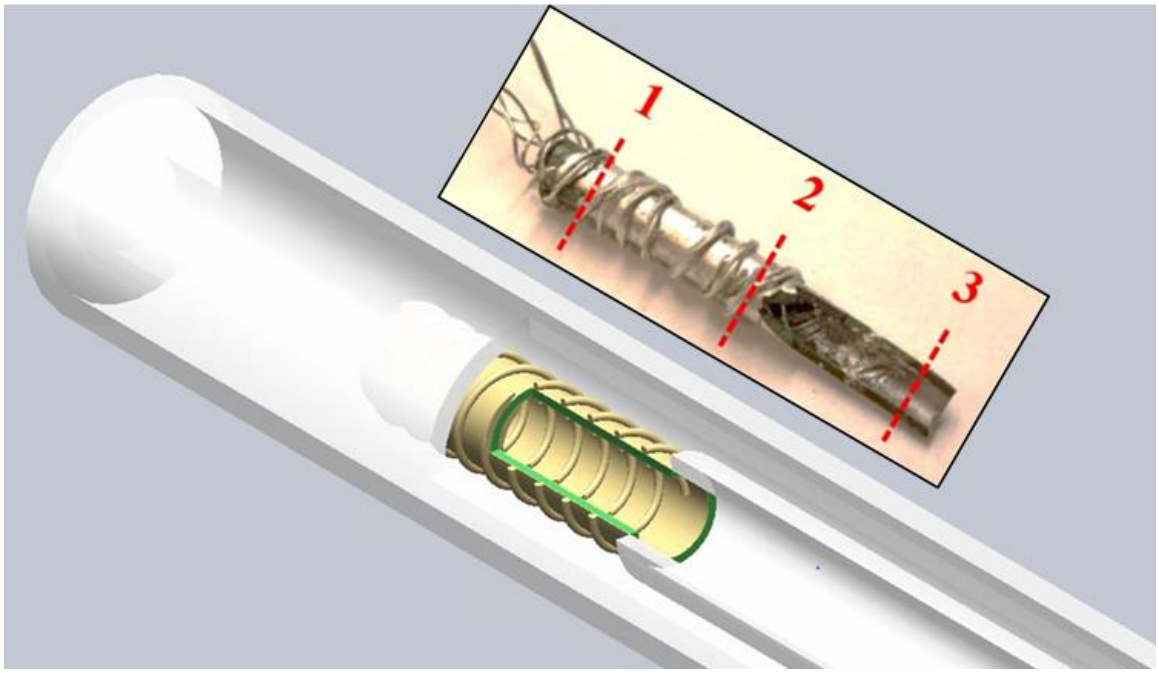

Figure 3.5: *Computer aided design of IC-tSOFC with cutaway. The inset image of actual IC-tSOFC shows internal current collector, external current collector and the three locations used in SEM analysis of the fill coated films. Adapted from* [50].

3.1.4 Performance Testing Methods

To evaluate and compare the performance of the two geometries of cell, hydrogen was used as a fuel and air was used as an oxidant. The volumetric flow rate of both gases could be carefully controlled using flowmeters and a LabView program. The mounting and gas delivery to the cell is shown in Figure 3.6. Quartz tubes were used for mounting the cells as well as for

containment of fuel and oxidant gases. For the IC-tSOFC, both ends of the cell were mounted to quartz tubes to provide internally routed oxidant and to prevent unwanted recombination reactions occurring at the exhaust end of the cell. This setup was then contained within a larger quartz tube where fuel was provided. This setup replicated the environment intended for IC-tSOFC integration where fuel is abundant outside the cell and the mounting for the cell also is the oxidant supply as shown in Figure 3.6. This entire setup was then placed within a tube furnace where environmental temperature was varied from 650-800 ^{o}C. Before testing began with any cell, reduction of the NiO-YSZ was necessary. This was done by supply the anode with hydrogen gas at a flow rate of 100 mL·min^{-1} for two hours in a furnace heated to 650 ^{o}C, turning the NiO into nickel metal.

After reducing, testing began. Hydrogen flow rates were varied from 50-150 mL·min^{-1} while the air was maintained at a rate of 235 mL·min^{-1}. Stoichiometric mixtures corresponded to 100 mL·min^{-1} hydrogen and 235 mL·min^{-1} air. Power and polarization curves were obtained with a Keithley 2420 sourcemeter using the 4-point probe method. Active areas of the cell were defined by the unobstructed cathode area of the cell. The active areas were 1.26 cm^2 and 1.28 cm^2 for the IC-tSOFC and EC-tSOFC respectively, corresponding to tube lengths of 1.67 cm and 1.27 cm.

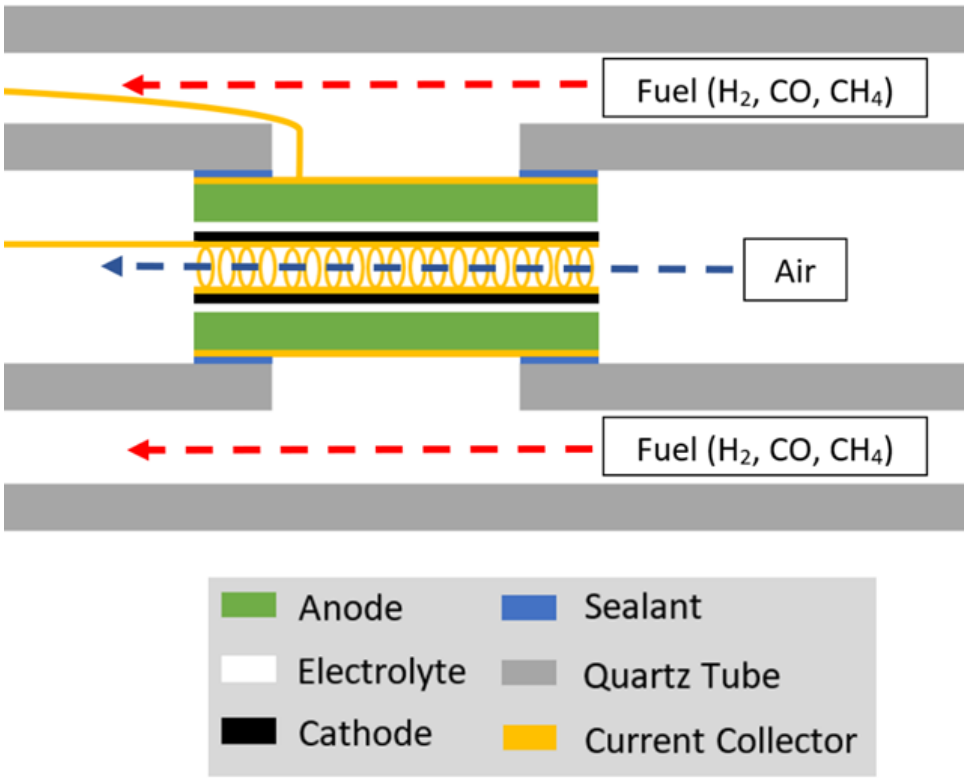

Figure 3.6: *Schematic showing mounting and gas delivery for testing of IC-tSOFCs. Adapted from* [50].

3.1.5 SEM Evaluation Methods

A JEOL JSM-5600 SEM was used to obtain images of the EC-tSOFC and IC-tSOFC microstructures and layer uniformities. As indicated in Figure 3.5, three cross-sections of each type of cell were obtained by scoring then fracturing the cell. Each cross section was then imaged at the top, bottom, and each side. At each of the twelve sites where images were taken, five measurements of each layer thickness were taken. Image processing software was then used to measure the thickness of the electrolyte and cathode films. Average thicknesses and corresponding standard deviations were calculated for the whole cell, each cross-section, and each site at the cross-section to obtain overall thickness as well as longitudinal and radial thickness variations. To obtain high topological contrast, the SEM was used in secondary electron imaging mode.

3.1.6 Cell Morphology Results and Discussion

Figure 3.7 shows SEM images of the IC-tSOFC. Desired characteristics described in section 2.1.1 such as a porous anode, dense electrolyte, porous cathode, and thin metallic current collector on the cathode surface can be observed. Figure 3.7 A, B, and C all show distributed 5 μm spherical pores which are created by the addition of methylcellulose to the anode clay. In addition to these large pores, ~500 nm black spots may be observed throughout the anode. These are caused by reduction of NiO to Ni [155]. Figure 3.7 D also shows the high porosity of the cathode obtained by sintering at 1100 ^{o}C [156]. In cells where the cathode is cosintered with the anode and electrolyte, the resulting microstructure is significantly denser. Figure 3.7 C shows a large pore most likely caused by inclusion of air within the extruded clay [157]. The anode support tubes used for the IC-tSOFCs and EC-tSOFCs were the same, so these defects were not expected to contribute to differences between cell performance.

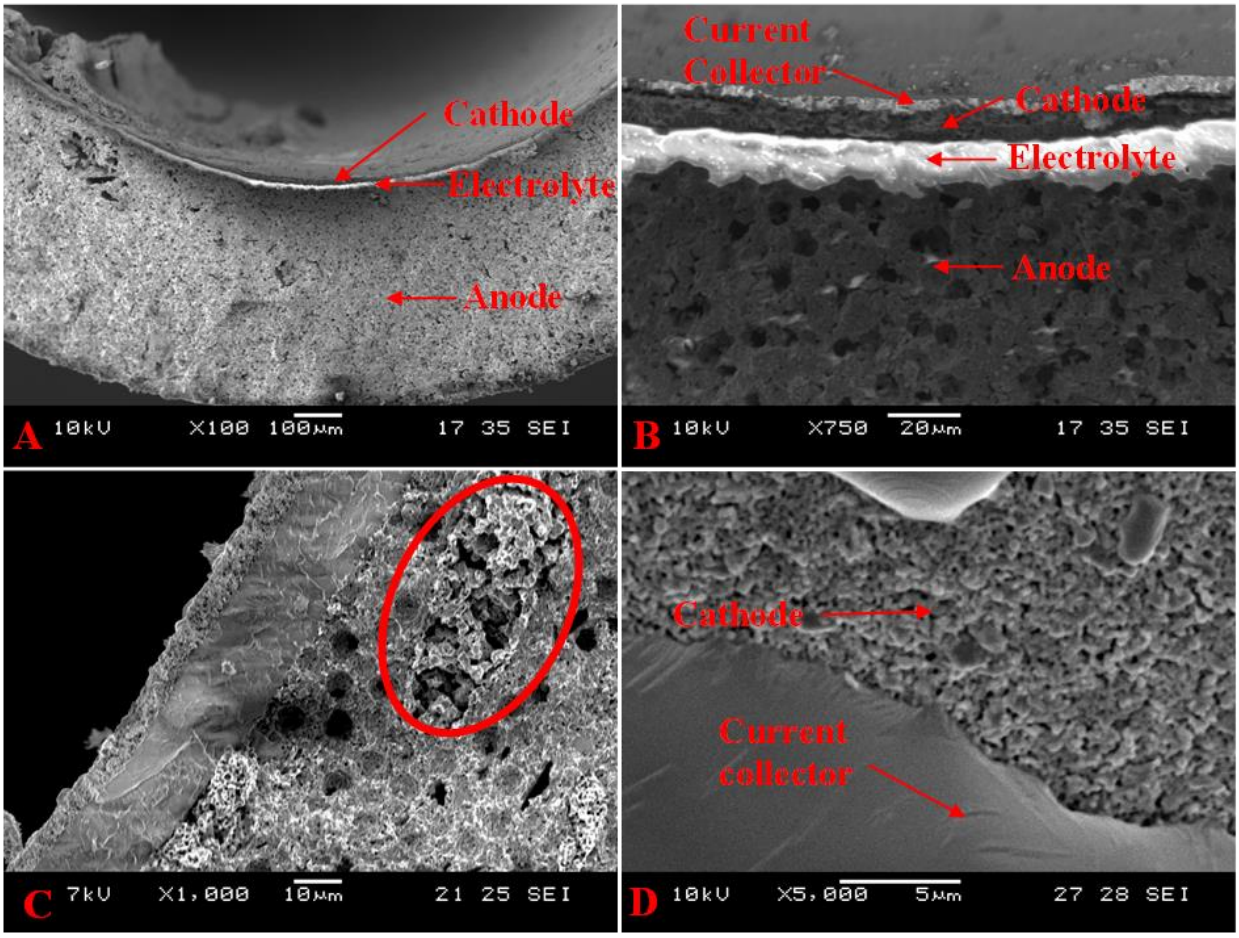

Figure 3.7: *SEM images of IC-tSOFC. A-C show cross sections and D shows cathode surface. Adapted from* [50].

A comparison between the IC-tSOFC and EC-tSOFC morphologies is shown in Figure 3.8. As densification of ceramics is a function of time and temperature as discussed in section 2.2.7, differences in microstructure are expected to be the result of the increased sintering time for the IC-tSOFC due to the extended electrolyte cooldown procedure and low cathode sintering heating and cooling rates. Figure 3.7 A and C generally show lower densification and smaller grain size; however, differences are minor, and larger scale pores generated through pore formers appear unchanged.

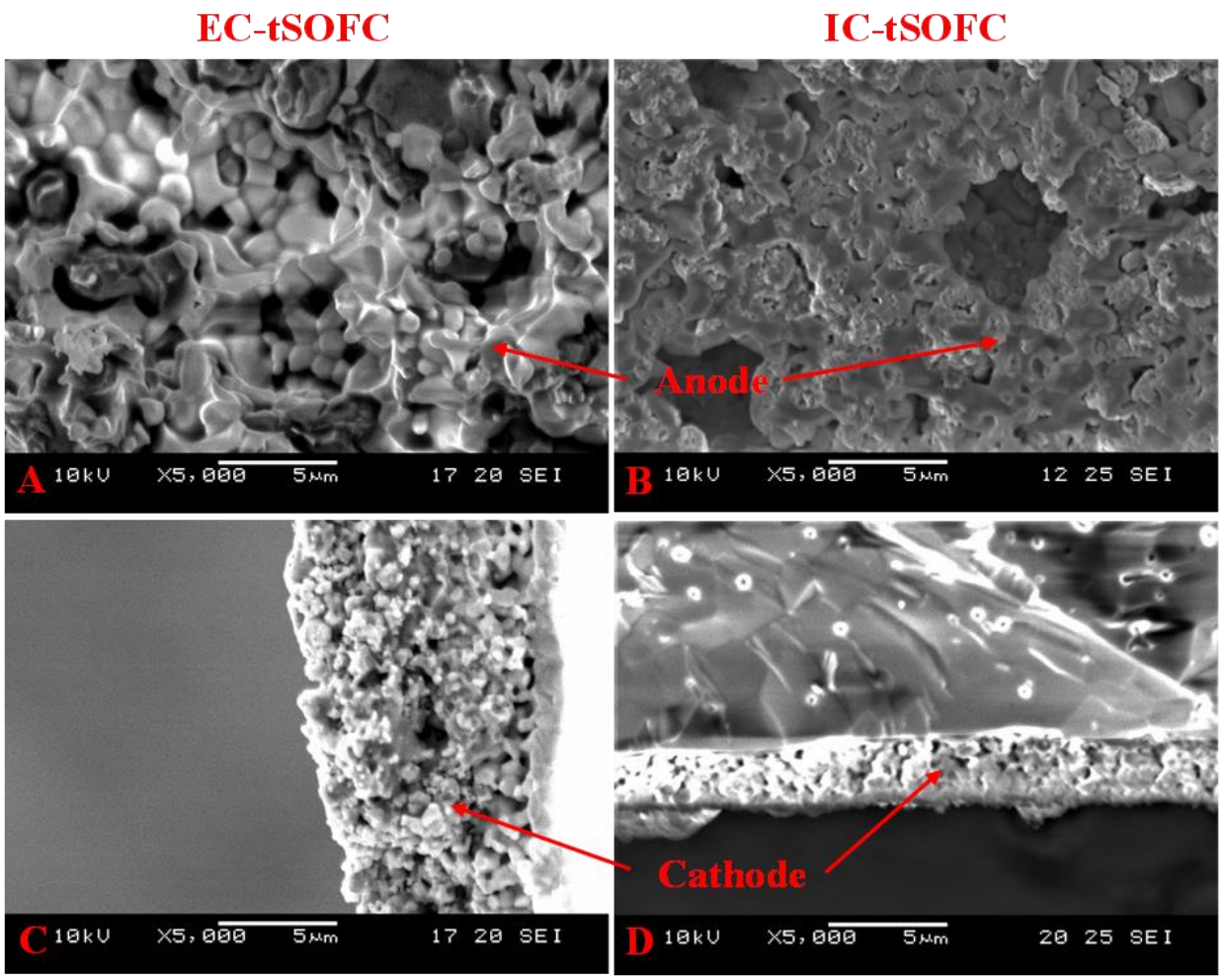

Figure 3.8: *Comparison of IC-tSOFC and EC-tSOFC morphologies. Adapted from* [50].

Figure 3.9 shows the results for measurements of the cathode and electrolyte films for dip coating and fill coating. Average electrolyte thicknesses for the EC-tSOFC and IC-tSOFC were 21.6 µm and 18.3 µm respectively with standard deviations of 3.32 µm and 2.53 µm respectively. For the cathode, average thicknesses of 3.33 µm and 2.49 µm were found with standard deviations of 4.13 µm and 1.06 µm for the EC-tSOFC and IC-tSOFC respectively. To enable facile comparison between cell geometries, it was desired to obtain the same layer thicknesses for EC-tSOFCs and IC-tSOFCs. Though they are not the same, the two values are still within approximately one standard deviation of each other. For the cathode and electrolyte, the standard

deviation of the thickness is greater for the EC-tSOFC than the IC-tSOFC. This indicates the novel fill-coating procedure produces a comparable and potentially superior deposited film. A major contributor to the high deviation observed with the EC-tSOFC cathode was delamination. Some areas of the cell had no observable cathode. This delamination was most likely caused by the mismatch in TECs between cell components as has been observed frequently in SOFCs [2,158]. The addition of the creep stress relaxation step as well as improved coverage of the electrolyte surface due to the agitation during deposition in the case of the fill-coating procedure could have aided in preventing delamination for the IC-tSOFC cell.

Variations in thickness in the longitudinal and radial directions can be observed for both deposition techniques. Electrolyte longitudinal variation remains within one standard deviation of the overall cell thickness. The same can be said for the cathode layers, though the EC-tSOFC has a higher standard deviation overall. Radial thickness variation is also within the overall cell thickness standard deviation, but for the IC-tSOFC there is a noticeable trend. Thin sections are seen opposite thick sections with intermediate section in between indicating a gradual increase in thickness towards one side of the tube. This can be explained by the fill coating procedure where the slurry is initially injected horizontally into the cell.

Overall, the novel fill coating procedure was shown to produce desirable microstructures for all cell layers coated using this process as well as films which were as uniform as the much more mature dip coating process. The absence of fracture lines throughout all SEM imaging showed a resolution to the initial issues with critical stresses with the use of altered sintering procedure.

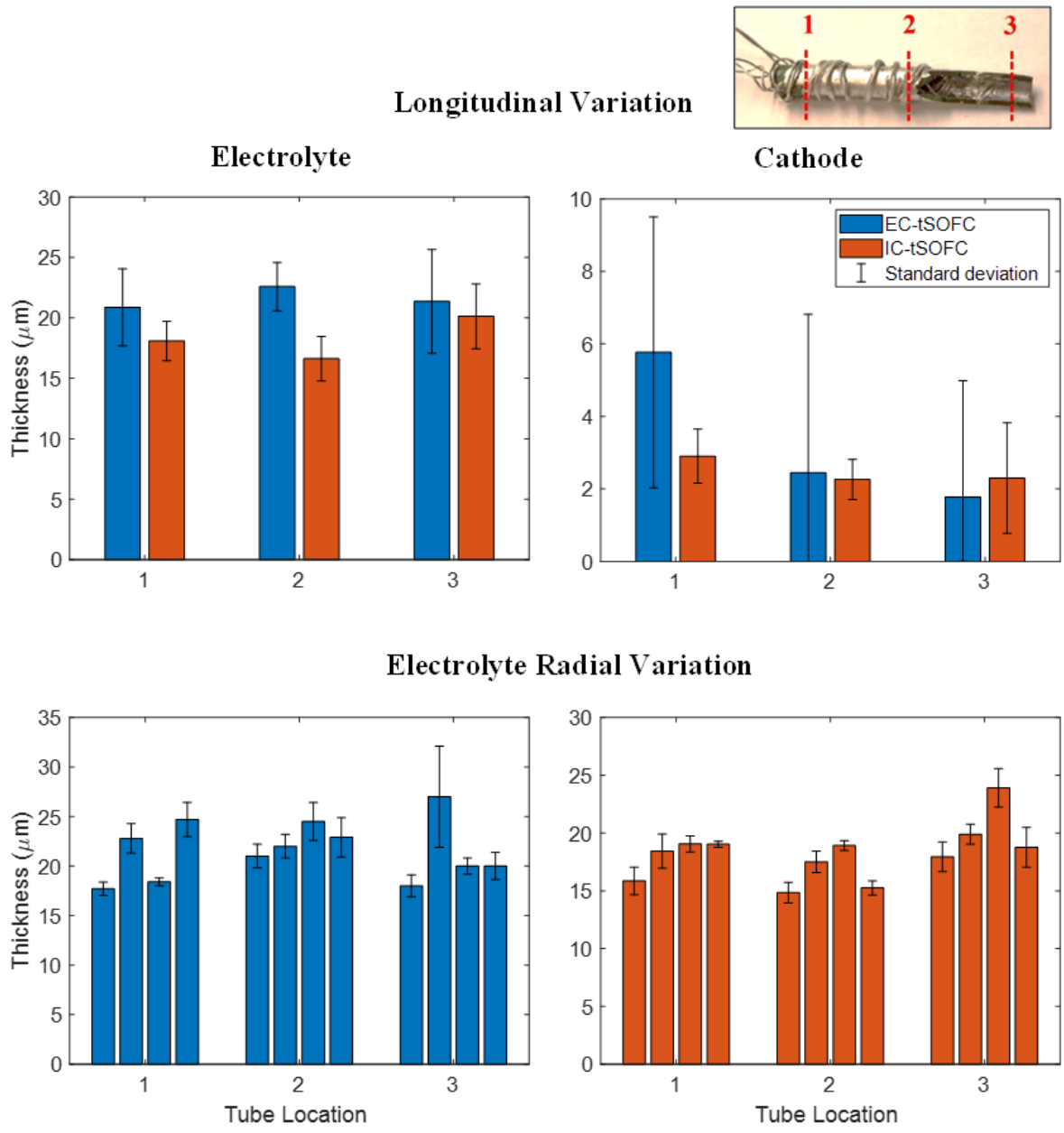

Figure 3.9: *Bar graphs showing longitudinal and radial variation of electrolyte thickness and longitudinal variation of electrolyte and cathode. The inset image shows cross section location. Adapted from* [50].

3.1.7 Cell Performance Testing Results and Discussion

Beyond physical analysis of the novel IC-tSOFC, it was necessary to evaluate its electrochemical performance and ensure it was well suited for operation within the intended combustion chamber applications. Figure 3.10 shows IC-tSOFC performance variation for

temperature from 650-800 ^{o}C. A peak OCV of 0.98 V was shown at a temperature of 650 ^{o}C and decreased to 0.95V at 800 ^{o}C as predicted by the Nernst potential equation 3.3. For the H_2-O_2 reaction $\Delta \hat{s}_{rxn}$ = -54.755 J·(mol·K)$^{-1}$ at 650 ^{o}C [15]. With a standard electrode potential, E_0 of 1.229 V [15], the number of transferred electrons, n of 2, the Faraday constant, F, and 21 % concentration of oxygen in air, an OCV of 1.02 V can be expected. The measured OCV at 650 ^{o}C is only 0.04 V lower than this predicted value, indicating minimal losses to the cell. Minor things like the resistance of the electrical connections between the cell and Keithley sourcemeter can explain this small difference. Agreement between the expected and measure OCV indicate, as observed in SEM analysis, that the electrolyte layer is well-formed and provides sufficient electrical insulation between the anode and cathode without providing substantial ohmic losses. Furthermore, easy access to the triple phase boundary thanks to high porosity of the anode and cathode minimized any activation and mass concentration losses.

The power curves show a maximum peak power density of 369 mW·cm^{-2} at 800 ^{o}C and a minimum peak power density of 86.5 mW·cm^{-2} at 650 ^{o}C. Unlike the cell voltage, as the temperature of the cell increases, the ionic conductivity of the electrolyte increases, reducing ohmic losses within the cell and increasing overall power production. Reactions at the cathode and anode are also increased as more thermal energy is present to activate elementary reactions. The fuel utilization efficiency ε_F associated with the maximum current i can be used to evaluate cell performance and is calculated using the following equation:

$$\varepsilon_F = \frac{i}{nF\nu_{mole}} \qquad (3.4)$$

where n and F are the same as in the Nernst potential equation 3.3, and ν_{mole} refers to the molar flow rate of fuel. With the calculated active area of 1.26 cm^2 for the IC-tSOFC, the maximum

current density of 1.355 A·cm^{-2} at 0.200 V, and the molar volume of a gas at standard conditions of 2.24 m^{3}·mol^{-1}, a maximum fuel utilization of 11.9 % can be given for the IC-tSOFC operating with a 100 mL·min^{-1} hydrogen flow rate. Similarly, a fuel utilization corresponding to the peak power density where current density is 0.871 A·cm^{-2} is 7.64 %. At high fuel utilizations (>40 %), anisotropy in reactant concentration combined with a multitude of other effects can complicate cell performance obscuring the impacts of cell geometry [79,159]. Therefore, it was desired to perform cell comparisons at low fuel utilizations.

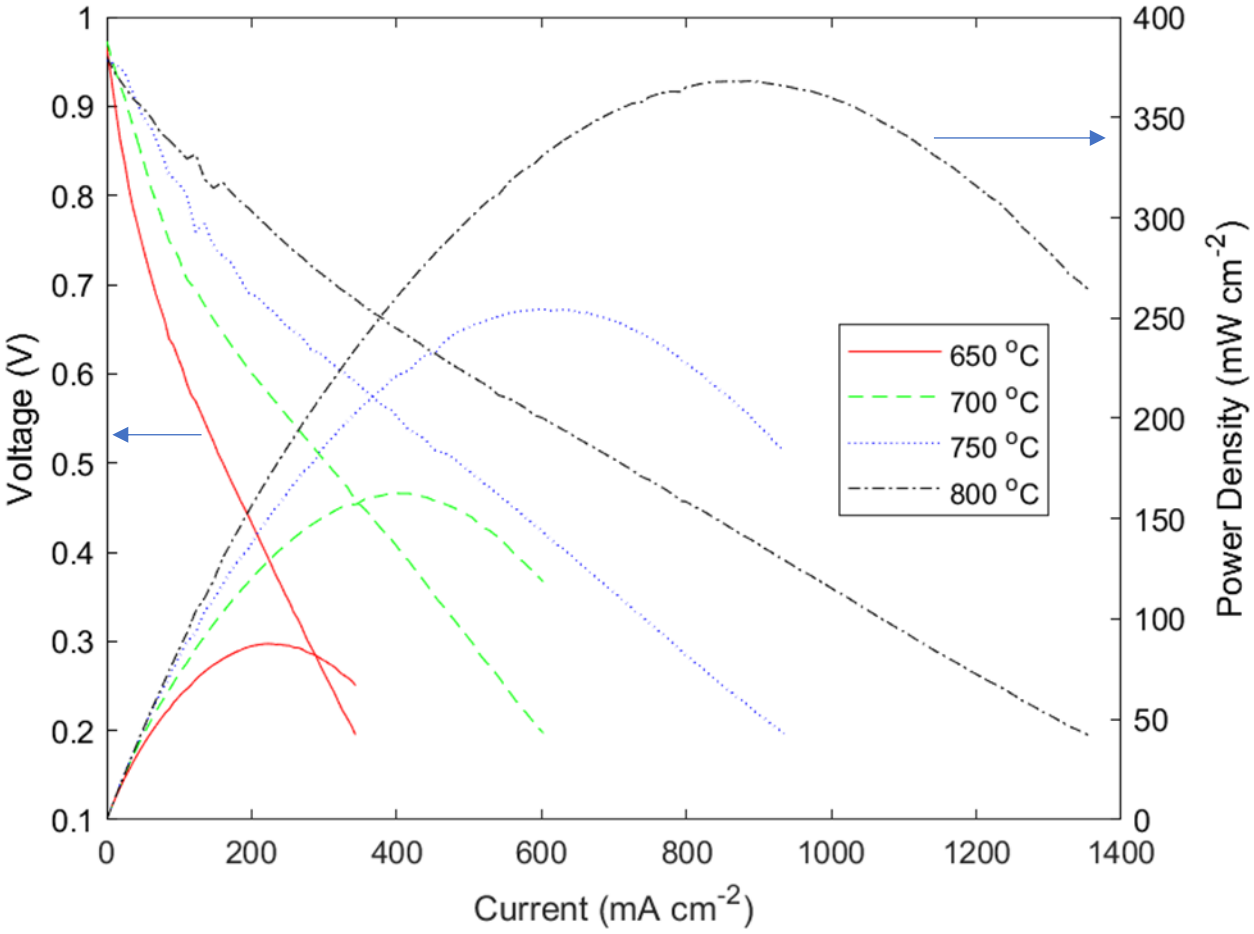

Figure 3.10: *Power and polarization curves for IC-tSOFC with hydrogen and air flow rates of 100 mL·min^{-1} and 235 mL·min^{-1}respectively. Adapted from* [50].

By varying the hydrogen flow rate from 25 mL·min^{-1} to 150 mL·min^{-1} it can be confirmed that effects related to high fuel utilization were not present. This is shown in Figure 3.11 where

the maximum fuel utilization corresponding to a hydrogen flow rate of 25 mL·min^{-1} is 47.6 %. For hydrogen flow rates of 100 mL·min^{-1} and above, the relative stability indicates effects from high fuel utilization disappear. Small variations persist due to minor changes in cell temperature as a result of changing gas flow rates, slight variation in furnace temperature etc.

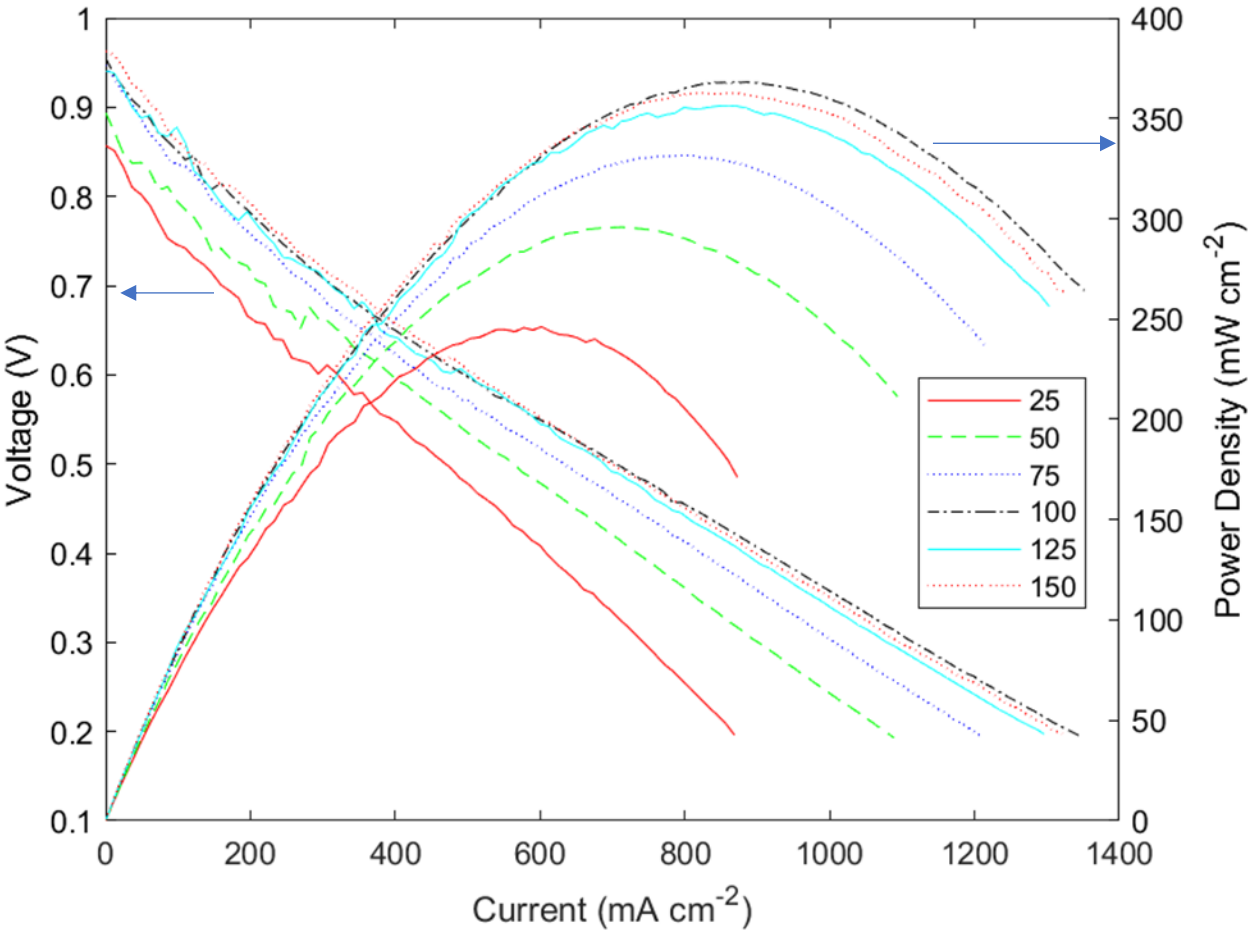

Figure 3.11: *Power and polarization curves for IC-tSOFC operating at 800 °C and 235 mL·min^{-1} air flow rate with varying hydrogen flow rate. Legend indicates hydrogen flow rate in mL·min^{-1}. Adapted from* [50].

Finally, Figure 3.12 shows the power and polarization curve for an EC-tSOFC operating at 800 °C supplied with 235 mL·min^{-1} and 100 mL·min^{-1} flow rates of air and hydrogen respectively. This cell obtained a peak power density of 478 mW·cm^{-2} at 800 °C. This is only 22.8 % higher than the IC-tSOFC peak power density and more recent work has shown improved

performance of IC-tSOFCs as manufacturing has improved [52,160]. The maximum fuel utilization was calculated to be 14.1 %, again showing low fuel utilization and therefore minimal losses unassociated with cell geometry. The differences between the IC-tSOFC and EC-tSOFC performance can be explained by the differences observed in Figure 3.8. The slightly higher cathode and anode densities partially impede mass transport within the cell and decrease the surface area of the accessible triple phase boundary slightly lowering overall cell power production.

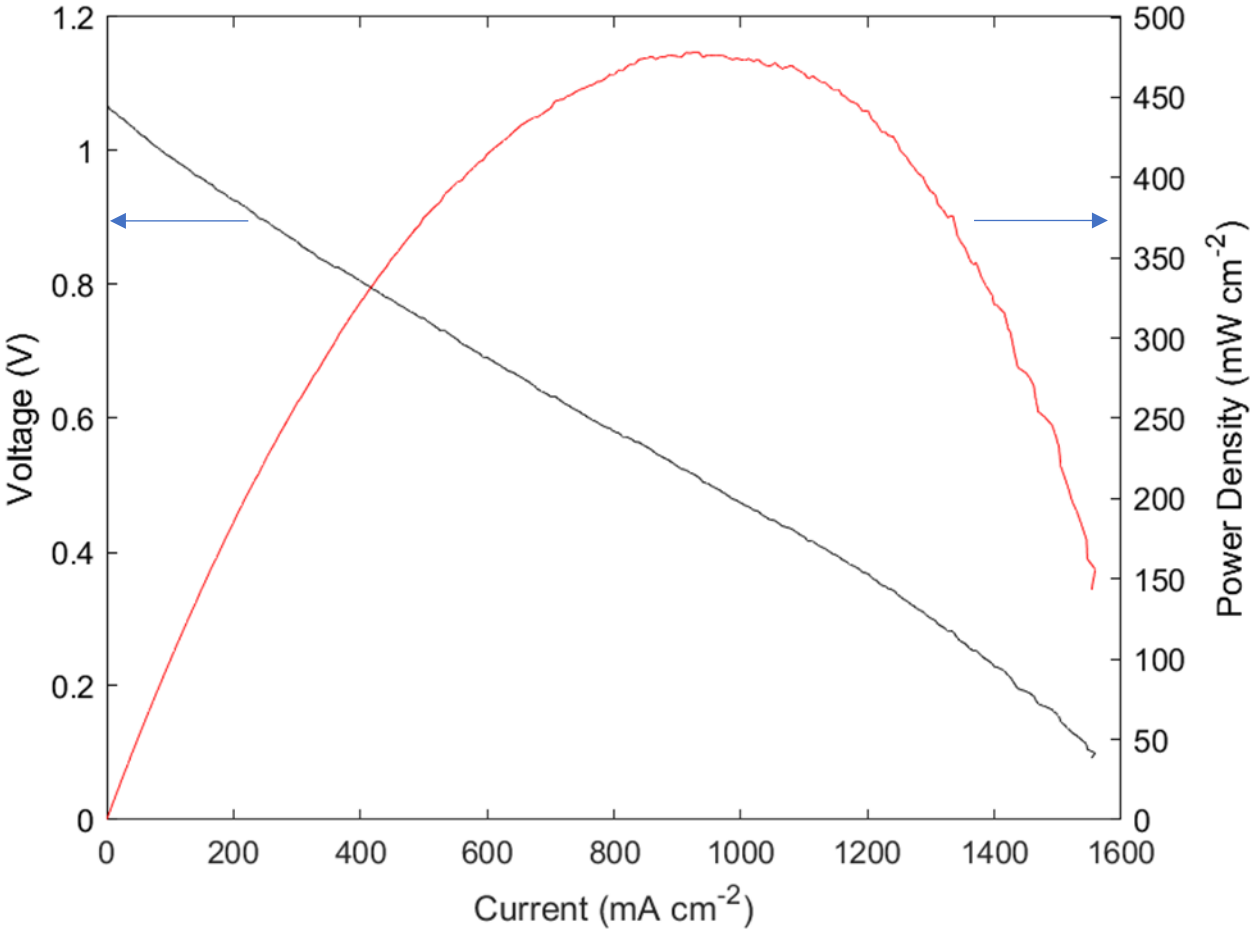

Figure 3.12: *Power density and polarization curve for EC-tSOFC operating at 800 °C supplied with 235 mL·min^{-1} and 100 mL·min^{-1} flow rates of air and hydrogen respectively. Adapted from* [50].

3.2 IC-tSOFC Performance on Simulated Exhaust

Following the initial publication of the work related to the development of the IC-tSOFC, further work was completed which demonstrated the performance of these cells in a variety of exhaust streams. This further indicatied its potential to successfully integrate into combustion systems. The first work looked at IC-tSOFC performance on methane exhaust as the equivalence ratio and temperature were changed [52]. In this work the IC-tSOFC was used as a testbed to perform an in-depth study into the effects of complicated exhaust compositions on SOFC performance. After this, simulated exhaust based on measured exhaust from small internal combustion engines was used again to evaluate IC-tSOFC performance within a potential application [160].

3.2.1 IC-tSOFC Performance on Methane Exhaust

The following work is adapted from the publication *Effects of Synthesis Gas Concentration, Composition, and Operational Time on Tubular Solid Oxide Fuel Cell Performance* published in Sustainability 14 (2022) [52].

To better understand the effects of dilution and unfavorable reaction kinetics expected with exhaust mixtures, comprehensive testing was performed using IC-tSOFCs as a platform for study. The testing setup was the same as for previous IC-tSOFC performance testing with pure hydrogen as a fuel as depicted in Figure 3.6. The composition of the gas mixture was obtained from NASA CEA as depicted in Figure 3.3 and confirmed with previous experimental work [19,21,141]. Two forms of testing were desired. The first was a dilute hydrogen baseline which replicated the dilution of fuels within the exhaust mixture at various equivalence ratios, but eliminated any effects of unfavorable reaction kinetics by replacing CO with an equal amount of hydrogen. Equal here is

determined by the moles of reactant necessary to produce the same number of free electrons, however, conveniently the oxidation of CO and hydrogen both involve two free electrons. The second form of testing was the simulated exhaust mixture consisting of the primary four exhaust species, hydrogen, CO, CO_2, and N_2. The resulting fuel mixtures fed to the cell are given in Table 2. As done with initial IC-tSOFC, temperature was also varied replicating the changes that may occur as the IC-tSOFC is moved within the exhaust stream to lower or higher temperature regions.

Table 2: *Gas flow rates for all simulated combustion exhaust and dilute hydrogen baseline tests. Equivalence ratio refers to the combustion reaction producing the set of exhaust mixtures. Adapted from* [52].

	Flow Rate (mL·min^{-1})					
	Simulated Combustion Exhaust				**Dilute Hydrogen**	
Equivalence Ratio	**H_2**	**CO**	**CO_2**	**N_2**	**H_2**	**N_2**
1.1	32	68	321	1855	100	2177
1.2	37	63	145	982	100	1128
1.3	42	58	86	670	100	757
1.4	46	54	59	513	100	572
1.5	50	50	44	420	100	462
1.6	52	48	34	356	100	390
1.7	55	45	28	311	100	339
1.8	57	43	24	277	100	301
1.9	58	42	21	250	100	271

The resulting power and polarization curves are shown in Figure 3.13 for the IC-tSOFC at 800 ^oC. Various behaviors of the cell may be observed. As expected, at high fuel utilization, in this case low equivalence ratio, power and voltage of the cell are comparably low. In particular, high fuel utilization causes high activation losses causing large drops in OCV as well as more rapid decreases in cell voltage [154]. For higher equivalence ratios, though these losses are smaller, mass concentration losses begin to become stronger. This can be seen by the decrease in slope at higher current densities. Interestingly, these losses appear delayed for the hydrogen baseline tests,

occurring at ~100 $mA \cdot cm^{-2}$ higher. This is most likely due to the easier transport of hydrogen through the anode due to its smaller size [161] and faster reaction kinetics [162].

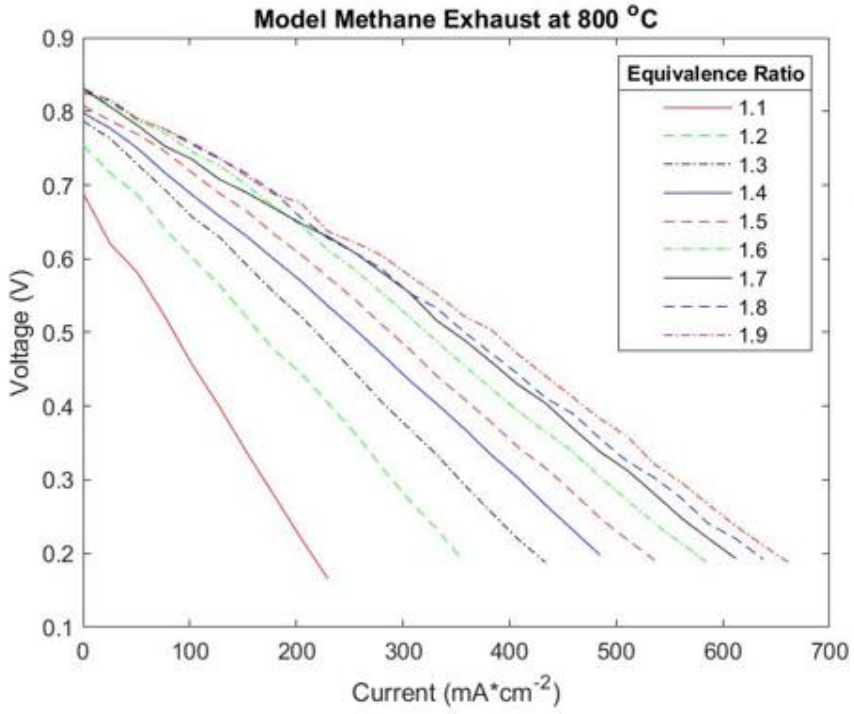
Model Methane Exhaust at 800 °C
Equivalence Ratio
1.1
1.2
1.3
1.4
1.5
1.6
1.7
1.8
1.9
Voltage (V)
Current (mA*cm-2)
0.9
0.8
0.7
0.6
0.5
0.4
0.3
0.2
0.1
0
100
200
300
400
500
600
700

(**a**)

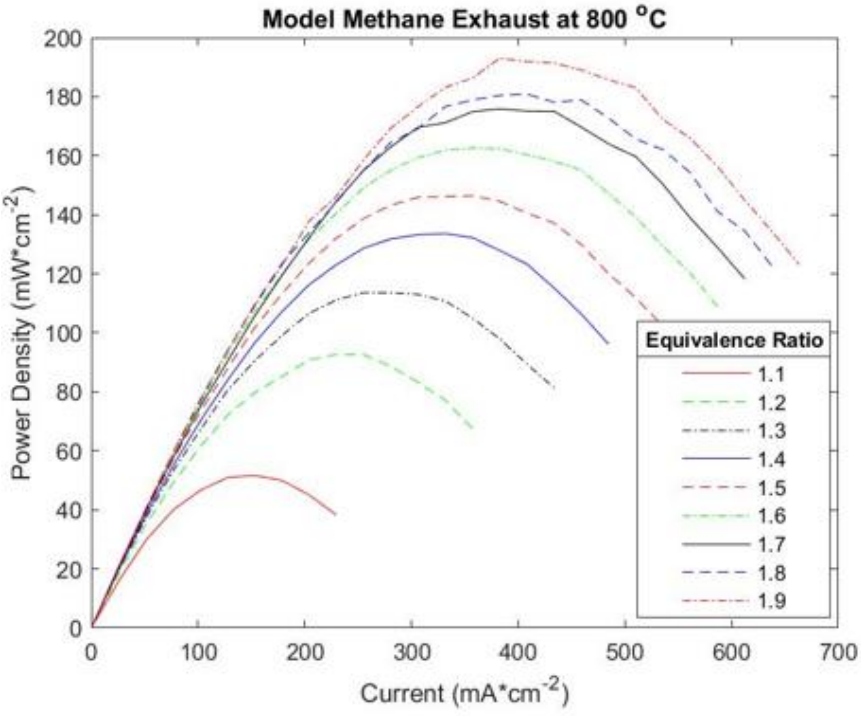
Model Methane Exhaust at 800 °C
Equivalence Ratio
1.1
1.2
1.3
1.4
1.5
1.6
1.7
1.8
1.9
Power Density (mW*cm-2)
Current (mA*cm-2)
200
180
160
140
120
100
80
60
40
20
0
0
100
200
300
400
500
600
700

(**b**)

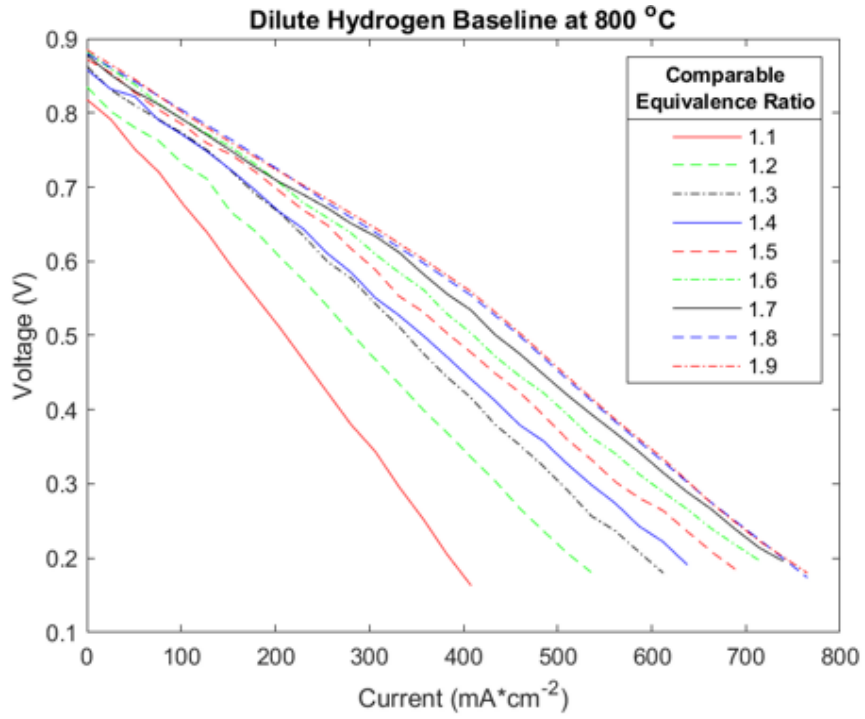

(c)

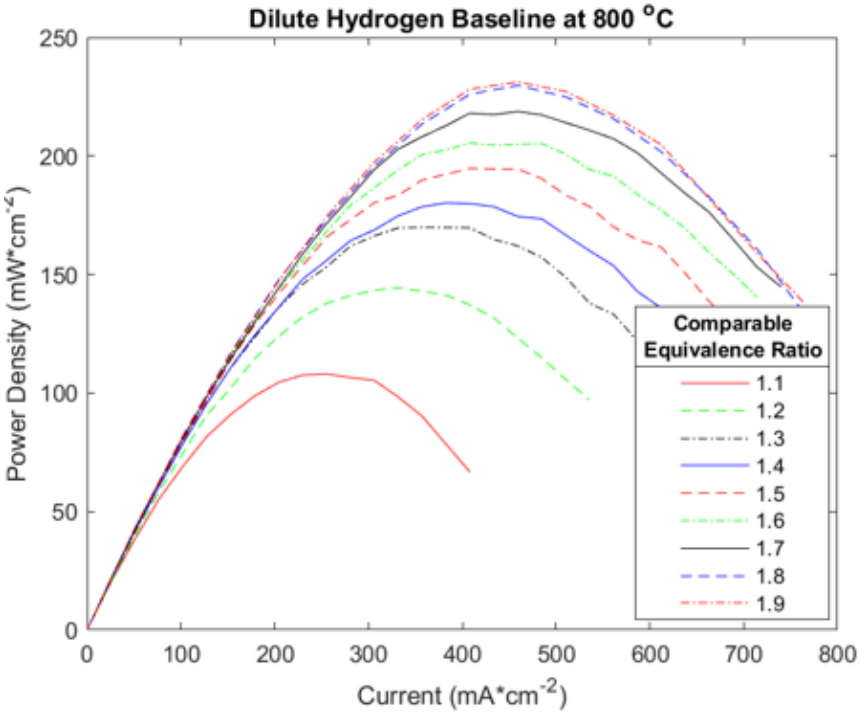

(d)

Figure 3.13: *Power and polarization curves for IC-tSOFC operating on simulated combustion exhaust and dilute hydrogen. Adapted from* [52].

To then analyze effects of fuel utilization, reaction kinetics, dilution, and temperature all OCVs and peak power densities were put together for all tests as shown in Figure 3.14. As predicted by the Nernst potential, the lower temperature tests have a higher OCV. As temperature increases, and ionic conductivity of the electrolyte increases, the peak power density similarly increases. Interestingly, though while the differences between OCVs remains approximately constant for all equivalence ratios, the same cannot be said for the peak power density. At higher equivalence ratios, the increase in peak power density for higher temperature tests becomes greater. This is most likely a result of the many advantageous effects higher temperatures have on SOFC performance. For simulated exhaust tests, the increase from low to high equivalence ratio at 800 ^{o}C is 38% while the increase at 650 ^{o}C is 18%. The similar increase for the hydrogen baseline test is 25 % and 12 % respectively. This indicates that in addition to improved ionic conductivity of the electrolyte, improved reaction kinetics are occurring as thermal energy to promote reactions increases. The increase is higher for the simulated exhaust because reactions involving CO are slower and have higher activation energies.

Overall, this study highlighted the impacts of complex fuel mixtures on SOFC performance. When operating with simulated exhaust as fuel these effects are significant and must be accounted for. In relation to IC-tSOFCs, this study demonstrated the reliability with which these cells can be used as a test platform and as a mature cell technology. Finally, the testing methodology where effects of dilution, reaction kinetics, and temperature were isolated was a novel procedure which has been carried on with other exhaust mixtures.

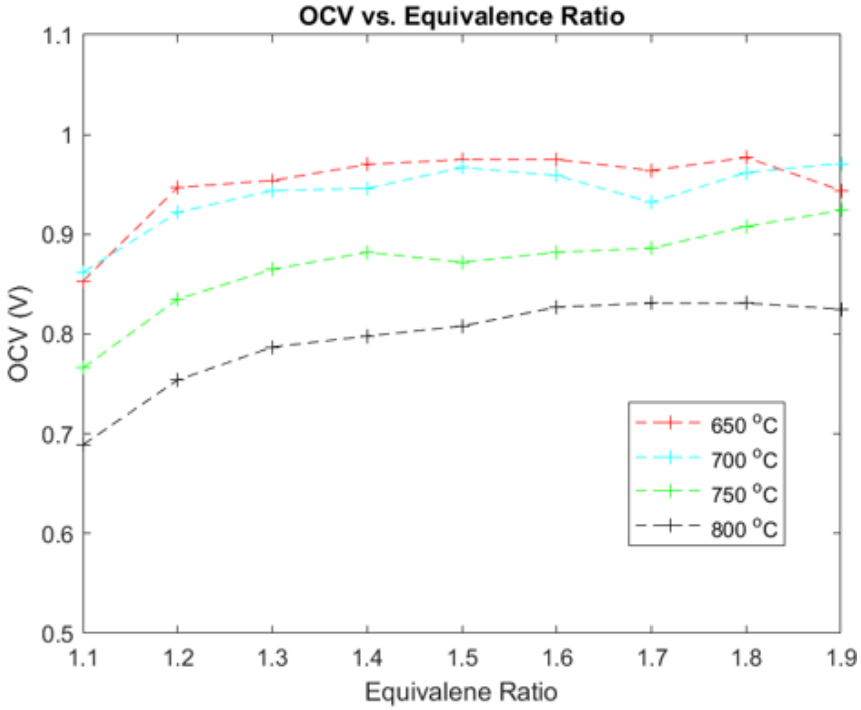
OCV vs. Equivalence Ratio
OCV (V)
Equivalene Ratio
650 °C
700 °C
750 °C
800 °C

(**a**)

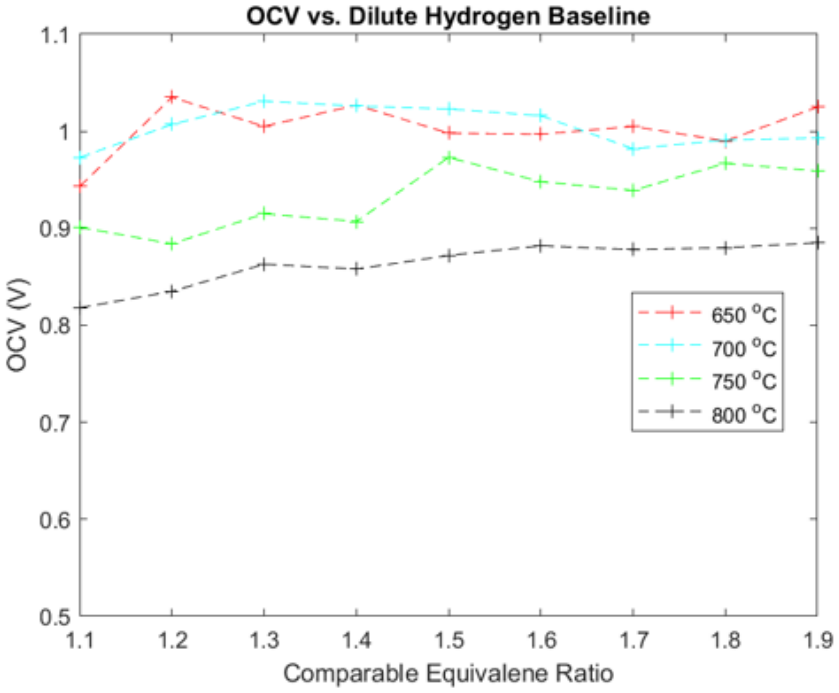
OCV vs. Dilute Hydrogen Baseline
OCV (V)
Comparable Equivalene Ratio
650 °C
700 °C
750 °C
800 °C

(**b**)

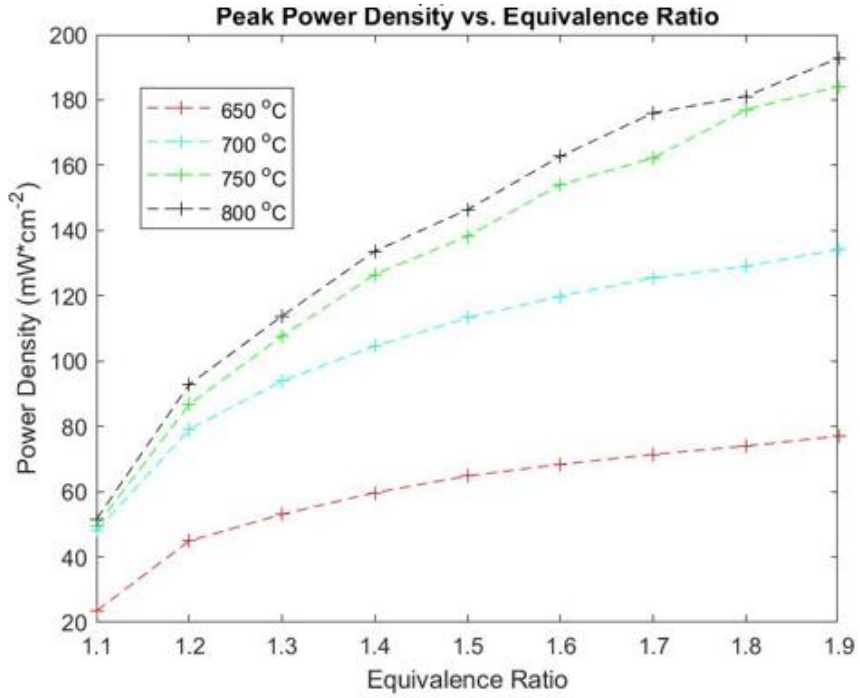

(c)

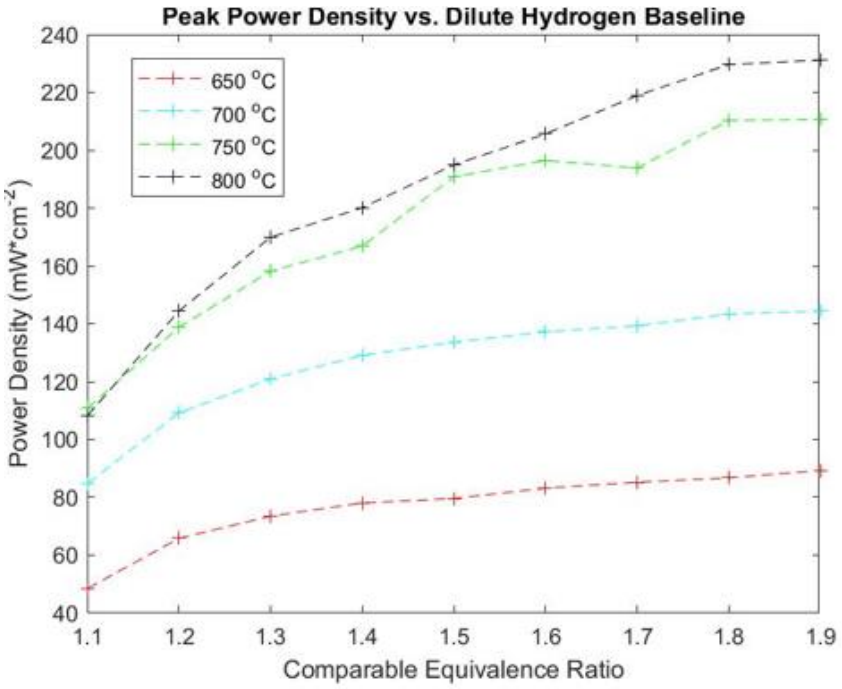

(d)

Figure 3.14: *OCV and peak power densities for all simulated combustion exhaust and dilute hydrogen baseline tests with IC-tSOFC. Adapted from* [52].

3.2.2 IC-tSOFC Performance on Simulated Two-Stroke Internal Combustion Engine Exhaust

The following work is adapted from the publication *Internal Cathode Tubular Solid Oxide Fuel Cell Operating on Simulated Two-Stroke Internal Combustion Engine Exhaust* published in Proceedings of the Nineteenth International Conference on Flow Dynamics (2022) [160].

The most recent work utilizing IC-tSOFCs investigated hybrid systems which combined SOFC stacks with small two-stroke internal combustion engines. The ultimate goal of this project is to produce high efficiency hydrocarbon powered unmanned aerial vehicles with extremely long flight time capabilities. The exhaust mixture was obtained from previous work using 70:30 methanol to nitromethane fuel at an approximate equivalence ratio of 1.6 [163]. Following the procedure used in the previous study involving IC-tSOFC performance on methane exhaust [52], pure hydrogen, dilute hydrogen, and simulated exhaust mixtures were used to examine the performance of the IC-tSOFC. Interestingly, two-stroke ICEs tend to exhaust partially reacted fuel into the exhaust stream. This appears as a relatively high concentration of methane in the simulated exhaust mixture. Though methane cannot be directly reacted by SOFCs, but it can be internally reformed via steam reformation or partial combustion resulting in syngas [10,19,61].

Table 3: *Simulated exhaust, dilute baseline, and pure baseline gas mixtures for testing of IC-tSOFC with two-stroke ICE. Adapted from* [160].

Test	Gas	Flow rate (mL·min^{-1})
Simulated Exhaust	H_2	17.7
	CH_4	16.8
	N_2	49.0
	Air	75.8
	CO	15.2
	CO_2	82.2
	Total	256.7
Dilute Baseline	H_2	100.0
	N_2	156.7
Pure Baseline	H_2	100.0

Ultimately, the inclusion of methane in the simulated exhaust had highly detrimental effects on the power production capabilities and OCV of the IC-tSOFC as seen in Figure 3.15. The dilution effects and unfavorable reaction kinetics previously observed [52] were more significant in this system. The IC-tSOFC, however, performed very well with a peak power density of 415 mW·cm^{-2} when operating on pure hydrogen. This is a 14 % increase from the initial peak power density observed during development of the first IC-tSOFCs [50] indicating continued improvement of the cell.

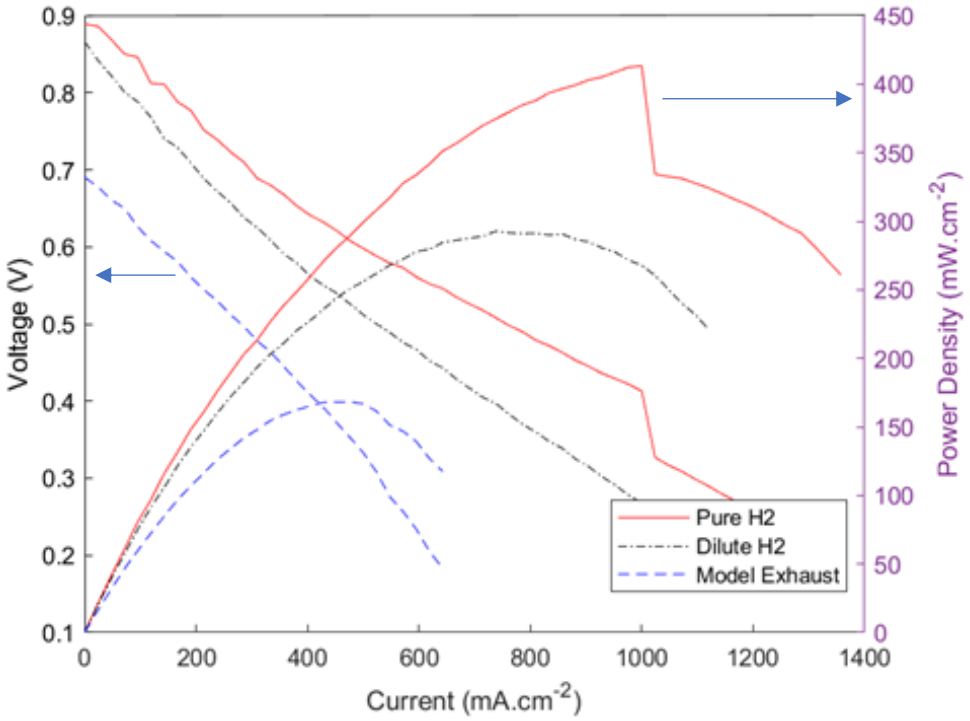

Figure 3.15: *Power and polarization curves for IC-tSOFC operating on model (simulated) exhaust from two-stroke ICE, dilute baseline, and pure hydrogen baseline tests at 800 °C. Adapted from* [160].

3.3 Defects Complicating Development of the IC-tSOFC

As mentioned in section 3.1, development of the IC-tSOFC was hindered by the frequent presence of a fracture within the cell. To remedy this issue, extended sintering procedures were used to promote creep stress relaxation as described in section 3.1.3. The cause for this defect, however, was more elusive than the solution. The following discussion will describe the defect in detail, introduce a potential cause for the defect, and then introduce the idea of utilizing these residual stresses for constructive means.

3.3.1 Identification of Defect

The following work is adapted from *Integration of Novel Geometry Solid Oxide Fuel Cells into A Residential Furnace/Boiler* from Proceedings of the ASME 2020 International Mechanical Engineering Congress and Exposition [164].

Figure 3.16 shows the defect in question. The SEM image depicts a cross-section of the IC-tSOFC with a crack that penetrates from the inner cathode to the outer anode and goes along the entire length of the tube. This crack alone causes significant issues with cell performance. The electrolyte plays the vital role of maintaining a gas tight seal between the oxidant and fuel streams as described in section 2.1.1. When this seal is broken, oxidant and fuel may mix within the cell. At high temperatures this can result in combustion reactions occurring within the cell, consuming otherwise usable fuel, and creating high local heat. This localized heating then causes significant thermal stress for the cell resulting in failure.

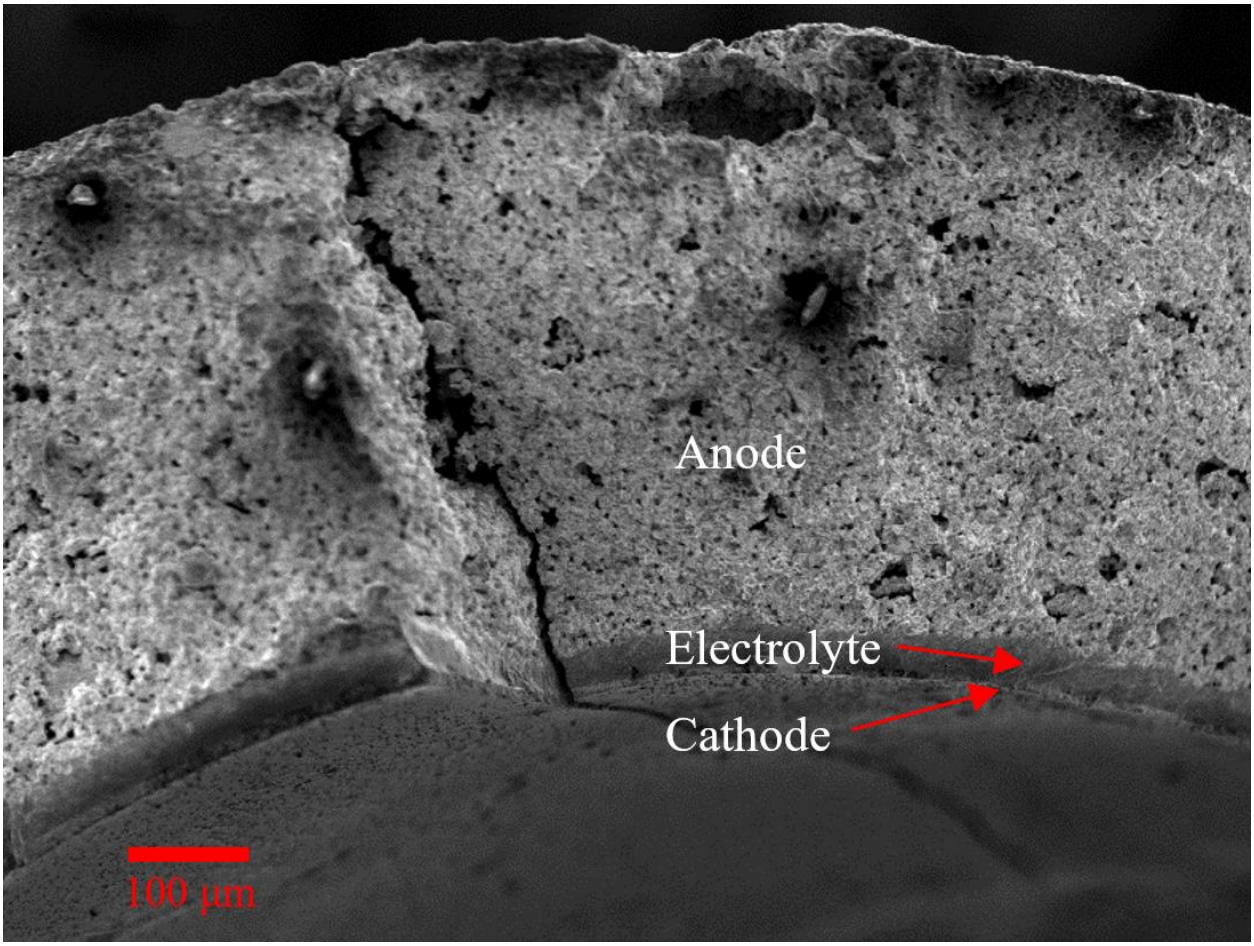

Figure 3.16: *SEM image showing longitudinal fracture of IC-tSOFC going through anode, electrolyte, and cathode layers. Adapted from* [164].

Beyond these potential issues with performance, however, issues were observed immediately following the cathode deposition and sinter. This issue is depicted in Figure 3.17. The crack formed during the electrolyte-anode cosinter and so during the fill coating of the cathode slurry, some slurry was able to penetrate the crack. The cathode was then able to make direct contact with the anode. This contact resulted in shorting of the cell as was consistently observed during testing.

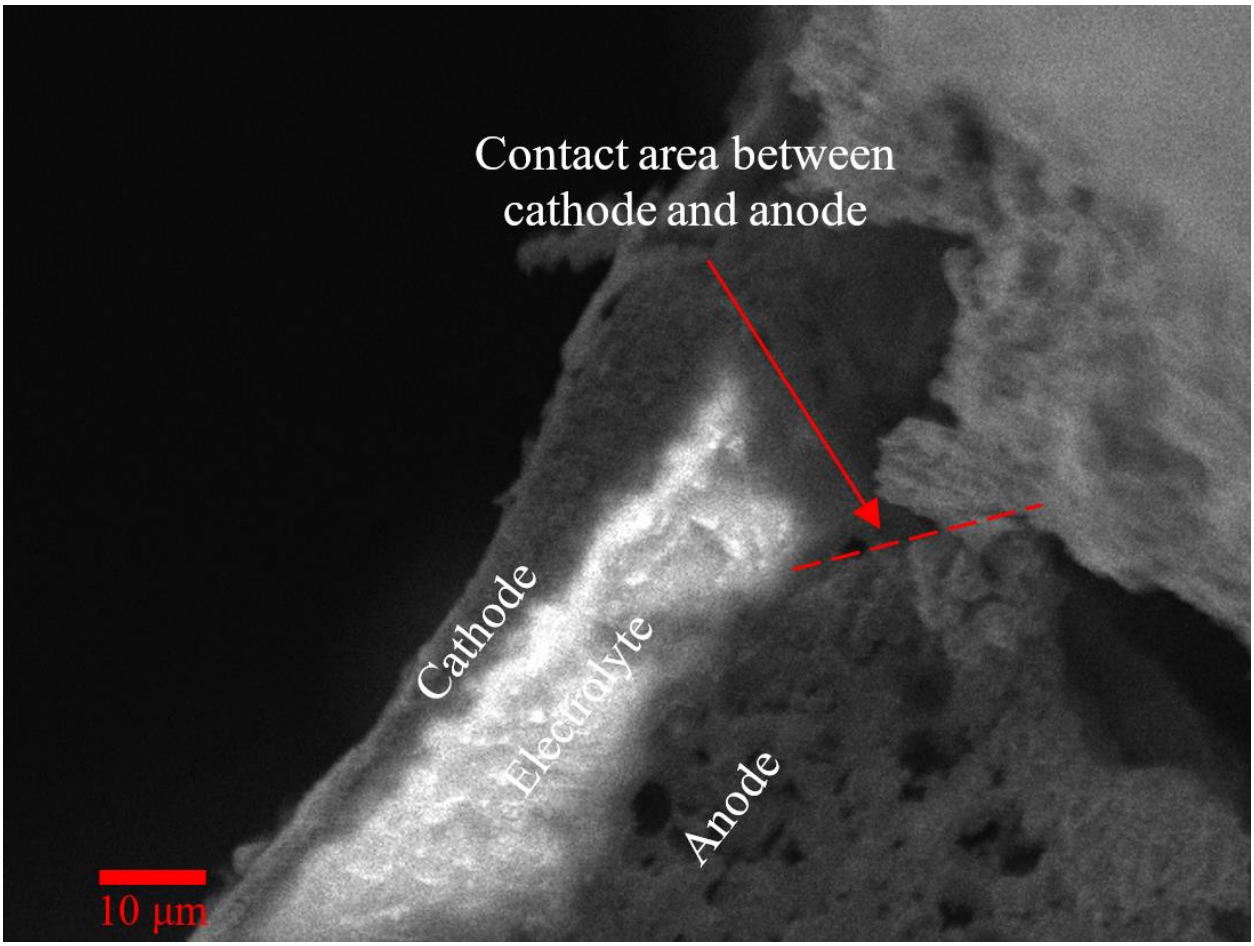

Figure 3.17: *SEM image showing cross-section of IC-tSOFC with contact between cathode and anode labeled. Adapted from* [164].

Following the successful development of the IC-tSOFC, the question remained why this geometry of cell was so vulnerable to this defect. With the information that the defect occurred during the anode-electrolyte cosinter, that it was unique to the IC-tSOFC geometry, and that it could be remedied by allowing small amounts of strain to relax residual stresses, FEM modeling was used to identify the probable cause.

3.3.2 Identifying the Cause of Fracture

Models of the IC-tSOFC and EC-tSOFC were developed in ABAQUS and the material properties obtained from literature described in Table 1 were used for the anode and electrolyte.

Half of the tubular cross-section of the cell was modeled with vertical symmetry. The top node at this symmetry line was fully constrained and the rest of the symmetry line was restricted from movement in the x-direction. The composite was then initiated with a temperature of 1350 ^{o}C and cooled to 298 ^{o}C in a static process. The residual stresses are depicted in Figure 3.18.

For the IC-tSOFC, the electrolyte film pulls the anode towards the center of the tube so $\sigma_{rr} > 0$, but compresses the anode in the circumferential direction as it shrinks so $\sigma_{\theta\theta} < 0$. For the EC-tSOFC, the electrolyte pushes the anode towards the center of the tube so $\sigma_{rr} < 0$, and compresses the anode in the circumferential direction as it shrinks so $\sigma_{\theta\theta} < 0$. This is shown in the contours in Figure 3.18 depicting σ_{rr}. The key characteristic observed here is the absence of tensile stress within the anode for the EC-tSOFCs. Though the electrolyte experiences tensile stresses, the electrolyte is extremely dense and largely free of defects which contribute to stress concentrations. As a result, this layer is mechanically robust as discussed in relation to electrolyte supported cells in section 2.1.1. The anode, however, is by design extremely porous and therefore possesses innumerable locations where significant stress concentration can occur. The presence of tensile stresses within the anode for IC-tSOFCs therefore introduces a susceptibility to fracture that is not experienced by the EC-tSOFCs with anodes purely in compression. This is because ceramics are brittle materials with much higher compressive ultimate strengths than tensile ultimate strengths [165]. The mixing of stress directions also introduces a higher susceptibility to fracture as the Von Mises stress for this combination is larger than for two compressive stresses or two tensile stresses.

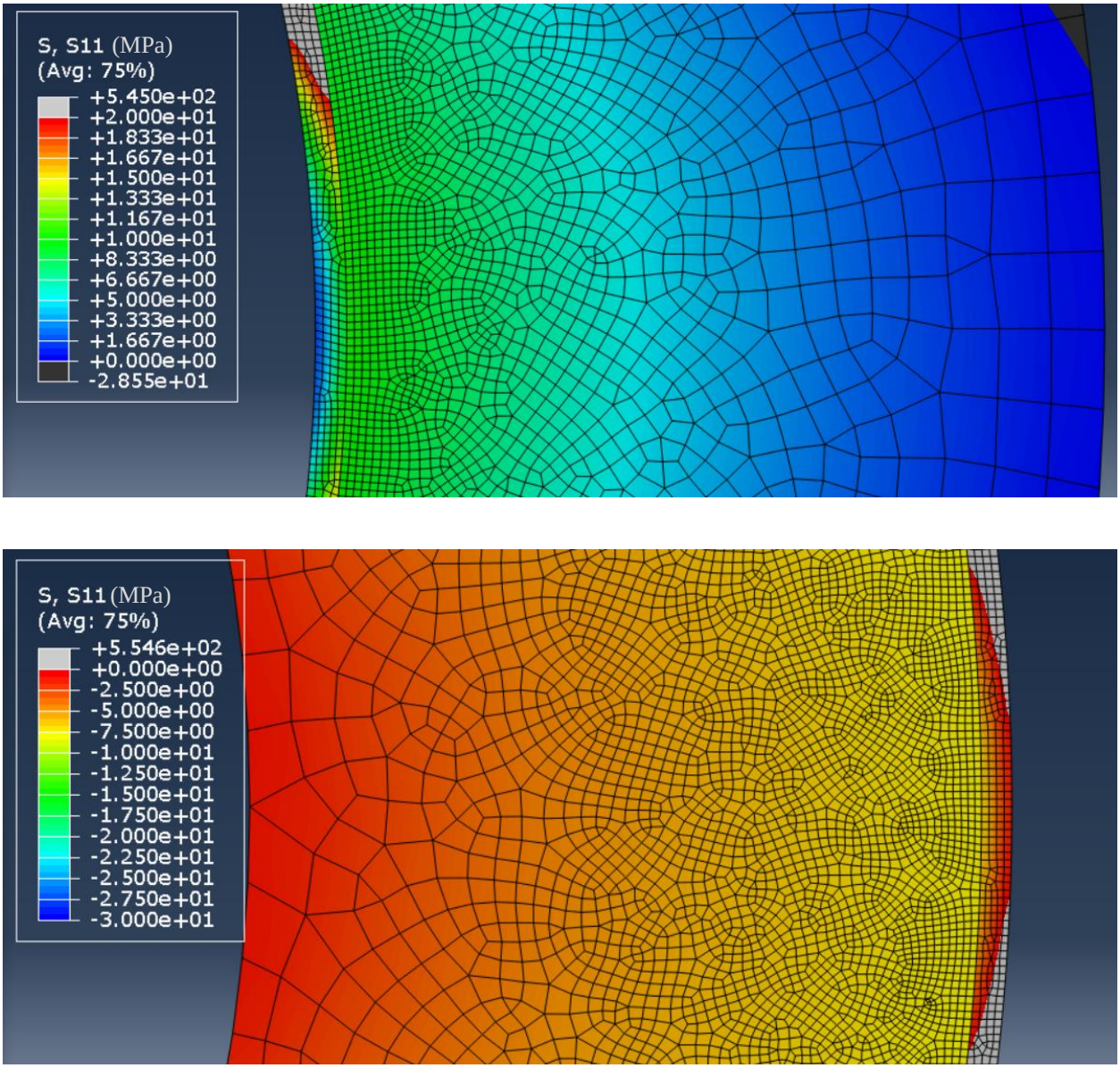

Figure 3.18: *FEM models of IC-tSOFC (top) and EC-tSOFC (bottom) colored with magnitude of* $\boldsymbol{\sigma_{11}}$ *in MPa.*

To further support this explanation for the fracture of IC-tSOFCs, the relationship between electrolyte thickness and the likelihood of fracture was investigated. As will be discussed in relation to Timoshenko's work with bimetal thermostats [39], for bimaterial composites, as the contracting material increases in thickness relative to the substrate, the stresses present in the substrate also increase. In the case of the IC-tSOFC where the bimaterial composite is

geometrically constrained from deforming, this increase in residual stress increases the likelihood of failure. As seen in Figure 3.19, an increase in layers of electrolyte generally leads to an increase in failure rate of IC-tSOFCs as expected when using an unmodified sintering procedure. Using the empirically determined relationship between number of electrolyte depositions and total layer thickness, it can also be seen that electrolyte thicknesses above ~30 µm consistently result in critical stresses within IC-tSOFCs.

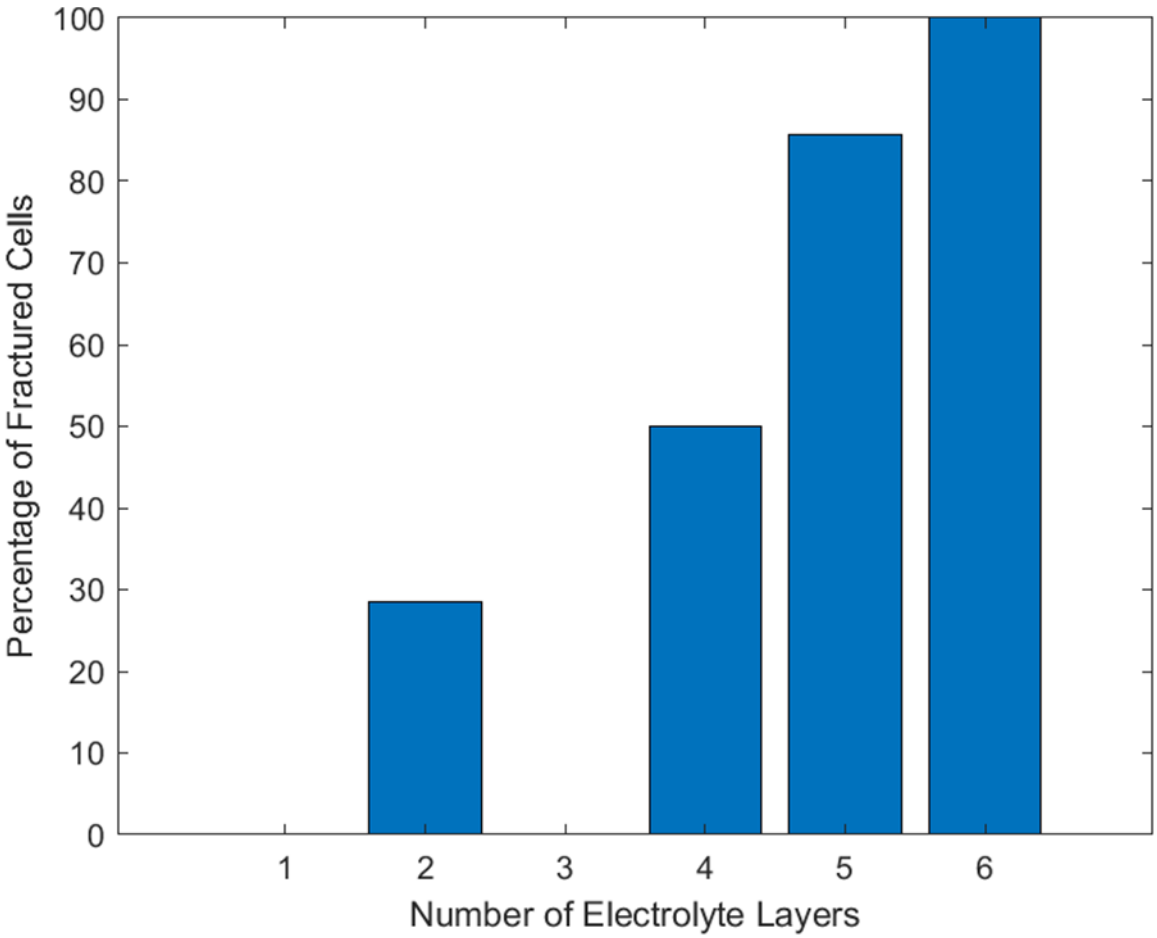

Figure 3.19: *Bar plot showing fracture rate of IC-tSOFCs with increasing electrolyte thickness.*

4. Development of Self-Shaping Ceramics

The defects that complicated development of the IC-tSOFC revealed that the power of the residual stresses experienced by MCCs are typically ignored because geometric constraints hide any deformation or are avoided through the use of sintering procedures which prevent curvature [9,140]. Chapter 3 also showed the impact a change in cell architecture can have. By turning the traditional EC-tSOFC inside out, direct integration into combustion chambers and other fuel containing environments became possible. By combining these two ideas, a much more impactful effect may be achieved. By utilizing these residual stresses that plague IC-tSOFCs to control not just cell architecture, but entire cell geometry, entirely new ceramic shapes can be obtained, unleashing completely new applications for SOFCs, MCCs, and ceramics in general.

Beyond developing the experimental techniques to produce real-world samples, it was equally, if not more important, to be able to reliably predict and design objects using this process. As such, one of the goals of this work was to use analytical and FEM modeling developed in relation to easily deformable materials like polymers and metals to predict the behavior of ceramics. Comparisons were made between materials and modeling approaches to assess any behaviors unique to ceramics and to confirm the ability to use the wealth of knowledge already available for bilayer shrinkage driven self-shaping.

4.1 Observation of Bilayer Shrinkage in Ceramics

As has been introduced in section 2.3, bilayer shrinkage is the mechanism used to form self-shaping ceramics. For SOFC materials, the possibility to utilize this mechanism was first illustrated in attempts to make IC-tSOFCs with electrolyte buffer layers. As discussed in section 2.1.1, by adding a GDC or SDC layer to a YSZ electrolyte, an LSCF cathode may be used in place

of an LSM cathode, achieving higher cell performance. Typically, this buffer is ~ 2 µm thick or less [48]. However, this early attempt to deposit a buffer layer with the fill coating procedure resulted in a GDC layer thickness of ~10 µm. As shown in Table 1, the TEC of GDC is greater than that of YSZ for all temperatures experienced during sintering. As a result, the GDC layer will shrink more than the YSZ layer it is deposited onto. For the relatively thick layers of GDC deposited in this initial attempt, an unexpected behavior was observed as shown in Figure 4.1. This behavior was deformation due to bilayer shrinkage.

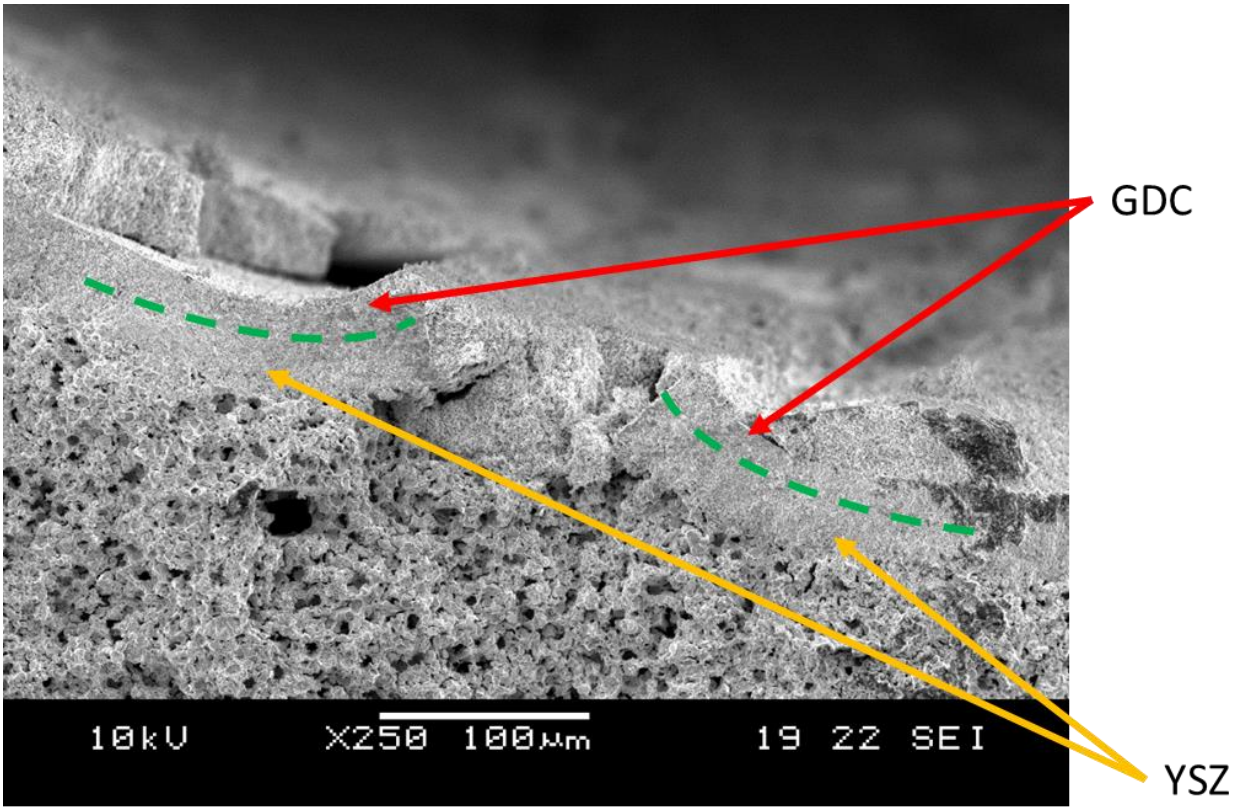

Figure 4.1: *SEM image showing IC-tSOFC with YSZ-GDC buffer layer electrolyte. As a result of mismatched TECs, the electrolyte has deformed in the direction of the GDC.*

For the buffer layer cells, this behavior was an issue which current work is attempting to resolve. More beneficially, it illustrated the highly deformable nature of ceramics during sintering

as well as the high strains possible with bilayer shrinkage. As such, it became desirable to use this technique to control the overall 3D geometry of MCCs.

4.2 Motivation for Forming Self-Shaping Ceramics

As briefly mentioned in section 2.3, traditional methods for manufacturing ceramics are limited in terms of the geometries they can form and the scale of the finished part. It is desirable to expand the manufacturing methods available to form ceramic parts so that SOFCs, MCCs, and ceramics in general can be better suited to their intended application.

For SOFCs, several benefits could be achieved by expanding beyond the currently available planar and tubular cell geometries. The first is obtaining high active surface areas within a small volume. This goal is extremely important in relation to recent work completed in the COMER, investigating SOFC materials as non-precious metal replacements for platinum catalytic converters [83]. The higher the surface area, the more that harmful emissions can be treated. Without the need to generate electrical power, many of the strict requirements for cell architecture are removed, allowing for more flexibility in the membrane design. As such, a possible geometry for this membrane could be a Swiss roll. Previous work with combustion systems has shown this geometry can aid in not only obtaining high surface area to volume ratios, but also minimizing heat transfer to the surroundings, promoting the high temperature reactions which reduce harmful NO_x emissions [166,167]. For ceramics in general, this geometry cannot be produced. Thin-walled green bodies need physical support until they are sintered, but encapsulation prevents supports from being provided. One of the only viable ways to form a ceramic Swiss roll would be to have it shape itself during sintering.

Second, in addition to high surface area packing, curvature of thin sheets can yield mechanical benefits. Large thin sheets of brittle materials are extremely prone to cracking. Simply lifting a sintered planar sheet becomes a challenging task. However, by introducing curvature in one direction, rigidity may be obtained in the perpendicular direction as described in section 2.3.1. Following Gauss, if an inextensible sheet is to retain its zero Gaussian curvature, but is bent in one direction, the curvature in the perpendicular direction must remain zero [126]. In the case of the Swiss roll catalytic converter, this would be highly beneficial. The structure could be secured at the top and bottom of the roll but would need to be mechanically robust to perturbations between these boundaries. The roll would curve perpendicular to this unsupported direction improving its mechanical strength. Comparable planar sheets would not possess this stiffening and therefore remain vulnerable to damage. This would be particularly problematic for many of the portable applications this emission reduction device would be used in. More generally, this can introduce stiffness to SOFC stacks which otherwise rely on interconnects to ensure that all components remain intact.

Third, in addition to mechanical support, interconnects within SOFC stacks provide routing of fuel, oxidant, and exhaust gases to and from the cell. Interconnects, however, are complex, heavy, and are made of different materials than the SOFC itself. This contributes to high cost and high weight of the overall system as well thermal degradation during rapid thermal cycling [168,169]. Some work has investigated the removal of interconnects by producing extremely porous anode and cathodes through freeze casting [170], but this technique is difficult to execute. By using self-shaping ceramics, SOFC stacks could be produced which have curvature induced stiffness increasing mechanical rigidity of the stack, but these curves could also produce

channels through which gases could be transported. A possible cell geometry for interconnect-free SOFC stacks could be the wave cell depicted in Figure 4.2.

Figure 4.2: *Image of wave cell produced using bilayer shrinkage driven self-shaping. Scale bar is 5 mm.*

4.3 Method for Producing Self-Shaping Ceramics

The general procedure to form self-shaping ceramics using bilayer shrinkage began with the formation of the substrate and is shown in Figure 4.3. To obtain a sufficiently thin and uniform substrate, tape casting was the preferred method. Tape cast sheets are also highly flexible and able to be cut with scissors or razor blades allowing for easy shaping of the substrate into a variety of 2D shapes. As discussed in section 2.2.1, the thickness of the final ceramic sheet varies greatly from the height of the doctor blade used to form the initial wet tape. For example, to obtain a green body thickness of 300 µm, the final doctor blade must be set to 750 µm. The initial shaping doctor blade would be set to twice that height at 1500 µm. Of course, the sintered film would be thinner than 300 µm, ultimately necessitating the use of SEM or physical measurement as will be discussed.

The ceramic slurry was prepared using standard procedures by mixing NiO-YSZ powder with solvents such as toluene, and binders. Mixing was carried out for at least 48 hours. To eliminate air bubbles, the slurry was allowed to rest for approximately 15 minutes after mixing

and before it was poured into the tape caster hopper. The tape was then cast and allowed to dry within a well-ventilated chamber for approximately 30 minutes before being collected on a roll.

The prepared tape was then cut into approximately 10 x 10 cm sections. During aerosol spraying, the extremely light ceramic sheets must be attached to the hot plate base with heat resistant Kapton tape, so it is easier to spray larger sheets. It is then cut into the desired shape following spraying. For sheets sprayed with a mask, however, the ceramic substrate may be cut into its final shape as the mask serves the dual purpose of controlling the deposited film pattern as well as restraining the ceramic substrate.

The sheets were then sprayed by a Sonotek ultrasonic spray coater with hotplate set to 100 ^{o}C. Approximately 420 layers were sprayed onto the substrates to achieve a film thickness of 20 μm. However, for the various experiments that will follow, the number of layers was varied to similarly vary the thickness of the deposited film. For substrates receiving film on both sides of the substrate, such as for the wave cell depicted in Figure 4.3, this process was repeated after flipping the substrate and aligning the mask as necessary.

Once the substrates were sprayed with film, they were sintered. Unlike with IC-tSOFCs, the sintering procedure was unchanged from standard procedure used in SOFC processing as reported in previous work [18,59,60]. Sintering began by heating to 600 ^{o}C at a rate of 2.5 ^{o}C·min^{-1}. The temperature was then held at 600 ^{o}C for half an hour. After the hold, the furnace temperature was brought to 1350 ^{o}C at a rate of 4.2 ^{o}C·min^{-1}. This temperature was held for 4 hours. The samples were cooled to 800 ^{o}C at a rate of 6.1 ^{o}C·min^{-1}. Final cooling to room temperature was carried out at a rate of 2.5 ^{o}C·min^{-1}.

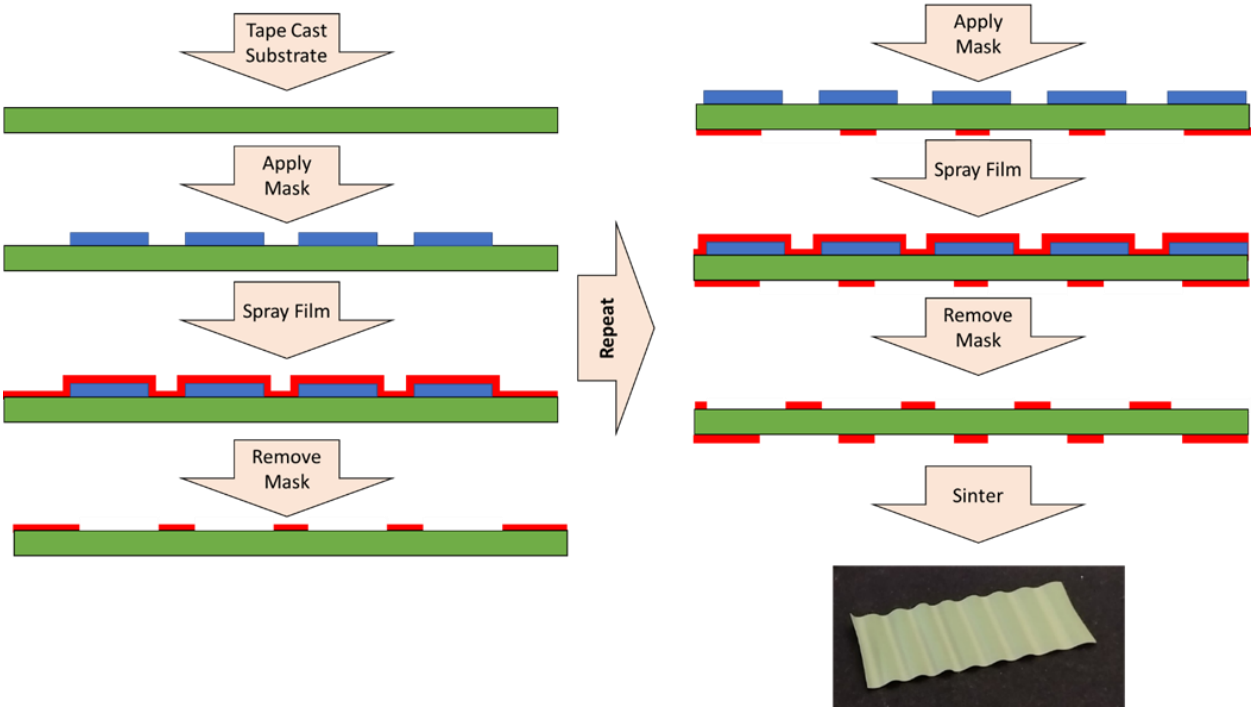

Figure 4.3: *Flow diagram showing manufacturing of self-shaping ceramics. Substrate is shown in green, film is shown in red, and mask is shown in blue. Provisional patent SU#2023-007 – Bilayer Shrinkage to Assemble Complex Ceramic Shapes. Adapted from* [171].

4.3.1 Method for Producing and Analyzing Canonical Shapes Experiencing Homogeneous Bilayer Shrinkage

For much of the experimental analysis carried out in this work, a simplified version of the methods shown in Figure 4.3 were used. Much of the previous work investigating bilayer shrinkage has been carried out with homogeneous bilayer shrinkage [38,41,42,107] and so initial studies regarding self-shaping ceramics were intended to replicate these results in other material systems. Future work will thoroughly study the more complicated anisotropic bilayer shrinkage using patterned films [115,172] which have recently begun to be investigated with soft materials.

This simplified method, along with the curvature of the final shape, was used to carry out much of the following quantitative analysis is depicted in Figure 4.4. For these samples, no masks were used. After spraying, canonical shapes including disks and rectangles were cut using circular

dies as well as rectangular stencils. After sintering, the samples were analyzed. For samples which curved more than 180^{o}, the curvature could easily be obtained by measuring the diameter. For samples that curved less than that, the length of the arc and the chord length needed to be obtained. The curvature of the sample can then be obtained from these two quantities; however, the resulting relationship is implicit as follows:

$$\frac{2\sin\left(\frac{\theta}{2}\right)}{\theta} = \frac{l}{s}, r = \frac{s}{\theta} \qquad (4.1)$$

This was then solved using Newton's method where an initial estimate of the curvature was made by fitting two right triangles into the arc with hypotenuse length equal to half the arc length and leg length equal to half the chord length. Qualitative analysis of the samples was simply carried out using digital photography.

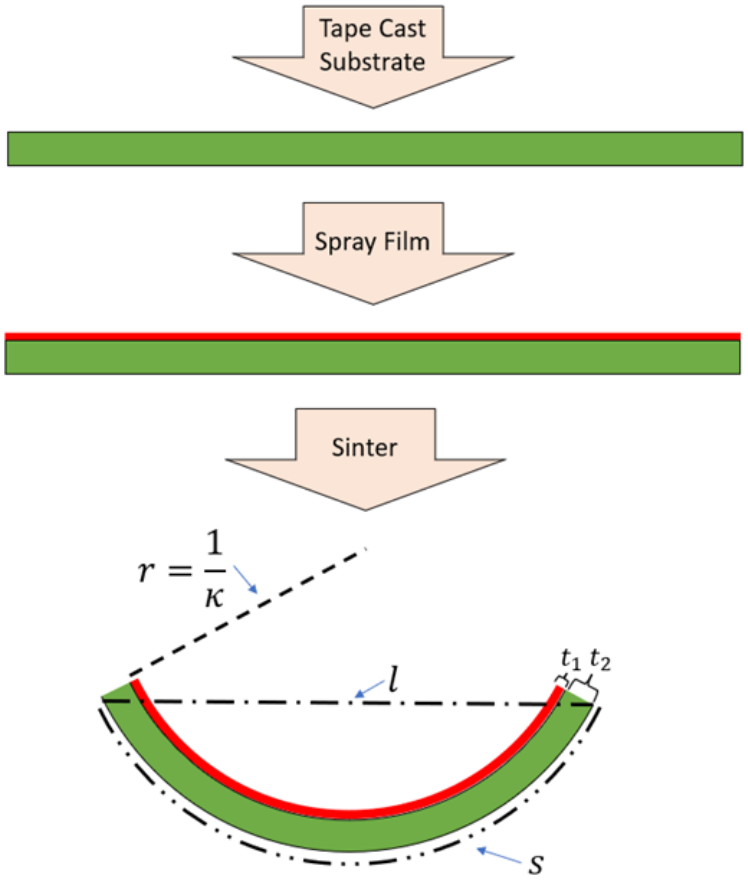

Figure 4.4: *Flow diagram showing process for forming homogeneous bilayer shrinkage driven self-shaping ceramics. Curvature* $\boldsymbol{\kappa}$ *is shown in addition to measure quantities including chord length* $\boldsymbol{l}$*, arc length* $\boldsymbol{s}$ *and thickness of the film and substrate respectively* $\boldsymbol{t_1}, \boldsymbol{t_2}$*. Adapted from* [173].

To obtain the thickness of the substrate and film layers, SEM was used. Sintered and deformed samples were fractured to expose cross-sections of the composite. These were then imaged in a JEOL-JSM-5600 SEM in secondary electron imaging mode. This is shown in Figure 4.5. Thickness measurements were obtained using image processing software ImageJ. The thickness of the substrate and film were measured in five different locations, then averaged.

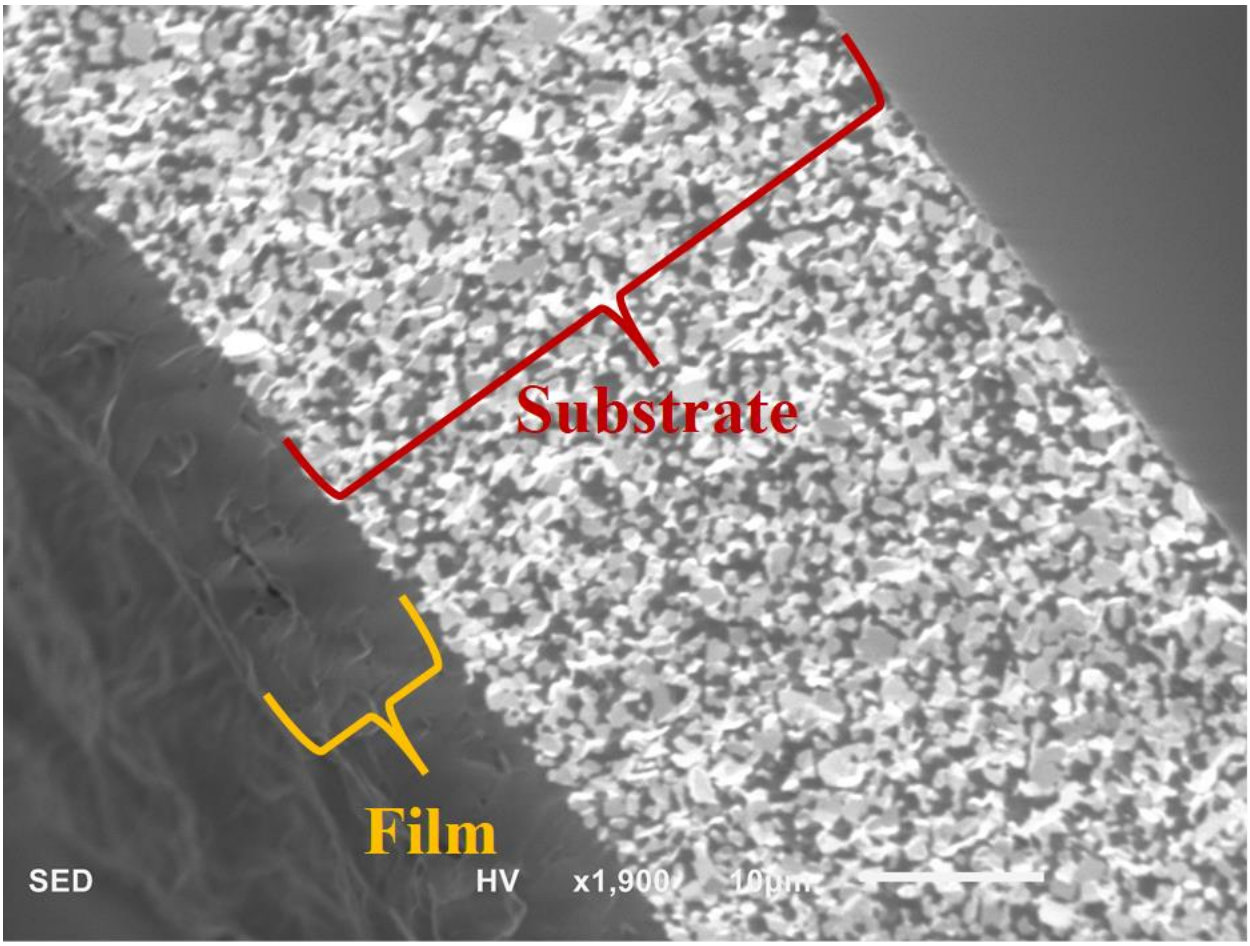

Figure 4.5: *SEM image of bilayer composite used to obtain substrate and film thickness.*

4.4 FEM Modeling of Self-Shaping Ceramics

While it is relatively simple to produce samples experimentally, understanding and predicting how the 2D shape of the ceramic substrate and the pattern of the film will interact is an incredibly complex challenge. One of the best tools to give insight into this relationship is FEM modeling. In this work 2D FEM models are used to directly predict curvature for any combination of substrate and film, replicating results from G. G. Stoney [40] and S. Timoshenko [39]. The 2D model is then expanded into three dimensions with a straight-forward 3D solid model. For more complex shapes and patterns, however, the composite shell model developed in the work by Huang et al. [174] was modified for the ceramic material system.

4.4.1 2D and 3D Solid FEM Modeling

The following section is adapted from *Utilizing Bilayer Shrinkage to Assemble Complex Ceramic Shapes* from Proceedings of the ASME 2022 International Mechanical Engineering Congress & Exposition (IMECE 2022) [171].

The 2D FEM model was executed in ABAQUS. The model was static and implicit and consisted of two steps. In the initial step, a constant 1350 ^{o}C temperature field was defined over the entire bimaterial composite. In the second step, this temperature was ramped down to 22 ^{o}C. For static steps like this, ABAQUS linearly interpolates between known material properties like those listed in Table 1 to provide continuous data. There is little information regarding extremely high temperature material properties of ceramics, so the model was limited to the maximum temperature properties listed in Table 1. Furthermore, because this model was static, time dependent processes like creep stress relaxation were not included. While these effects are expected to have significant impacts for long sintering procedures like those used with IC-tSOFCs, they are expected to have minor influences here, where the time spent at high temperatures is significantly less. Due to the large deformation expected, nonlinear geometry was also selected.

Following initial studies of curvature in bimaterial composites [39,40], the model was designed as a long rectangular 20 x 0.2 mm strip with varying ratio of substrate to film. This is shown in Figure 4.6. For cases where the substrate was significantly thicker than the film, a coarse mesh was used with edge seeds of 0.05 mm on the external surface of the substrate. At all four surfaces bounding the film, the edge seed was chosen to be 0.01 mm, yielding a fine mesh. For cases with a thick film (> 0.05 mm) the film boundary edge seeds were increased to 0.02 mm. The body was then meshed with unstructured triangular elements. The bottom left corner of the

composite was bound in the x and y directions. The left edge of the composite was bound in the x direction. This combination of boundary conditions allowed for displacement due to shrinkage of the thickness of the composite but kept this edge vertical. The right edge of the composite was unbound. Deformation could then be calculated using the displacement of the right mid-point.

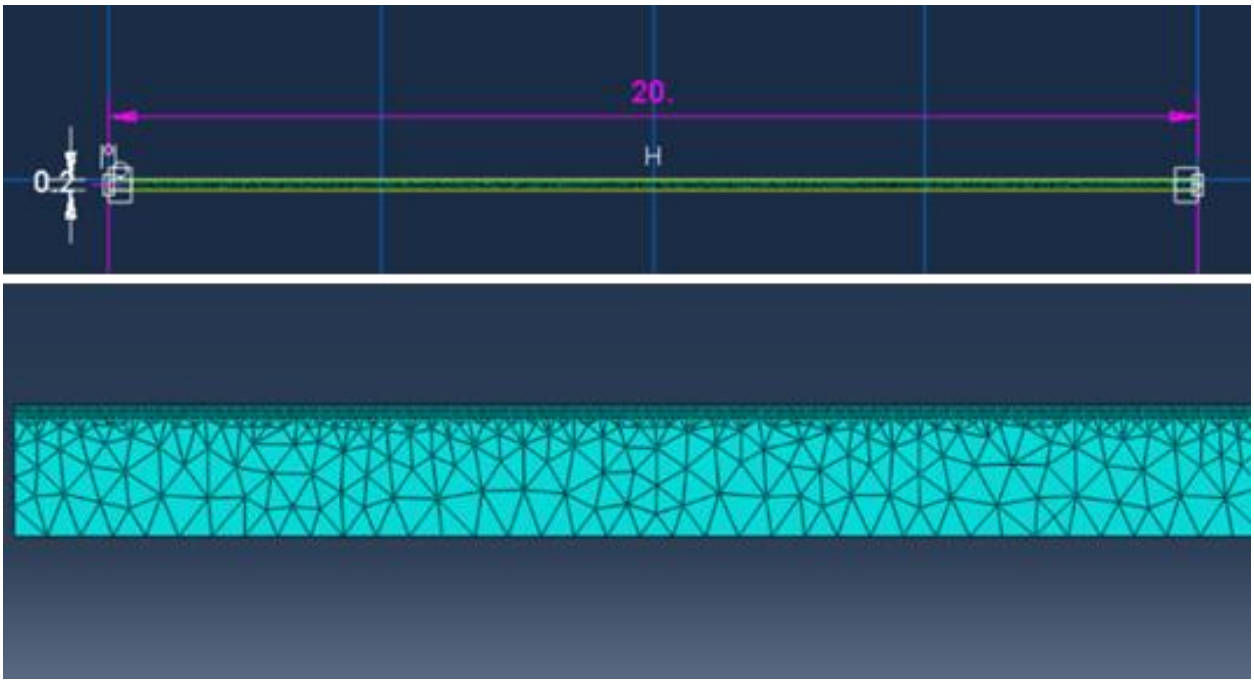

Figure 4.6 *Top: dimensions of two-dimensional finite element analysis bilayer test structure. Bottom: mesh of bilayer showing coarse mesh within substrate and fine mesh in film.*

For three-dimensional solid modeling, a square sheet with side length of 10 mm and thickness of 0.4 mm was produced with a film thickness of 0.02 mm. The mesh consisted of cubic elements with a side length of 0.02 mm. The bottom left corner of the composite was bound in the x, y and z directions, the right bottom corner was bound in the y and z directions, and the top left corner was bound in the z direction. This allowed the composite to deform out of the z-plane it was initiated in, but the corners remained in this plane. The same static implicit model for the 2D simulation was used here.

4.4.2 Composite Shell FEM Modeling

The following section is adapted from *Using Simulation and Experiment to Develop a Design Methodology for Self-Shaping Solid Oxide Fuel Cell Multilayer Ceramic Composites* published in Proceeding of the ASME 2023 POWER Conference (2023) [173].

Given how computationally intense the solid modeling described in section 4.4.1 becomes for increasingly complex models, a simpler approach was needed. As part of the work from Huang et al. [174], a 3D shell composite model was developed to model MEMS microelectrode arrays. While this work used polymers and metals, the expectation was this model could be easily modified using the material properties and process described in Table 1 and section 4.4.1 to predict the behaviors of the ceramic material system. The model used here consisted of a set of canonical 2D shapes including squares, rectangles, and disks. These shapes were meshed with 0.2 mm seeds and quadrilateral elements as shown in the top of Figure 4.7. For quantitative curvature measurements, rectangles with dimensions of 25 x 10 mm and 10 x 5 mm were used. For homogeneous bilayer shrinkage models, a section was defined with NiO-YSZ substrate of thickness varying from 0.100 to 0.150 mm. The YSZ film thickness was varied from 0.005 to 0.050 mm. Three integration points were used for both layers. For non-homogeneous models, regions were chosen with either film on top or bottom surface of substrate and regions with only substrate. Thicknesses were chosen to replicate a constant substrate thickness with additional film added in regions that received coating.

Boundary conditions for rectangular models was the same as in section 4.4.1 where three corners of the rectangle were constrained to ensure they remain within a constant z-plane but

enable deformation and shrinkage. These boundary conditions are depicted in the bottom of Figure 4.7.

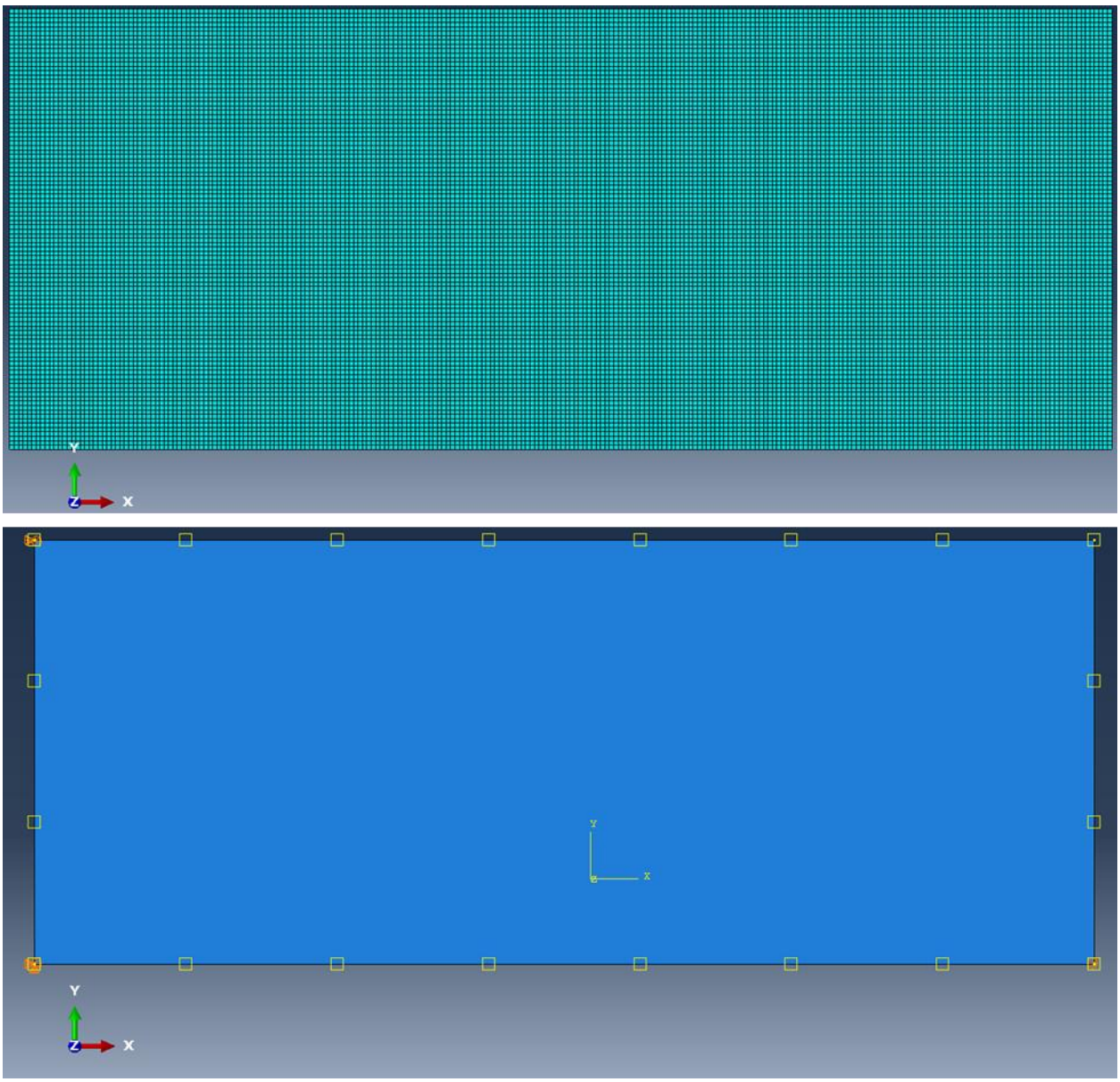

Figure 4.7 *top: Image showing rectangular mesh for 25 x 10 mm rectangle ABAQUS model. Bottom: Image showing boundary conditions for rectangular samples.*

Boundary conditions for disks were similar to those used with rectangles where three edges of the disk were constrained to a constant z-plane, but shrinkage within that plane was allowed.

For both rectangles and disks, these boundary conditions were chosen to allow for free deformation of the structure.

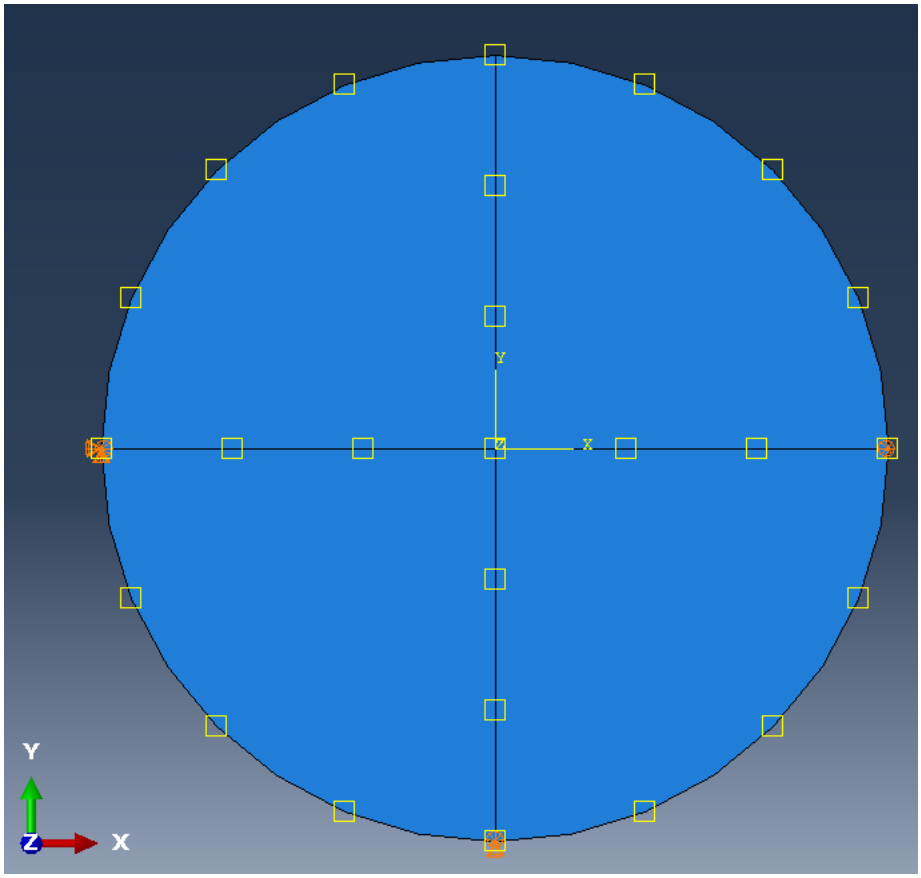

Figure 4.8: *Image showing boundary conditions for disk ABAQUS models.*

4.5 Understanding the Behavior of Ceramic Composites Experiencing Bilayer Shrinkage

Studies regarding bilayer shrinkage primarily analyze curvature and shape as discussed in section 2.3. Following will be analysis of the ceramic material system experiencing bilayer shrinkage where predictions of curvature and shape will be obtained from analytical modeling, FEM modeling, and experiment.

4.5.1 Prediction of Curvature with Stoney Model

This section is adapted from *Utilizing Bilayer Shrinkage to Assemble Complex Ceramic Shapes* from Proceedings of the ASME 2022 International Mechanical Engineering Congress and Exposition (IMECE 2022) [171].

As described in section 2.3.1 G. G. Stoney's model (equation 2.1 and repeated here for reference) may be used to analyze bimaterial composites experiencing bilayer shrinkage:

$$\sigma_1 = \frac{E_2 t_2^2}{6(1-\nu_2)t_1}\kappa_0 \qquad (2.1)$$

When the assumption is made that the tension within the film remains constant, a simplified relationship in terms of a parameter τ which compares the square of the substrate thickness to the film thickness may be given as in equation 2.2:

$$\frac{1}{\kappa_0} = r \propto \frac{t_2^2}{t_1} \equiv \tau \qquad (2.2)$$

The curvature for various combinations of substrate and film thickness was produced using the 2D solid FEM model described in section 4.4.1. These curvatures were then plotted against τ as shown in Figure 4.9. All combinations of substrate and film thickness conformed well to a linear fit as predicted by Stoney, but with a non-zero intercept. A theoretical model is added to this graph with a y-intercept of zero. This would be the trend expected by the Stoney model where a zero-value of τ (a film which is infinitely thicker than the substrate) would cause an infinitely curved composite. The presence of this non-zero intercept in the linear fit is an expected result. As described in section 2.3.1, the Stoney model is only accurate for film thicknesses up to ~ 10% the substrate thickness. Above this limit, we experience deviations from the theoretical model. Regardless, the linear fit

can allow us to predict the curvature for any τ assuming all other material properties remain the same. This is given by equation 4.1:

$$\frac{1}{\kappa_0}(mm) = (37.5 \pm 0.114) * (\tau)(mm) + (44.5 \pm 0.903)(mm) \quad (4.1)$$

Where p-values of 3.19e-11 and 8.28e-18 were obtained for the intercept and slope respectively indicating a very high accuracy of this fit.

This intercept corresponds to composites where the electrolyte film has a thickness greater than the substrate and at $\tau = 0$ the entire composite is the film. The original Stoney model indicates at this limit, $\kappa_0^{-1} = r = 0$. This would result in a composite rolled into an infinitely curved tube. Instead, this scenario would apparently have a radius of curvature of 44.5 mm. This makes sense given the non-zero cost to bending of the film itself. This also indicates that all samples with electrolyte film thickness >~25% the anode thickness, the degree of curvature remains constant. More generally, for a ceramic composite, there is a limit to the degree of warpage that can be achieved only by varying film thickness.

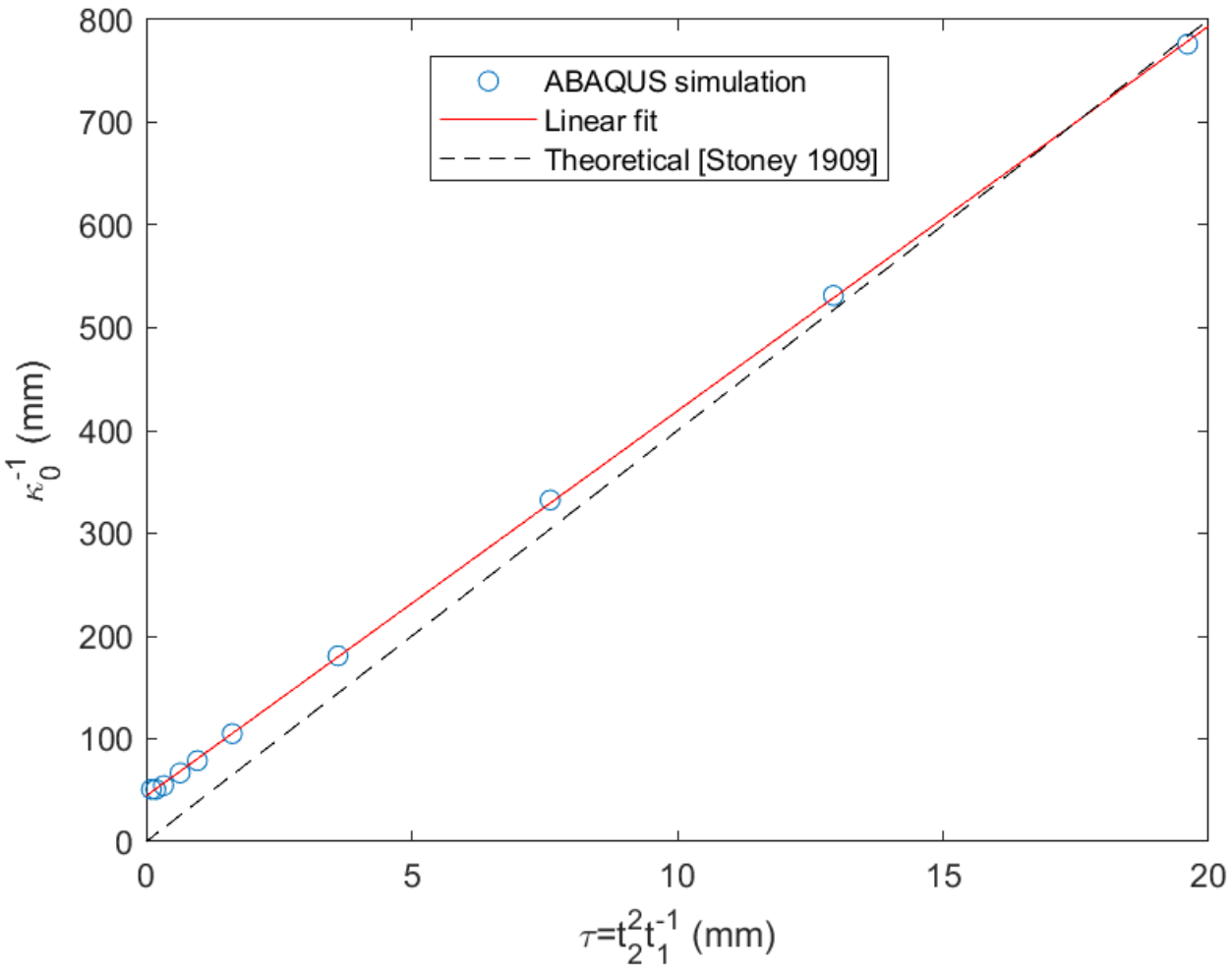

Figure 4.9: *Plot showing curvature obtained in 2D solid FEM models versus parameter* $\boldsymbol{\tau}$ *obtained from Stoney's prediction for curvature of bimaterial composites. Adapted from* [171].

4.5.2 Prediction of Curvature Using Timoshenko Model

The following section is adapted from *Using Simulation and Experiment to Develop a Design Methodology for Self-Shaping Solid Oxide Fuel Cell Multilayer Ceramic Composites* published in Proceeding of the ASME 2023 POWER Conference (2023) [173].

As described in section 2.3.1, while Stoney's model is applicable to a wider variety of situations where bilayer shrinkage occurs, Timoshenko's model is specifically suited to bilayer shrinkage caused by mismatched TEC [39]. The relationship is repeated from section 2.3.1 here:

$$\kappa_0 = \frac{6(\alpha_2-\alpha_1)(T-T_0)\left(1+\frac{t_1}{t_2}\right)^2}{(t_1+t_2)\left(3\left(1+\frac{t_1}{t_2}\right)^2+\left(1+\frac{t_1E_1}{t_2E_2}+\frac{1}{\frac{t_1E_1}{t_2E_2}}\right)\right)} \quad (2.3)$$

This analytical model was compared against the results from 2D FEM and 3D FEM for a variety of substrate and film thicknesses. This can be seen in Figure 4.10. All models agree well with each other for film thickness > ~10 μm. Possible sources of discrepancies between models could be the need to use average material properties with the Timoshenko model.

Interestingly, it can be seen that for 3D FEM models, the 10 x 5 mm rectangle had a higher curvature than the 25 x 10 mm rectangle. Following Alben et al. [42], small regions of nonzero Gaussian curvature occur at the edges of bimaterial composites experiencing bilayer shrinkage. For larger sheets these regions will be larger and cause a greater increase in the second moment of area perpendicular to the primary axis of curvature introducing a stiffening effect.

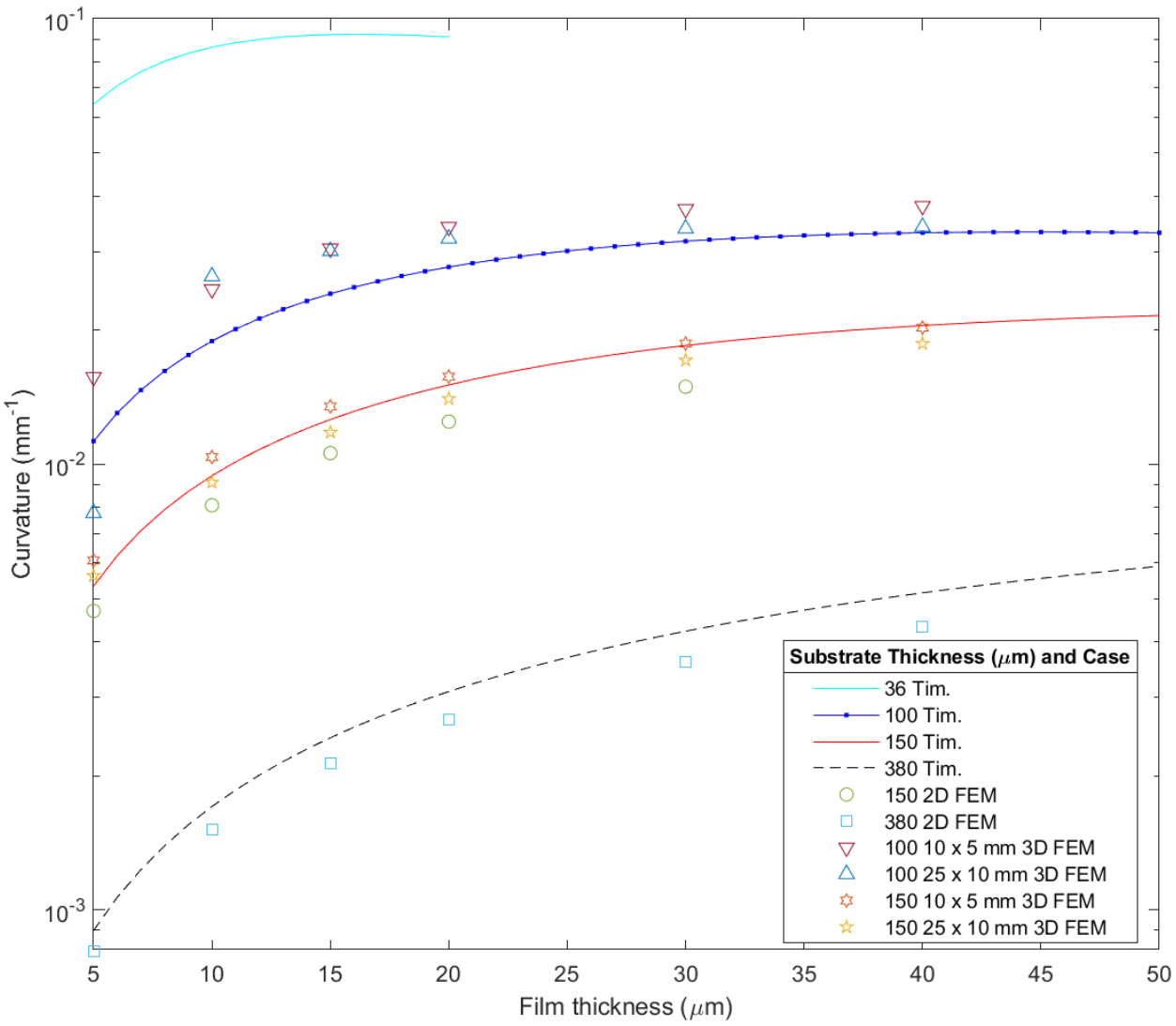

Figure 4.10: *Plot showing curvature for Timoshenko analytical model, 2D FEM model, and 3D FEM model for varying film thickness.*

4.5.3 Comparison Between Experiment and Prediction for Curvature

Though good agreement is achieved between analytical models, 2D FEM models, and 3D FEM models. There is a large disagreement between these predictions of curvature and the actual curvature achieved in experiment. Real samples curve more by an order of magnitude. This discrepancy is shown in Figure 4.11. As described in section 4.4, there is limited information regarding the material properties of the ceramic materials used here at the temperature they

experience during sintering. Also, time dependent processes like creep stress relaxation are not included in this model. Furthermore, in analytical modeling, as described in sections 4.5.1 4.5.2 various simplifying assumptions are made. In relation to the Timoshenko model, all material properties are assumed constant. Further work is needed to assess the validity of these assumptions. There is also the possibility that linear shrinkage plays a role here. By vastly differentiating ceramic loading through a material, curvature may be introduced as used by Dine et al. [36]. Currently, it is thought that the zero-stress, flat state of the sheet is experienced at the peak sintering temperature. Before this point, the composite is not a solid object, rather a collection of loosely bound particles as described in section 2.2.7. If this is not true, then linear shrinkage may have an effect. This explanation, however, would have the opposite effect, causing a decrease in curvature from that predicted by modeling techniques. This is because the linear shrinkage of porous NiO-YSZ is greater than fully dense YSZ [154]. This conflict necessitates further study.

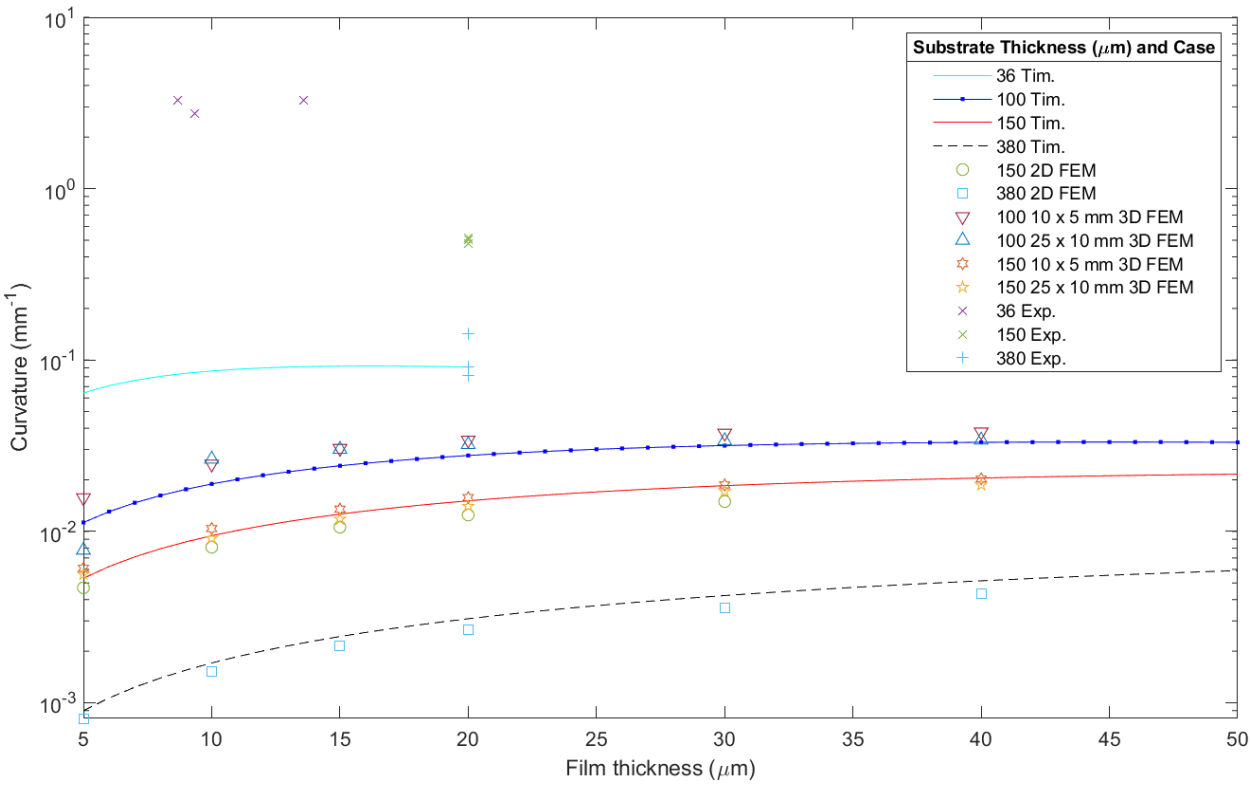

Figure 4.11: *Compilation of all experimental curvatures, analytical models, 2D FEM models, and 3D FEM models. Adapted from* [173].

In ceramics manufacturing analytical predictions for processes rarely align with reality as described in sections 2.2.1 and 2.2.5. Instead, it is often easiest and most effective to develop an empirical prediction for a process as was done with fill coating in relation to IC-tSOFCs. Here, an experimental TEC may be used to match the curvature obtained in experiment to predictions from modeling. This is shown in Figure 4.12. Following literature, the average TEC for NiO-YSZ and YSZ from 1350 °C to 22 °C are $7.3 \cdot 10^{-6}$ K^{-1} [175] and $1.00 \cdot 10^{-5}$ K^{-1} [103] respectively. If the YSZ TEC is increased to $9.6 \cdot 10^{-5}$ K^{-1}, the new experimental TEC (TEC_{exp}), promising agreement is obtained between experiment and analytical modeling.

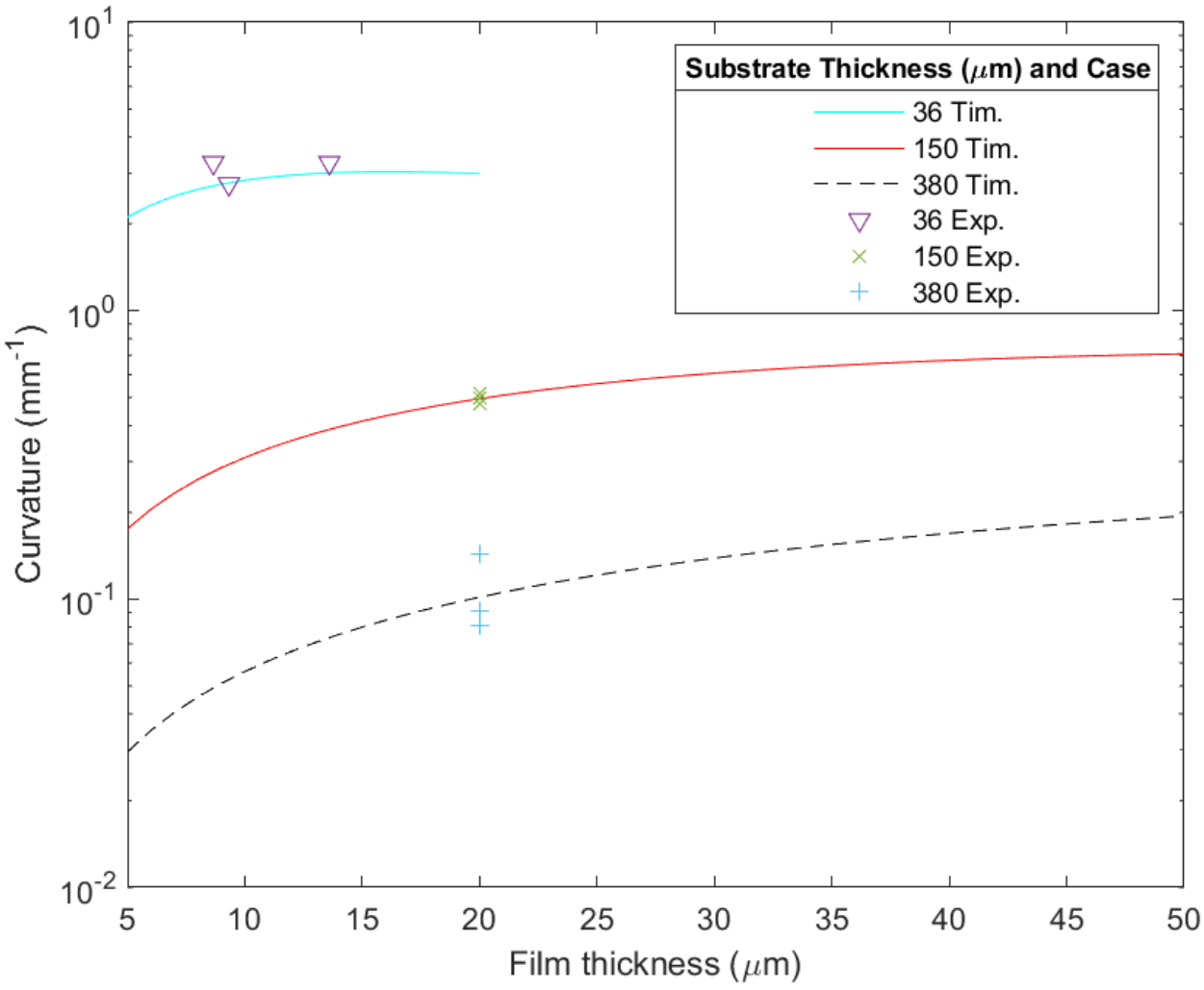

Figure 4.12: *Plot showing analytical models with TEC_{exp} determined from experiment and curvature from experimental samples. Adapted from* [173].

4.5.4 Predicting Mode of Deformation

This section is adapted from *Utilizing Bilayer Shrinkage to Assemble Complex Ceramic Shapes* from Proceedings of the ASME 2022 International Mechanical Engineering Congress and Exposition (IMECE 2022) [171].

As described by Pezzulla et al. [41] and as summarized in section 2.3.1, two primary modes of deformation may occur for a bimaterial composite experiencing bilayer shrinkage. The first is a cap-like mode where the composite develops a nonzero Gaussian curvature. The composite must

stretch to achieve this shape and so it is only expected with "thick" sheets, where thick can be determined by a comparison between the natural and characteristic curvatures κ_0 and $\kappa_c = \frac{h}{L^2}$, where h is the overall thickness of the composite, and L is a characteristic length. As a sheet deforms, it first stretches into the cap-like mode, then as the deformation continues and the natural curvature increases, it reaches a critical value κ_c where it bifurcates into the bending mode. This comes from a comparison of the stretching and bending energies of the sheet, equations 2.5 and 2.6, and ultimately yields a scaling law which may generally predict behaviors. When the characteristic curvature of the final deformed sheet is greater than the natural curvature i.e., when a sheet is "thick," it will stretch into a cap, and when the characteristic curvature is much lower than the natural curvature i.e., when a sheet is "thin," it will bend. This has generally been supported with experimental work and FEM modeling.

As can be seen in Figure 4.13, both a solid 3D FEM square and a dry pressed SOFC stretched into cap-like shapes. For the dry pressed cell, the composite thickness was measured to be 450 μm with a radius of 6.5 mm. This yields a characteristic curvature of 0.0107 mm^{-1}. The natural curvature was obtained by measuring the chord length and arc length to obtain a radius of curvature of 143 mm corresponding to a curvature of 0.0070 mm^{-1}. Here, the natural curvature remains below the characteristic curvature. As such, the bimaterial composite does not curve to the extent it would bifurcate into the bending mode. When the 3D solid FEM model from section 4.4.1 is used to analyze the deformation of a square bimaterial composite cap-like deformation is seen. The characteristic curvature for this shape is 0.004 mm^{-1} and the natural curvature is 0.0024 mm^{-1} as predicted by the Timoshenko model. Again, the natural curvature does not exceed the characteristic curvature and so bifurcation does not occur.

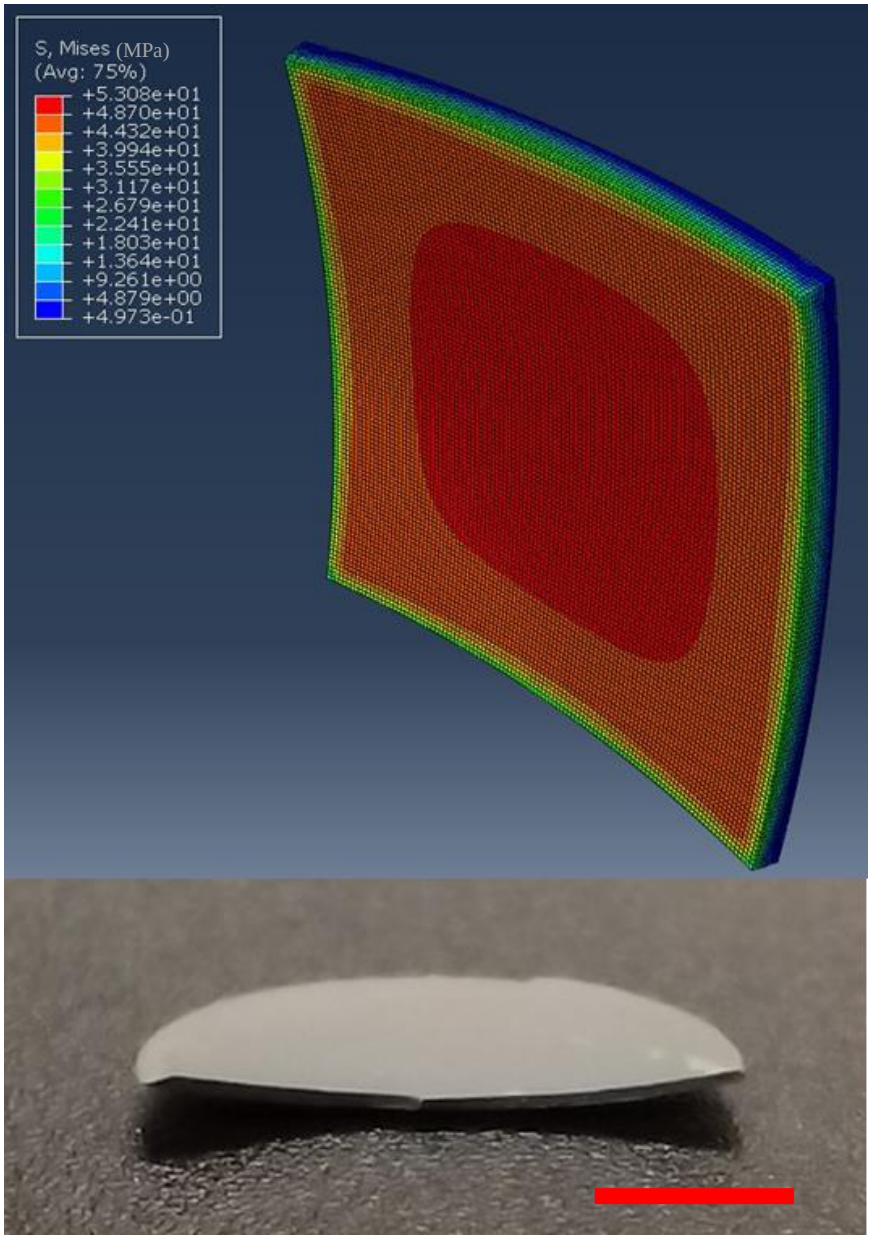

Figure 4.13 *Top: Solid 3D FEM model showing bimaterial composite deforming into cap-like shape. Bottom: Dry pressed SOFC deformed into cap-like shape after sintering. Scale bar is 5 mm. Adapted from* [171].

Given the ease with which large thin sheets may be made with tape casting, cap-like deformation is rare. Most sheets experimentally produced have natural curvatures significantly higher than the characteristic curvature. Two examples of this are shown in Figure 4.14. The top shows the composite shell FEM for a rectangle of dimensions 25 x 10 mm, substrate thickness of

150 μm, and film thickness of 20 μm. Here the TEC_{exp} described in section 4.5.3 is used. The bottom shows an experimentally obtained sample of the same dimensions. Natural curvatures for both may be predicted to be 0.51 mm^{-1} while characteristic curvatures are 0.00060 mm^{-1}. The Natural curvature is many orders of magnitude larger than the characteristic curvature, so bifurcation into the tube-like bending mode occurs almost instantaneously for both samples. In relation to prediction of deformation mode, agreement is achieved between analytical predictions, FEM modeling, and experiment.

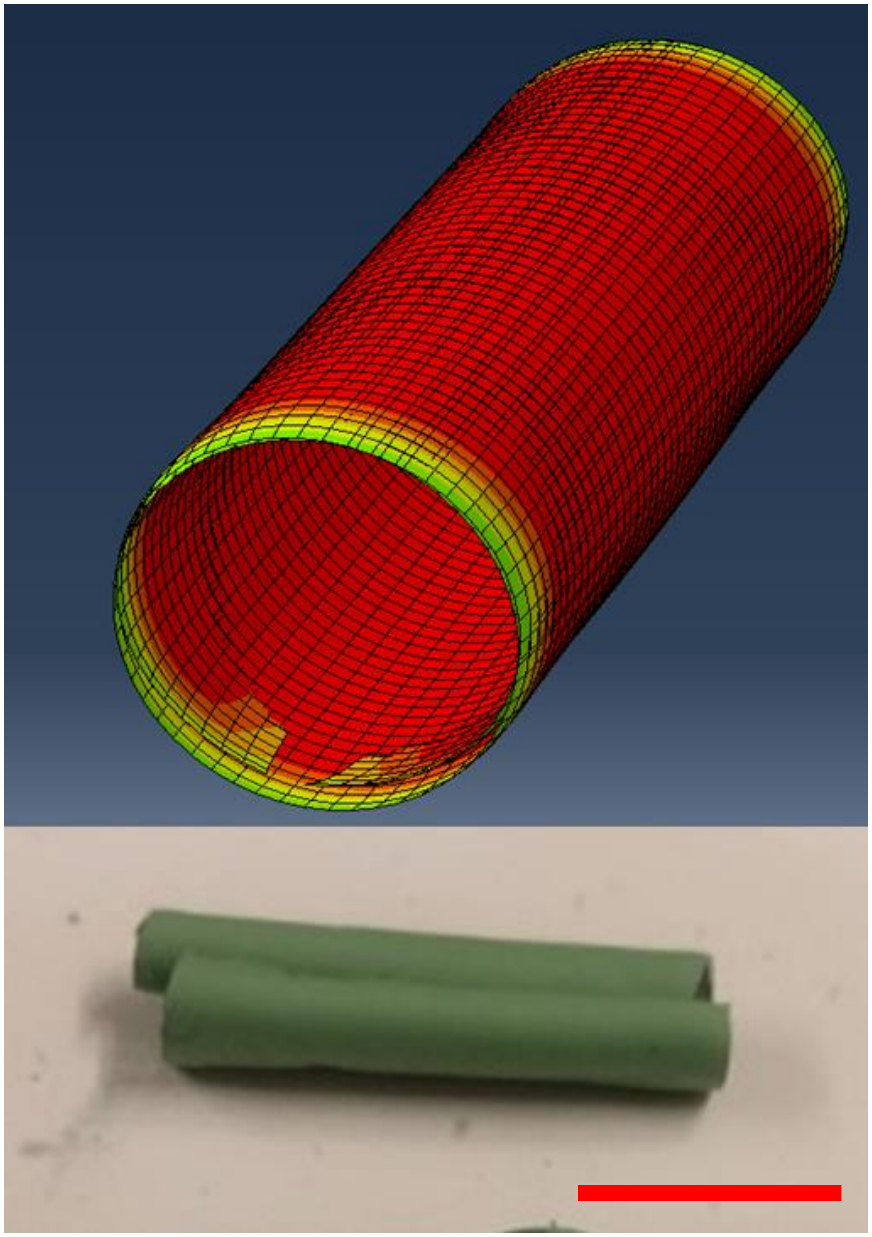

Figure 4.14 *Top: 3D composite shell FEM model of 25 x 10 mm rectangle. Bottom: Image of experimentally obtained 25 x 10 mm rectangle sample replicating FEM model. Scale bar is 5 mm.*

4.5.5 Predicting Deformation Direction

The following section is adapted from *Using Simulation and Experiment to Develop a Design Methodology for Self-Shaping Solid Oxide Fuel Cell Multilayer Ceramic Composites* published in Proceeding of the ASME 2023 POWER Conference (2023) [173].

For bimaterial composites deforming by bending into tube-like shapes, one principal axis curves while the perpendicular axis remains straight. The orientation of the axes with respect to the two-dimensional shape of the sheet has been studied by Pezzulla et al. [41], while Alben et al. [42] introduce reasoning for why certain bending directions are preferred as well as possible causes for misorientation of bending direction from theoretical predictions.

Beginning with the study of rectangular sheets, orientation of bending was shown to be a result of edge effects [42]. While the majority of the rectangular sheet bends, small regions at the boundaries and corners experience a small amount of stretching. These regions lower the local energy density, so to minimize the overall energy within the fully deformed sheet, these regions must be as large as possible. By bending the length of the sheet, these high energy regions may be maximized. For rectangles this means bending occurs such that a short thick tube is formed. Pezzulla then generalized this behavior to various symmetric canonical shapes including disks, triangles, pentagons, and hexagons [41]. For all these shapes, the longest length of the object bends. For shapes where there are multiple longest lengths, no preference occurs between these axes. For circles, this results in no preferred bending direction, and for squares either diagonal may bend while the other remains straight. These results have been replicated in experiment as shown in Figure 4.15. For rectangles, squares, and circles, the behaviors predicted by analytical understanding and FEM modeling coincide with deformation experienced by ceramic materials.

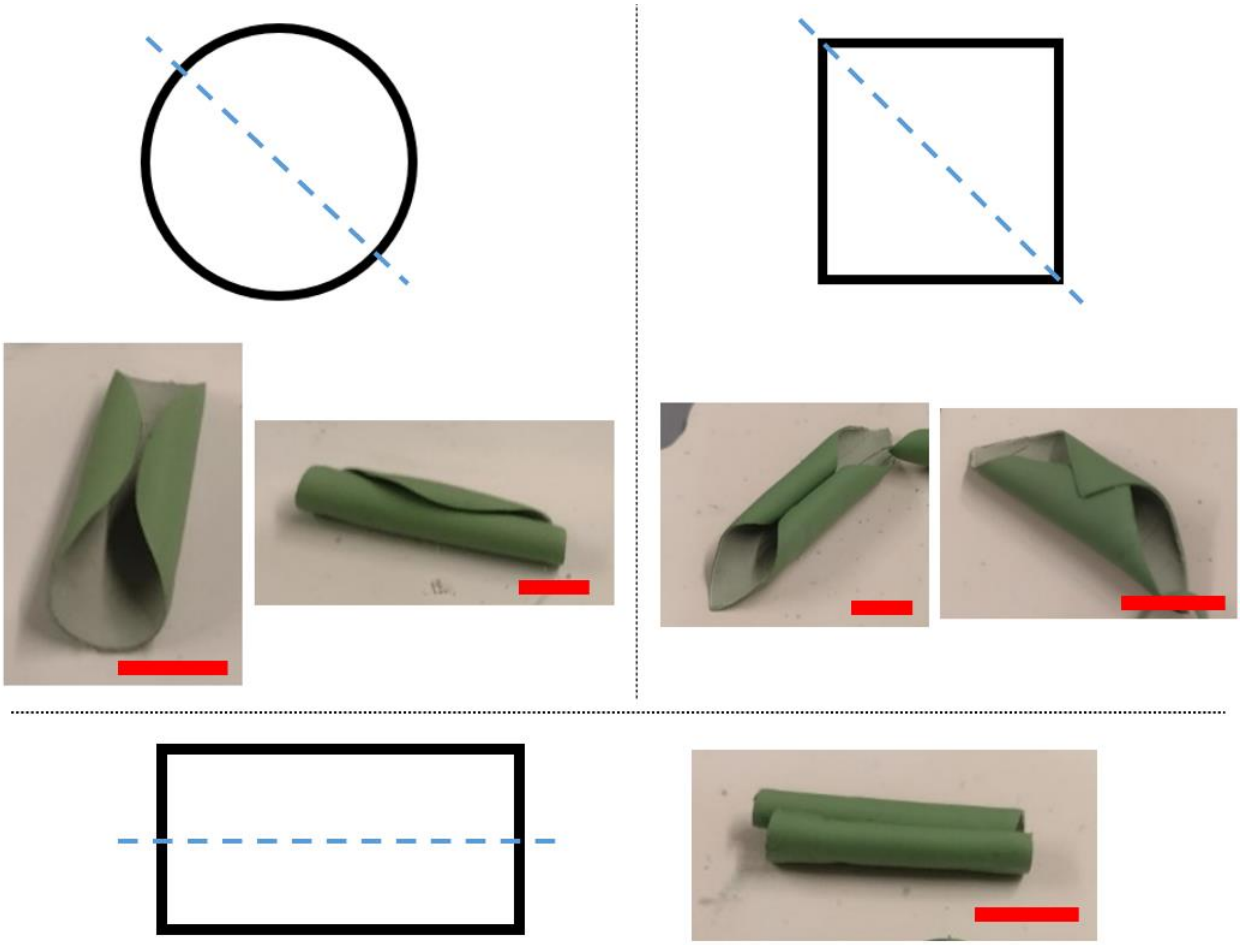

Figure 4.15: *Diagrams of analytical predictions for bending direction which show 2D shape with blue dashed line indicating principal axis which will bend. Inset images show experimentally produced samples with bending direction consistent with theoretical predictions. Disks are 5 mm radius and 10 mm radius (left), squares have side lengths of 20 mm and 10 mm (right), and rectangle have dimensions 10 mm x 20 mm (bottom). Substrate thickness is 150 µm and film thickness is 20 µm. Scale bar is 5 mm. Adapted from* [173].

As discussed in section 2.3.2, ceramics are far from an idealized or homogenous system. Alben et al. warn that the differences in energy between sheets bent in different directions is small, introducing a large potential to experience unexpected deformation modes. As can be seen in Figure 4.16 A, C, D, and E, misorientation of the bending direction occurs producing thin tubes and spirals. Unresolved deformation also occurs as shown in Figure 4.16 B. The presence of defects whether they may be irregularly sized air bubbles within the substrate, nonuniform film thickness, or imperfections in the 2D shape of the sheet may all contribute to these behaviors. As

also discussed in 2.3.2, these theoretical models do not account for body forces like gravity which become increasingly present with larger and heavier sheets. The 90^{o} misorientation angle shown in Figure 4.16 A and C is particularly common with rectangles of high aspect ratio. It is possible with these samples that instead of minimizing the energy associated with stretching at the sheet boundaries, gravitational potential energy may be minimized.

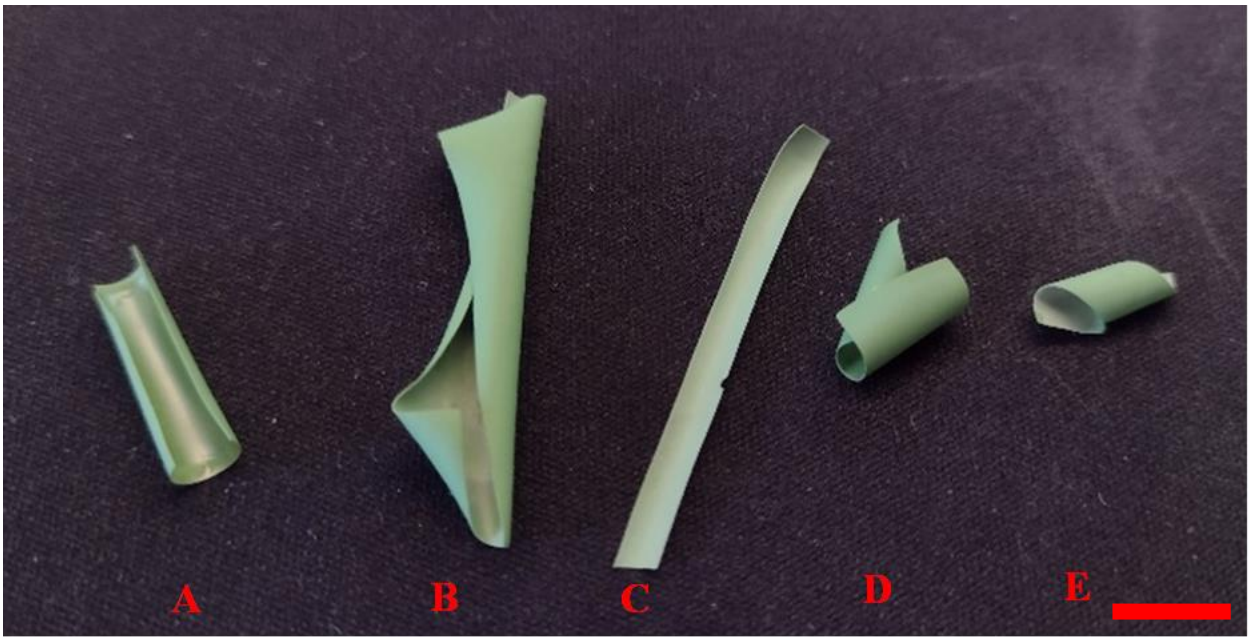

Figure 4.16: *SOFC MCCs showing unexpected behaviors. 90^{o} misoriented deformation direction (A, C). Varying local deformation (B, C, D). ~45^{o} misoriented deformation direction (E). Scale bar is 5 mm. Adapted from* [171].

The composite shell model described in 4.4.2 successfully predicts the bending direction for rectangles and complex shapes such as the wave cell successfully. As was shown in Figure 4.14, the rectangle has deformed by bending the longest length of the sheet. This was true for rectangles of aspect ratios from 25 to 1.064. Below this limit, a different mode of deformation was experienced. Pezzulla would predict one of the diagonals to bend while the other would remain straight, but this was not the case with this FEM model. Instead, all four corners bent as shown in Figure 4.17.

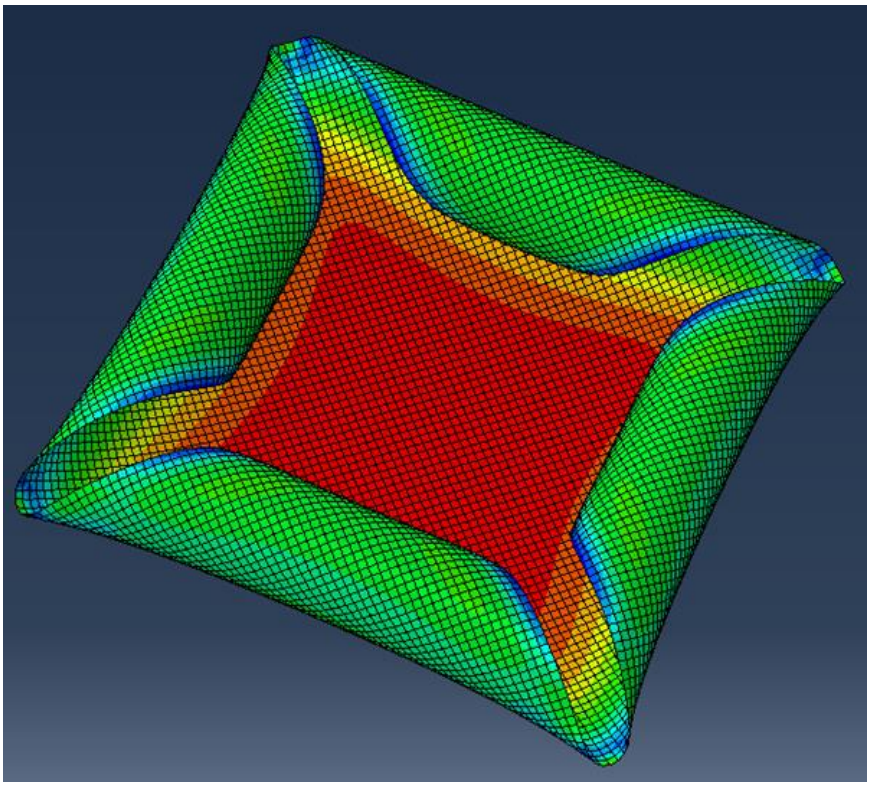

Figure 4.17: *Deformed square composite shell FEM model. Adapted from* [173].

As described in section 4.5.4, when deforming, the sheet must first stretch then bifurcate into the bending mode. Stretching is an axisymmetric mode while bending requires a buckle where the curvature in one principal direction reduces to zero. As can be seen in Figure 4.18, at approximately this point of bifurcation the rectangle with aspect ratio of 1.064 shows a mirror symmetry of its Von Mises stress. The bottom image shows a rectangle with aspect ratio of 1.042 two mirrored symmetries of its Von Mises stress. ABAQUS predicts this transition in aspect ratio to introduce the change in deformation direction between rectangles and squares, but does not accurately predict the deformation mode for squares. Pezzulla predicted the aspect ratio this transition would occur at to be 1.028 ± 0.0025 [41]. Disagreement between this prediction and what is observed here is only ~3 %.

25x23.5

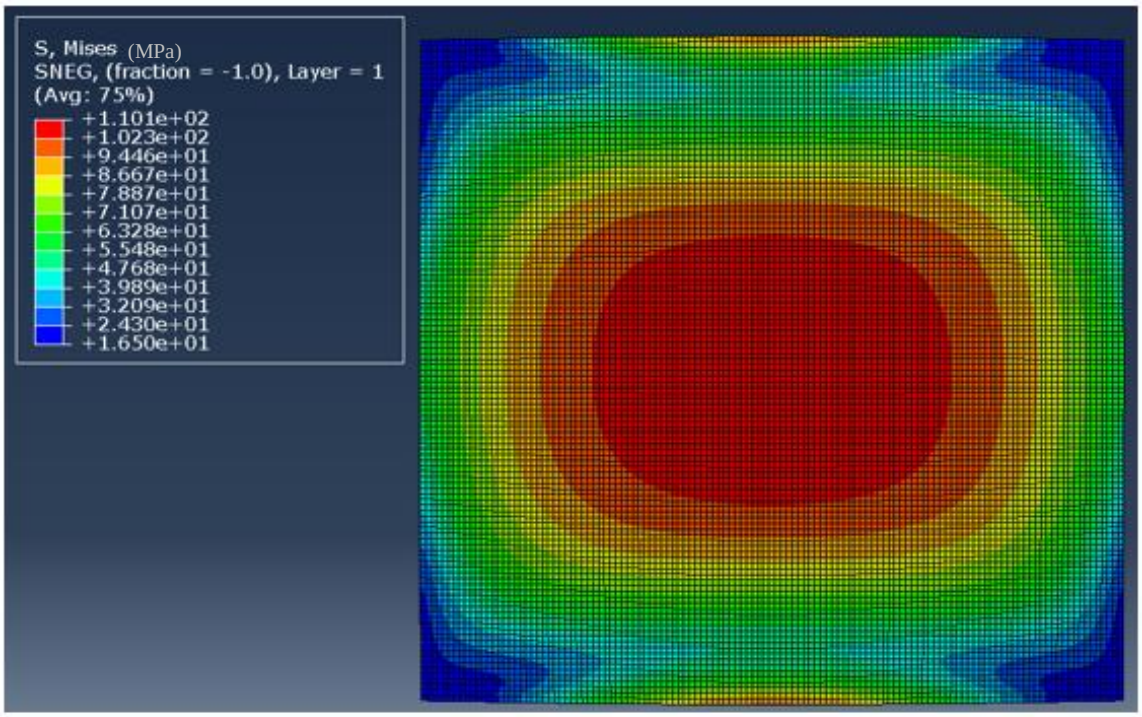

25x24

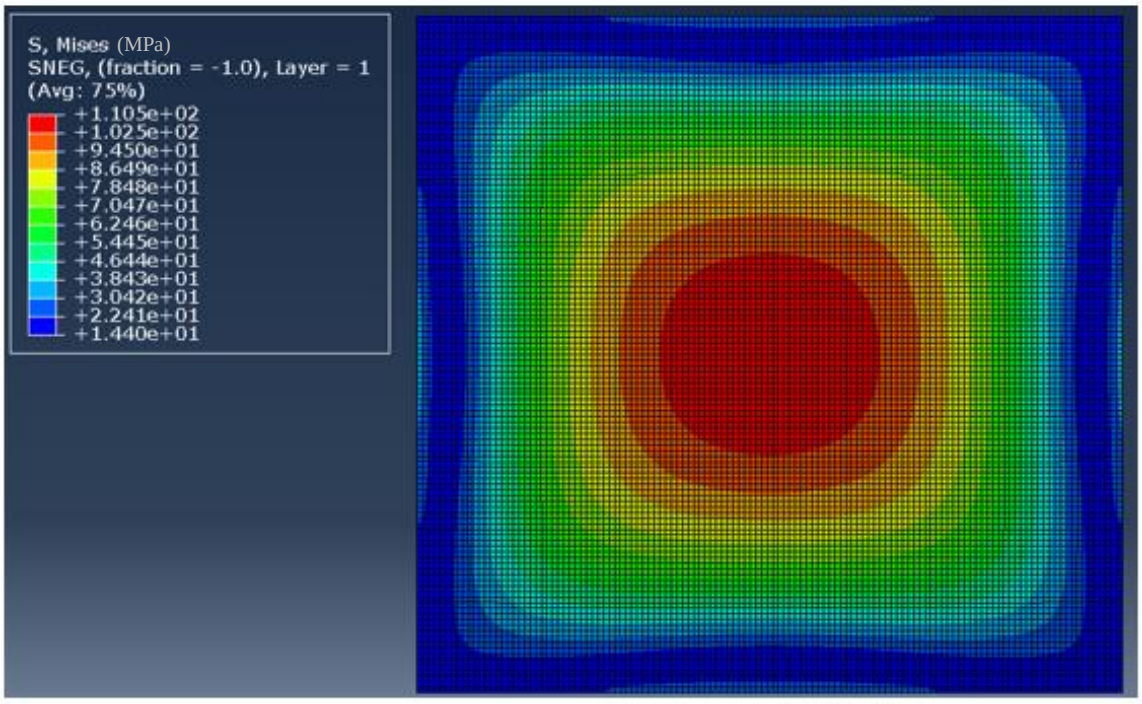

Figure 4.18 *Top: Rectangle with aspect ratio of 1.064. Bottom: Rectangle with aspect ratio of 1.042. Both are colored by Von Mises stress at point of bifurcation.*

This issue with squares is also seen with circles as shown in Figure 4.19. For these highly symmetric shapes where multiple longest lengths of the sheet exist, the current 3D composite shell FEM model is unable to successfully buckle the structure in such a way that the lowest energy deformation shape is experienced. While this is problematic for these structures, more complex patterns contain few lines of symmetry enabling accurate predictions of shape. This is shown in Figure 4.20 for the wave cell. This enables the prediction of increasingly complex 3D geometries as will be discussed briefly in chapter 5.

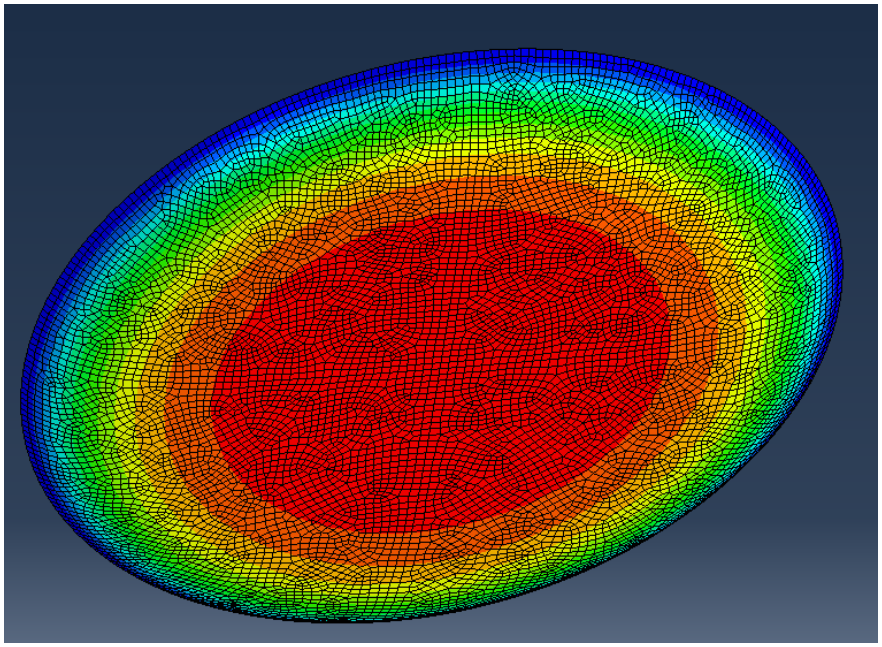

Figure 4.19: *Deformed circular composite shell FEM model. Adapted from* [173].

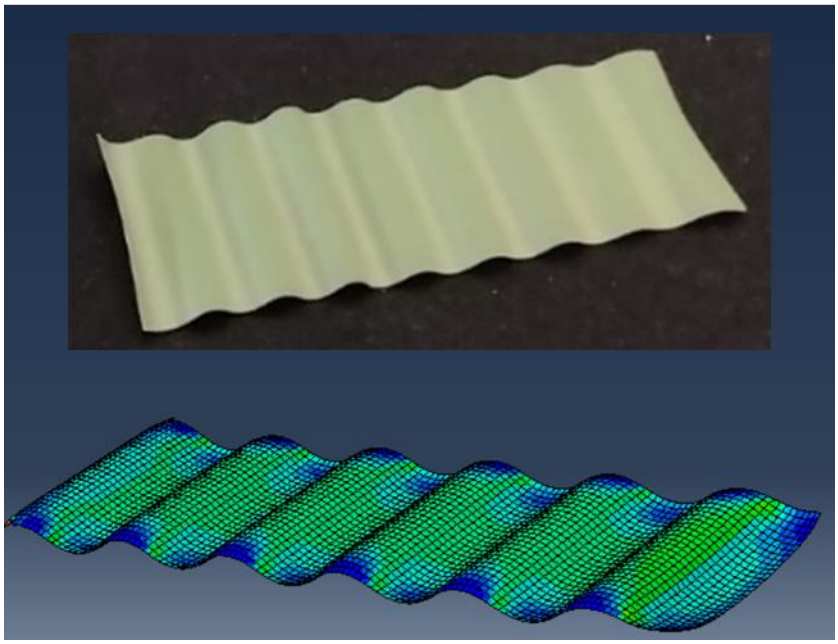

Figure 4.20: *Deformed wave composite shell FEM model. Inset image shows comparable experimental sample. Adapted from* [173].

5. Conclusions and Future Work

5.1 Conclusions

Methods to control MCC layer architecture, as well as the overall 3D geometry have been shown. By introducing novel manufacturing techniques, ceramics can be better tailored for use in a wide variety of applications, offering significant benefits over the materials that are currently used. The first component of this thesis dealt with cell layer architecture. The introduction of fill coating enabled the creation of tSOFCs with internal active layers. Specifically, the IC-tSOFC was developed, which is well-suited for use in fuel rich environments such as those seen with combustion chambers. The efficacy of this deposition method was evaluated through mechanical analysis and electrochemical performance analysis of fully formed cells. Compared to traditional EC-tSOFCs produced using dip coating, the novel cell and deposition technique were shown to have comparably uniform electrolyte and cathode layers. The power production of IC-tSOFCs was shown to be 23 % lower than EC-tSOFCs, but more recent work has shown continual increases in the power production capabilities of IC-tSOFCs. The IC-tSOFC also successfully served as a testbed to analyze the effects of complex fuel compositions on SOFC performance. Impacts of fuel streams containing high concentrations of carbon monoxide and methane were studied, revealing performance decreases compared to pure and dilute hydrogen fuel streams. These effects, however, were expected and performance remained at levels indicating promising results in future work analyzing SOFC performance in prototype SOFC-CHP systems.

Though the development of the IC-tSOFC was successful, issues with cracking during sintering prompted a more comprehensive analysis of the residual stresses within MCCs as well as potential solutions. It was discovered that the IC-tSOFC geometry introduced tensile stresses to

the anode support due to mismatched TECs of the anode and electrolyte. This issue was remedied with the introduction of extended sintering procedures, which enabled plastic deformation processes such as creep stress relaxation to introduce small amounts of strain to the IC-tSOFC, reducing residual stresses below critical values, and significantly increasing the survival rate of IC-tSOFCs.

Though initial work dealt with reducing residual stresses within MCCs, tremendous potential was seen to utilize these stresses to alter the 3D geometry of MCCs. The second part of this thesis dealt with this idea. Tape cast ceramic sheets consisting of NiO-YSZ were coated with a thin YSZ film. With the application of a mask during spraying, the deposited film pattern could be controlled. Figure 5.1 shows some of the samples prepared using this technique. To produce a robust design methodology using this technique, thorough understanding of bilayer shrinkage driven self-shaping is necessary. To do this, previous work analyzing soft materials was adapted for the ceramic system. Focus was placed on curvature prediction and shape prediction. Early studies which derived final curvature from basic mechanics were applied to this system [39,40]. Though these predictions were consistent with FEM modeling, experimentally obtained curvatures were greater by an order of magnitude. Though the cause for this discrepancy is a topic of future investigation, an experimental TEC was introduced which fit the curvature predicted from the Timoshenko model to experimental data. This TEC_{exp} can then be used to predict the shape obtained in real-world MCCs.

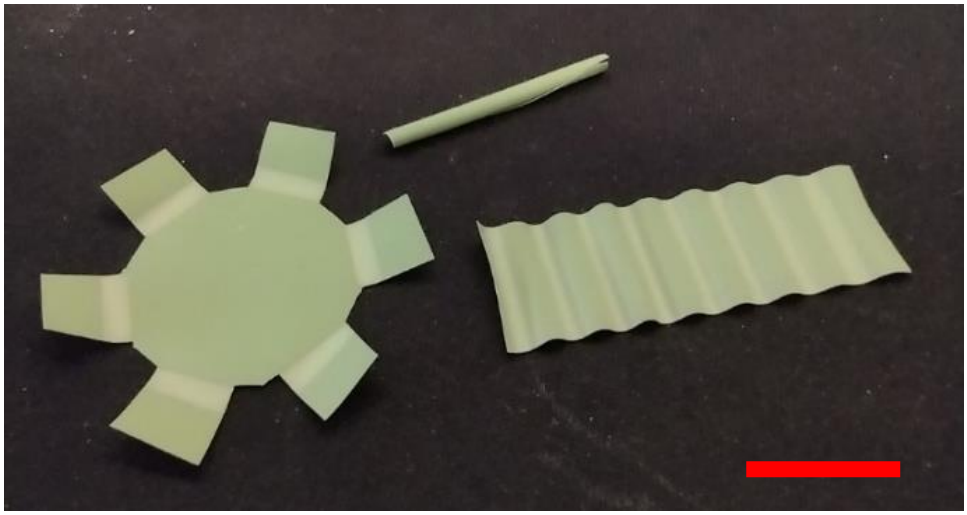

Figure 5.1: *MCCs formed using bilayer shrinkage driven self-shaping. Scale bar is 10 mm.*

Shape prediction was also adapted from the soft matter world to the ceramic system following previous work from Pezzulla et al. [41] and Alben et al. [42]. Bifurcation between cap-like and tube-like deformation modes was successfully predicted with comparison of the natural curvature and characteristic curvatures for both FEM and real-world experiments. Bending direction in the case of tube-deformation was generally shown to be consistent with analytical predictions where the longest length of the sheet is expected to bend. However, in the case of high aspect ratio rectangles, a 90^{o} misorientation was observed as shown in Figure 5.1, potentially due to gravitational effects which have previously been ignored. FEM modeling for low symmetry shapes was shown to be consistent with analytical predictions, however for highly symmetric shapes such as circles and squares, multiple lines of symmetry bent. For increasingly complex objects with low symmetry, FEM has proven successful at predicting final shape. Though there is tremendous work to be done investigating fundamental principles controlling this self-shaping process, there is equally tremendous potential to begin producing highly complex structures like those shown in Figure 5.1.

5.2 Future work

As described in section 5.1, IC-tSOFC performance has continued to increase since its initial development. Possible improvements can be achieved through the use of multilayered electrolytes and cathodes [51], but the majority of work is expected to focus on integrating IC-tSOFCs into combustion systems. With the aggressive shift away from fossil fuel powered HVAC systems, however, alternative applications are expected. The most promising of these applications is utilizing an otherwise harmful and unavoidable product of human existence, biogas [11–14,176–179].

Unlike the development of IC-tSOFCs, work investigating self-shaping ceramics has introduced a myriad of questions worthy of exploration. Experimental composites experience much higher curvatures than predicted by FEM or analytical modeling. This motivates the production of many experimental samples, probing a wider range of substrate and film thicknesses. Mechanical analysis to obtain high temperature properties of ceramics would also aid this work. Beyond curvature, unexpected behaviors like misorientation of bending direction warrant further investigation and expansion of current models to include a wider number of outside forces. This experimental system also enables the investigation of sheets at scales currently unexplored, hopefully introducing exciting new deformation patterns. These potential future studies just deal with homogenous bilayer shrinkage. The ability to pattern the deposited film on both sides of the substrate introduces a seemingly limitless number of questions to be explored regarding interactions between pattern scale and sheet scale, periodic and nonperiodic patterns, trilayer shrinkage, and many more. In addition to answering these fundamental questions, we can begin to apply this technique to produce intricate objects for a myriad of applications as active materials, structural materials, and even artisanal materials as shown in Figure 5.2.

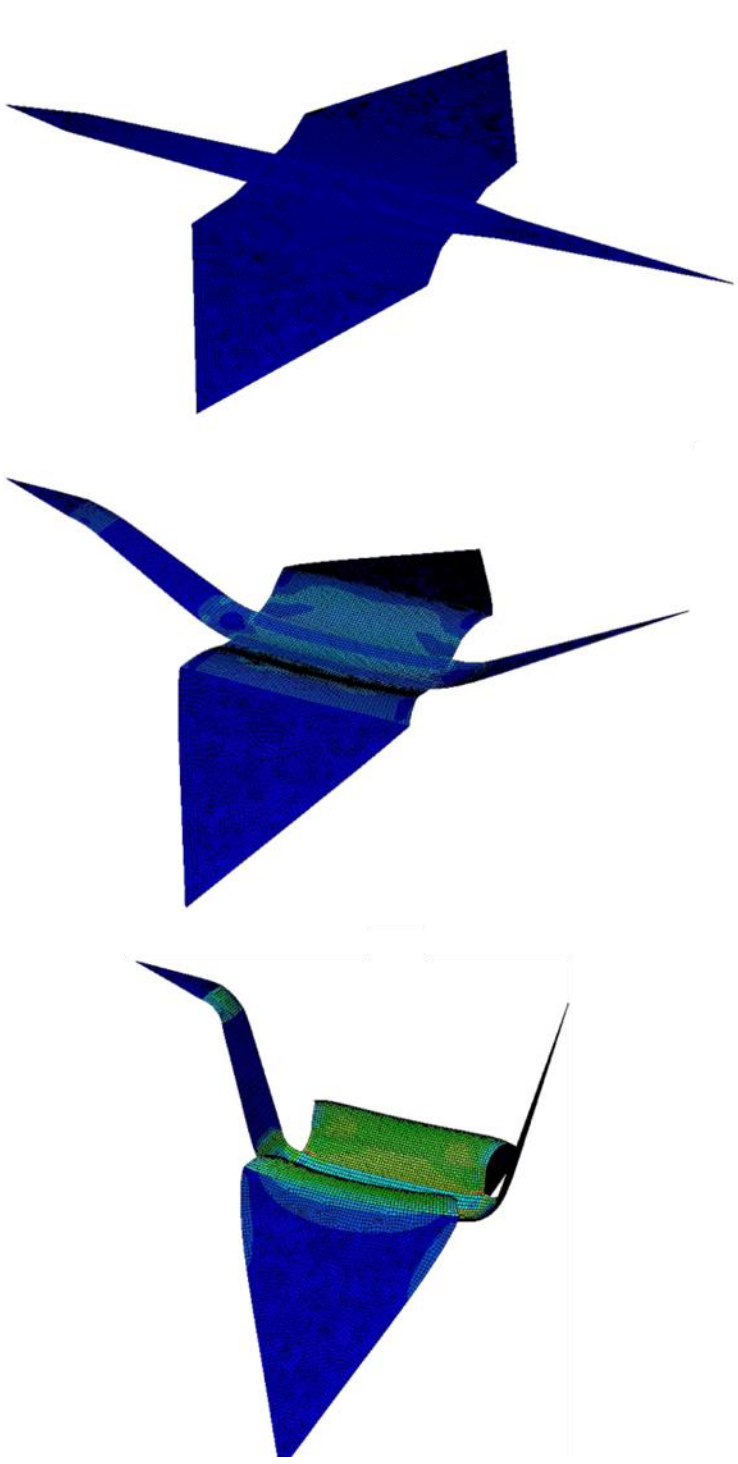

Figure 5.2: *Composite shell FEM model of self-shaping ceramic crane.*

6. References

[1] J. Binner, M. Porter, B. Baker, J. Zou, V. Venkatachalam, V. R. Diaz, A. D'Angio, P. Ramanujam, T. Zhang, and T. S. R. C. Murthy, *Selection, Processing, Properties and Applications of Ultra-High Temperature Ceramic Matrix Composites, UHTCMCs – a Review*, International Materials Reviews **65**, 389 (2020).

[2] E. Ivers-Tiffée, A. Weber, and D. Herbstritt, *Materials and Technologies for SOFC-Components*, J Eur Ceram Soc **21**, 1805 (2001).

[3] E. Feizi and A. K. Ray, *12CaO.7Al Ceramic: A Review of the Electronic and Optoelectronic Applications in Display Devices*, Journal of Display Technology **12**, 451 (2016).

[4] H. Hassanin, K. Essa, A. Elshaer, M. Imbaby, H. H. El-Mongy, and T. A. El-Sayed, *Micro-Fabrication of Ceramics: Additive Manufacturing and Conventional Technologies*, Journal of Advanced Ceramics **10**, 1 (2021).

[5] I. Denry and J. A. Holloway, *Ceramics for Dental Applications: A Review*, Materials **3**, 351 (2010).

[6] R. K. Bordia and A. Jagota, *Crack Growth and Damage in Constrained Sintering Films*, Journal of the American Ceramic Society **76**, 2475 (1993).

[7] J. Xie, W. Hao, and F. Wang, *Crack Propagation of Planar and Corrugated Solid Oxide Fuel Cells during Cooling Process*, Int J Energy Res **43**, 3020 (2019).

[8] B. N. Nguyen, B. J. Koeppel, S. Ahzi, M. A. Khaleel, and P. Singh, *Crack Growth in Solid Oxide Fuel Cell Materials: From Discrete to Continuum Damage Modeling*, Journal of the American Ceramic Society **89**, 1358 (2006).

[9] Z. Xiang, S. Haibo, W. Fenghui, L. Kang, and H. Jianye, *Curvature Reversal and Residual Stress in Solid Oxide Fuel Cell Induced by Chemical Shrinkage and Expansion*, Fuel Cells **14**, 1057 (2014).

[10] J. M. Klein, Y. Bultel, S. Georges, and M. Pons, *Modeling of a SOFC Fuelled by Methane: From Direct Internal Reforming to Gradual Internal Reforming*, Chem Eng Sci **62**, 1636 (2007).

[11] Y. Shiratori, T. Ijichi, T. Oshima, and K. Sasaki, *Internal Reforming SOFC Running on Biogas*, Int J Hydrogen Energy **35**, 7905 (2010).

[12] V. Chiodo, A. Galvagno, A. Lanzini, D. Papurello, F. Urbani, M. Santarelli, and S. Freni, *Biogas Reforming Process Investigation for SOFC Application*, Energy Convers Manag **98**, 252 (2015).

[13] N. Chatrattanawet, D. Saebea, S. Authayanun, A. Arpornwichanop, and Y. Patcharavorachot, *Performance and Environmental Study of a Biogas-Fuelled Solid Oxide Fuel Cell with Different Reforming Approaches*, Energy **146**, 131 (2018).

[14] K. W. Lin and H. W. Wu, *Hydrogen-Rich Syngas Production and Carbon Dioxide Formation Using Aqueous Urea Solution in Biogas Steam Reforming by Thermodynamic Analysis*, Int J Hydrogen Energy **45**, 11593 (2020).

[15] R. P. O'Hayre, S.-W. Cha, W. G. Colella, and F. B. Prinz, *Fuel Cell Fundamentals*, Third Edit (John W, Hoboken, NJ, USA, 2016).

[16] R. J. Milcarek and J. Ahn, *Micro-Tubular Flame-Assisted Fuel Cells Running Methane, Propane and Butane: On Soot, Efficiency and Power Density*, Energy **169**, 776 (2018).

[17] R. J. Milcarek and J. Ahn, *Rich-Burn, Flame-Assisted Fuel Cell, Quick-Mix, Lean-Burn (RFQL) Combustor and Power Generation*, J Power Sources **381**, 18 (2018).

[18] R. J. Milcarek, M. J. Garrett, and J. Ahn, *Micro-Tubular Flame-Assisted Fuel Cell Stacks*, Int J Hydrogen Energy **41**, 21489 (2016).

[19] K. Wang, R. J. Milcarek, P. Zeng, and J. Ahn, *Flame-Assisted Fuel Cells Running Methane*, Int J Hydrogen Energy **40**, 4659 (2015).

[20] R. J. Milcarek, M. J. Garrett, K. Wang, and J. Ahn, *Micro-Tubular Flame-Assisted Fuel Cells Running Methane*, Int J Hydrogen Energy **41**, 20670 (2016).

[21] R. J. Milcarek, M. Chu, and J. Ann, *Investigation of a Solid Oxide Fuel Cell in a Residential Furnace during Rapid Thermal Cycling*, ASHRAE Trans **125**, 27 (2019).

[22] R. J. Milcarek, V. P. DeBiase, and J. Ahn, *Investigation of Startup, Performance and Cycling of a Residential Furnace Integrated with Micro-Tubular Flame-Assisted Fuel Cells for Micro-Combined Heat and Power*, Energy **196**, 117148 (2020).

[23] M. H. Lewis and R. S. Dobedoe, *Creep of Ceramics*, Encyclopedia of Materials: Science and Technology **23**, 1 (2002).

[24] J. Laurencin, G. Delette, F. Usseglio-Viretta, and S. di Iorio, *Creep Behaviour of Porous SOFC Electrodes: Measurement and Application to Ni-8YSZ Cermets*, J Eur Ceram Soc **31**, 1741 (2011).

[25] Y. C. Zhang, W. Jiang, S. T. Tu, J. F. Wen, and W. Woo, *Using Short-Time Creep Relaxation Effect to Decrease the Residual Stress in the Bonded Compliant Seal of Planar Solid Oxide Fuel Cell - A Finite Element Simulation*, J Power Sources **255**, 108 (2014).

[26] A. Lucantonio, P. Nardinocchi, and M. Pezzulla, *Swelling-Induced and Controlled Curving in Layered Gel Beams*, Proceedings of the Royal Society A: Mathematical, Physical and Engineering Sciences **470**, (2014).

[27] J. H. Na, A. A. Evans, J. Bae, M. C. Chiappelli, C. D. Santangelo, R. J. Lang, T. C. Hull, and R. C. Hayward, *Programming Reversibly Self-Folding Origami with Micropatterned Photo-Crosslinkable Polymer Trilayers*, Advanced Materials **27**, 79 (2015).

[28] Y. Liu, B. Shaw, M. D. Dickey, and J. Genzer, *Sequential Self-Folding of Polymer Sheets*, Sci Adv **3**, 1 (2017).

[29] J. Jeong, Y. Cho, S. Y. Lee, X. Gong, R. D. Kamien, S. Yang, and A. G. Yodh, *Topography-Guided Buckling of Swollen Polymer Bilayer Films into Three-Dimensional Structures*, Soft Matter **13**, 956 (2017).

[30] J. Cui, J. G. M. Adams, and Y. Zhu, *Controlled Bending and Folding of a Bilayer Structure Consisting of a Thin Stiff Film and a Heat Shrinkable Polymer Sheet*, Smart Mater Struct **27**, 055009 (2018).

[31] X.-D. Cheng, W.-L. Song, M. Chen, X. Yuan, Y. Yang, and D. Fang, *Metallic Origami Metastructures for High-Temperature Low Electromagnetic Reflectivity*, J Mater Sci **54**, 6425 (2019).

[32] Y. Zhao, M. S. Nandra, and Y. C. Tai, *A MEMS Intraocular Origami Coil*, in *2011 16th International Solid-State Sensors, Actuators and Microsystems Conference* (IEEE, 2011), pp. 2172–2175.

[33] F. L. Bargardi, H. le Ferrand, R. Libanori, and A. R. Studart, *Bio-Inspired Self-Shaping Ceramics*, Nat Commun **7**, 13912 (2016).

[34] K. Huang, H. Elsayed, G. Franchin, and P. Colombo, *Complex SiOC Ceramics from 2D Structures by 3D Printing and Origami*, Addit Manuf **33**, 101144 (2020).

[35] G. Liu, Y. Zhao, G. Wu, and J. Lu, Origami and 4D Printing of Elastomer-Derived Ceramic Structures, 2018.

[36] Z. Ding, H. Zreiqat, and M. Mirkhalaf, *Rationally-Designed Self-Shaped Ceramics through Heterogeneous Green Body Compositions*, Mater Horiz **9**, 2762 (2022).

[37] Y. Tao et al., *Morphing Pasta and Beyond*, Sci Adv **7**, 1 (2021).

[38] Z. Zhao, J. Kumar, Y. Hwang, J. Deng, M. S. Bin Ibrahim, C. Huang, S. Suresh, and N.-J. Cho, *Digital Printing of Shape-Morphing Natural Materials*, Proceedings of the National Academy of Sciences **118**, (2021).

[39] S. Timoshenko, *Analysis of Bi-Metal Thermostats*, J Opt Soc Am **11**, 233 (1925).

[40] G. G. Stoney, *The Tension of Metallic Films Deposited by Electrolysis*, Proceedings of the Royal Society of London. Series A, Containing Papers of a Mathematical and Physical Character **82**, 172 (1909).

[41] M. Pezzulla, G. P. Smith, P. Nardinocchi, and D. P. Holmes, *Geometry and Mechanics of Thin Growing Bilayers*, Soft Matter **12**, 4435 (2016).

[42] S. Alben, B. Balakrisnan, and E. Smela, *Edge Effects Determine the Direction of Bilayer Bending*, Nano Lett **11**, 2280 (2011).

[43] K. Hamamoto, T. Suzuki, B. Liang, T. Yamaguchi, H. Sumi, Y. Fujishiro, B. Ingram, A. Jeremy Kropf, and J. David Carter, *Investigation of the Microstructural Effect of Ni–Yttria Stabilized Zirconia Anode for Solid-Oxide Fuel Cell Using Micro-Beam X-Ray Absorption Spectroscopy Analysis*, J Power Sources **222**, 15 (2013).

[44] K. Amezawa, *Operando XAFS Analysis of Solid Oxide Fuel Cells (SOFCs)*, Vacuum and Surface Science **62**, 21 (2019).

[45] Y. Du and N. M. Sammes, *Fabrication and Properties of Anode-Supported Tubular Solid Oxide Fuel Cells*, J Power Sources **136**, 66 (2004).

[46] S. Lee, M. Park, H. Kim, K. J. Yoon, J. W. Son, J. H. Lee, B. K. Kim, W. Choi, and J. Hong, *Thermal Conditions and Heat Transfer Characteristics of High-Temperature Solid Oxide Fuel Cells Investigated by Three-Dimensional Numerical Simulations*, Energy **120**, 293 (2017).

[47] M. Mangold, M. Krasnyk, and K. Sundmacher, *Theoretical Investigation of Steady State Multiplicities in Solid Oxide Fuel Cells*, J Appl Electrochem **36**, 265 (2006).

[48] R. J. Milcarek, K. Wang, R. L. Falkenstein-Smith, and J. Ahn, *Performance Variation with SDC Buffer Layer Thickness*, Int J Hydrogen Energy **41**, 9500 (2016).

[49] D. Chen, G. Yang, Z. Shao, and F. Ciucci, *Nanoscaled Sm-Doped CeO2 Buffer Layers for Intermediate- Temperature Solid Oxide Fuel Cells*, Electrochem Commun **35**, 131 (2013).

[50] A. R. Hartwell, T. S. Welles, and J. Ahn, *The Anode Supported Internal Cathode Tubular Solid Oxide Fuel Cell: Novel Production of a Cell Geometry for Combined Heat and Power Applications*, Int J Hydrogen Energy **46**, 37429 (2021).

[51] A. R. Hartwell and J. Ahn, *Complex Material Behavior Seen with Novel Internal Cathode Tubular Solid Oxide Fuel Cells*, in *Proceedings of the ASME 2021 International Mechanical Engineering Congress & Exposition (IMECE 2021)* (2021).

[52] A. R. Hartwell, C. A. Wilhelm, T. S. Welles, R. J. Milcarek, and J. Ahn, *Effects of Synthesis Gas Concentration, Composition, and Operational Time on Tubular Solid Oxide Fuel Cell Performance*, Sustainability **14**, 7983 (2022).

[53] Y. Orikasa, T. Ina, T. Nakao, A. Mineshige, K. Amezawa, M. Oishi, H. Arai, Z. Ogumi, and Y. Uchimoto, *X-Ray Absorption Spectroscopic Study on La0.6Sr 0.4CoO3-δ Cathode Materials Related with Oxygen Vacancy Formation*, Journal of Physical Chemistry C **115**, 16433 (2011).

[54] Y. Fujimaki, H. Watanabe, Y. Terada, T. Nakamura, K. Yashiro, S. -i. Hashimoto, T. Kawada, and K. Amezawa, *Direct Evaluation of Oxygen Chemical Potential Distribution in an SOFC Cathode by In Situ X-Ray Absorption Spectroscopy*, ECS Trans **57**, 1925 (2013).

[55] J. W. Fergus, *Sealants for Solid Oxide Fuel Cells*, J Power Sources **147**, 46 (2005).

[56] T. Suzuki, T. Yamaguchi, Y. Fujishiro, and M. Awano, *Improvement of SOFC Performance Using a Microtubular, Anode-Supported SOFC*, J Electrochem Soc **153**, A925 (2006).

[57] R. J. Milcarek, M. J. Garrett, T. S. Welles, and J. Ahn, *Performance Investigation of a Micro-Tubular Flame-Assisted Fuel Cell Stack with 3,000 Rapid Thermal Cycles*, J Power Sources **394**, 86 (2018).

[58] R. J. Milcarek, J. Ahn, and J. Zhang, *Review and Analysis of Fuel Cell-Based, Micro-Cogeneration for Residential Applications: Current State and Future Opportunities*, Sci Technol Built Environ **23**, 1224 (2017).

[59] R. J. Milcarek, K. Wang, R. L. Falkenstein-Smith, and J. Ahn, *Micro-Tubular Flame-Assisted Fuel Cells for Micro-Combined Heat and Power Systems*, J Power Sources **306**, 148 (2016).

[60] K. Wang, P. Zeng, and J. Ahn, *High Performance Direct Flame Fuel Cell Using a Propane Flame*, Proceedings of the Combustion Institute **33**, 3431 (2011).

[61] Y. Wang, Y. Shi, X. Yu, N. Cai, J. Qian, and S. Wang, *Experimental Characterization of a Direct Methane Flame Solid Oxide Fuel Cell Power Generation Unit* , J Electrochem Soc **161**, F1348 (2014).

[62] Y. Wang, Y. Shi, M. Ni, and N. Cai, *A Micro Tri-Generation System Based on Direct Flame Fuel Cells for Residential Applications*, Int J Hydrogen Energy **39**, 5996 (2014).

[63] Y. Wang, H. Zeng, T. Cao, Y. Shi, N. Cai, X. Ye, and S. Wang, *Start-up and Operation Characteristics of a Flame Fuel Cell Unit*, Appl Energy **178**, 415 (2016).

[64] Y. Wang, H. Zeng, Y. Shi, T. Cao, N. Cai, X. Ye, and S. Wang, *Power and Heat Co-Generation by Micro-Tubular Flame Fuel Cell on a Porous Media Burner*, Energy **109**, 117 (2016).

[65] M. Rahaman, *Ceramic Processing*, 1st ed. (CRC Press, Boca Raton, FL, 2007).

[66] X. Wang, Z. Chen, and A. Atkinson, *Crack Formation in Ceramic Films Used in Solid Oxide Fuel Cells*, J Eur Ceram Soc **33**, 2539 (2013).

[67] E. Santanach Carreras, F. Chabert, D. E. Dunstan, and G. v. Franks, *Avoiding "Mud" Cracks during Drying of Thin Films from Aqueous Colloidal Suspensions*, J Colloid Interface Sci **313**, 160 (2007).

[68] M. N. Rahaman, *Sintering of Ceramics* (2007).

[69] N. H. Menzler, F. Tietz, S. Uhlenbruck, H. P. Buchkremer, and D. Stöver, *Materials and Manufacturing Technologies for Solid Oxide Fuel Cells*, Journal of Materials Science.

[70] D. U. Tulyaganov, A. A. Reddy, V. v. Kharton, and J. M. F. Ferreira, *Aluminosilicate-Based Sealants for SOFCs and Other Electrochemical Applications - A Brief Review*, J Power Sources **242**, 486 (2013).

[71] H. Shi, G. Yang, Z. Liu, G. Zhang, R. Ran, Z. Shao, W. Zhou, and W. Jin, *High Performance Tubular Solid Oxide Fuel Cells with BSCF Cathode*, Int J Hydrogen Energy **37**, 13022 (2012).

[72] P. Sarkar, L. Yamarte, H. Rho, and L. Johanson, *Anode-Supported Tubular Micro-Solid Oxide Fuel Cell*, Int J Appl Ceram Technol **4**, 103 (2007).

[73] N. Droushiotis, U. Doraswami, G. H. Kelsall, and K. Li, *Micro-Tubular Solid Oxide Fuel Cells Fabricated from Hollow Fibres*, J Appl Electrochem **41**, 1005 (2011).

[74] T. Suzuki, Y. Funahashi, T. Yamaguchi, Y. Fujishiro, and M. Awano, *Cube-Type Micro SOFC Stacks Using Sub-Millimeter Tubular SOFCs*, J Power Sources **183**, 544 (2008).

[75] W. Winkler and J. Krüger, *Design and Manufacturing of a Tubular Solid Oxide Fuel Cell Combustion System*, J Power Sources **71**, 244 (1998).

[76] N. M. Sammes, Y. Du, and R. Bove, *Design and Fabrication of a 100W Anode Supported Micro-Tubular SOFC Stack*, J Power Sources **145**, 428 (2005).

[77] R. J. Milcarek and J. Ahn, *Micro-Tubular Flame-Assisted Fuel Cell Power Generation Running Propane and Butane*, in *Volume 2: Heat Exchanger Technologies; Plant Performance; Thermal Hydraulics and Computational Fluid Dynamics; Water Management for Power Systems; Student Competition* (ASME, 2018), p. V002T12A002.

[78] R. J. Milcarek, H. Nakamura, T. Tezuka, K. Maruta, and J. Ahn, *Microcombustion for Micro-Tubular Flame-Assisted Fuel Cell Power and Heat Cogeneration*, J Power Sources **413**, 191 (2019).

[79] L. Zhou, M. Cheng, B. Yi, Y. Dong, Y. Cong, and W. Yang, *Performance of an Anode-Supported Tubular Solid Oxide Fuel Cell (SOFC) under Pressurized Conditions*, Electrochim Acta **53**, 5195 (2008).

[80] X. F. Ye, C. Yuan, Y. P. Chen, C. Y. Zhong, Z. L. Zhan, and S. R. Wang, *Micro-Tubular Solid Oxide Fuel Cells and Their Stacks Running on Direct Ethanol Fuels*, J Electrochem Soc **161**, F894 (2014).

[81] J. Durango-Petro, J. Usuba, H. Valle, G. Abarzua, H. Flies, R. Udayabhaskar, and R. v. Mangalaraja, *Ascendable Method for the Fabrication of Micro-Tubular Solid Oxide Fuel Cells by Ram-Extrusion Technique*, Ceram Int **46**, 2602 (2020).

[82] Y. Wang, Y. Shi, N. Cai, X. Ye, and S. Wang, *Performance Characteristics of a Micro-Tubular Solid Oxide Fuel Cell Operated with a Fuel-Rich Methane Flame*, ECS Trans **68**, 2237 (2015).

[83] T. S. Welles and J. Ahn, *Novel Investigation of Perovskite Membrane Based Electrochemical Nitric Oxide Control Phenomenon*, Sci Rep **10**, (2020).

[84] D. Hanft, J. Exner, M. Schubert, T. Stöcker, P. Fuierer, and R. Moos, *An Overview of the Aerosol Deposition Method: Process Fundamentals and New Trends in Materials Applications*, Journal of Ceramic Science and Technology.

[85] J. Akedo, *Room Temperature Impact Consolidation and Application to Ceramic Coatings: Aerosol Deposition Method*, Journal of the Ceramic Society of Japan **128**, 101 (2020).

[86] S. Taleb, M. A. Badillo-Ávila, and M. Acuautla, *Fabrication of Poly (Vinylidene Fluoride) Films by Ultrasonic Spray Coating; Uniformity and Piezoelectric Properties*, Mater Des **212**, (2021).

[87] I. Strawbridge and P. F. James, *The Factors Affecting the Thickness of Sol-Gel Derived Silica Coating Prepared by Dipping*, J Non Cryst Solids **86**, 381 (1986).

[88] D. Zhang, E. Peng, R. Borayek, and J. Ding, *Controllable Ceramic Green-Body Configuration for Complex Ceramic Architectures with Fine Features*, Adv Funct Mater **29**, (2019).

[89] T. A. Pham, D. P. Kim, T. W. Lim, S. H. Park, D. Y. Yang, and K. S. Lee, *Three-Dimensional SiCN Ceramic Microstructures via Nano-Stereolithography of Inorganic Polymer Photoresists*, Adv Funct Mater **16**, 1235 (2006).

[90] M. Zhou, W. Liu, H. Wu, X. Song, Y. Chen, L. Cheng, F. He, S. Chen, and S. Wu, *Preparation of a Defect-Free Alumina Cutting Tool via Additive Manufacturing Based on*

Stereolithography – Optimization of the Drying and Debinding Processes, Ceram Int **42**, 11598 (2016).

[91] R. He, W. Liu, Z. Wu, D. An, M. Huang, H. Wu, Q. Jiang, X. Ji, S. Wu, and Z. Xie, *Fabrication of Complex-Shaped Zirconia Ceramic Parts via a DLP- Stereolithography-Based 3D Printing Method*, Ceram Int **44**, 3412 (2018).

[92] M. L. Griffith and J. W. Halloran, *Freeform Fabrication of Ceramics via Stereolithography*, Journal of the American Ceramic Society **79**, 2601 (2005).

[93] Z. Chen, D. Li, W. Zhou, and L. Wang, *Curing Characteristics of Ceramic Stereolithography for an Aqueous-Based Silica Suspension*, Proc Inst Mech Eng B J Eng Manuf **224**, 641 (2010).

[94] R. Wang, D. Gu, K. Lin, C. Chen, Q. Ge, and D. Li, *Multi-Material Additive Manufacturing of a Bio-Inspired Layered Ceramic/Metal Structure: Formation Mechanisms and Mechanical Properties*, Int J Mach Tools Manuf **175**, (2022).

[95] S. Weingarten, U. Scheithauer, R. Johne, J. Abel, E. Schwarzer, T. Moritz, and A. Michaelis, *Multi-Material Ceramic-Based Components - Additive Manufacturing of Blackand- White Zirconia Components by Thermoplastic 3D-Printing (CerAM - T3DP)*, Journal of Visualized Experiments **2019**, (2019).

[96] R. Wick-Joliat, M. Schroffenegger, and D. Penner, *Multi-Material Ceramic Material Extrusion 3D Printing with Granulated Injection Molding Feedstocks*, Ceram Int **49**, 6361 (2023).

[97] J. Wu, Z. Qin, L. Qu, H. Zhang, F. Deng, and M. Guo, *Natural Hydrogel in American Lobster: A Soft Armor with High Toughness and Strength*, Acta Biomater **88**, 102 (2019).

[98] A. L. Mackay, *Periodic Minimal Surfaces*, Physics (College Park Md) **131**, 300 (1985).

[99] S. Giraud and J. Canel, *Young's Modulus of Some SOFCs Materials as a Function of Temperature*, J Eur Ceram Soc **28**, 77 (2008).

[100] M. Pihlatie, A. Kaiser, and M. Mogensen, *Mechanical Properties of NiO/Ni–YSZ Composites Depending on Temperature, Porosity and Redox Cycling*, J Eur Ceram Soc **29**, 1657 (2009).

[101] P. Fu, M. Yan, M. Zeng, and Q. Wang, *Sintering Process Simulation of a Solid Oxide Fuel Cell Anode and Its Predicted Thermophysical Properties*, Appl Therm Eng **125**, 209 (2017).

[102] H. Hayashi, M. Kanoh, C. J. Quan, H. Inaba, S. Wang, M. Dokiya, and H. Tagawa, *Thermal Expansion of Gd-Doped Ceria and Reduced Ceria*, Solid State Ion **132**, 227 (2000).

[103] H. Hayashi, T. Saitou, N. Maruyama, H. Inaba, K. Kawamura, and M. Mori, *Thermal Expansion Coefficient of Yttria Stabilized Zirconia for Various Yttria Contents*, Solid State Ion **176**, 613 (2005).

[104] N. Li, *The Interaction of LSM-YSZ Composite and Improvement of the Solid Oxide Cell Durability by Mn-Modified YSZ*, Doctoral Dissertations 320 (2014).

[105] D. W. Ni, B. Charlas, K. Kwok, T. T. Molla, P. V. Hendriksen, and H. L. Frandsen, *Influence of Temperature and Atmosphere on the Strength and Elastic Modulus of Solid Oxide Fuel Cell Anode Supports*, J Power Sources **311**, 1 (2016).

[106] F. Greco, H. L. Frandsen, A. Nakajo, M. F. Madsen, and J. Van herle, *Modelling the Impact of Creep on the Probability of Failure of a Solid Oxide Fuel Cell Stack*, J Eur Ceram Soc **34**, 2695 (2014).

[107] M. Pezzulla, S. A. Shillig, P. Nardinocchi, and D. P. Holmes, *Morphing of Geometric Composites via Residual Swelling*, Soft Matter **11**, 5812 (2015).

[108] J. L. Silverberg, A. A. Evans, L. McLeod, R. C. Hayward, T. Hull, C. D. Santangelo, and I. Cohen, *Using Origami Design Principles to Fold Reprogrammable Mechanical Metamaterials*, Science (1979) **345**, 647 (2014).

[109] Z. Song, T. Ma, R. Tang, Q. Cheng, X. Wang, D. Krishnaraju, R. Panat, C. K. Chan, H. Yu, and H. Jiang, *Origami Lithium-Ion Batteries*, Nat Commun **5**, (2014).

[110] J. M. Zanardi et al., *Optical Actuation of Micromirrors Fabricated by the Micro-Origami Technique*, Appl Phys Lett **83**, 3647 (2003).

[111] X. Guo, H. Li, B. Yeop Ahn, E. B. Duoss, K. J. Hsia, J. A. Lewis, and R. G. Nuzzo, *Two- and Three-Dimensional Folding of Thin Film Single-Crystalline Silicon for Photovoltaic Power Applications*, Proceedings of the National Academy of Sciences **106**, 20149 (2009).

[112] Y. Klein, E. Efrati, and E. Sharon, *Shaping of Elastic Sheets by Prescription of Non-Euclidean Metrics*, Science (1979) **315**, 1116 (2007).

[113] A. M. Abdullah, P. v. Braun, and K. J. Hsia, *Bifurcation of Self-Folded Polygonal Bilayers*, Appl Phys Lett **111**, 104101 (2017).

[114] J. H. Na, N. P. Bende, J. Bae, C. D. Santangelo, and R. C. Hayward, *Grayscale Gel Lithography for Programmed Buckling of Non-Euclidean Hydrogel Plates*, Soft Matter **12**, 4985 (2016).

[115] M. Byun, C. D. Santangelo, and R. C. Hayward, *Swelling-Driven Rolling and Anisotropic Expansion of Striped Gel Sheets*, Soft Matter **9**, 8264 (2013).

[116] A. M. Abdullah, X. Li, P. v. Braun, J. A. Rogers, and K. J. Hsia, *Kirigami-Inspired Self-Assembly of 3D Structures*, Adv Funct Mater **30**, 1 (2020).

[117] J. Wang, N. Dai, C. Jiang, X. Mu, B. Zhang, Q. Ge, and D. Wang, *Programmable Shape-Shifting 3D Structures via Frontal Photopolymerization*, Mater Des **198**, 109381 (2021).

[118] Q. Guo et al., *Programmable 3D Self-Folding Structures with Strain Engineering*, Advanced Intelligent Systems **2**, 2000101 (2020).

[119] I. Levin and E. Sharon, *Anomalously Soft Non-Euclidean Springs*, Phys Rev Lett **116**, 035502 (2016).

[120] E. Efrati, E. Sharon, and R. Kupferman, *Buckling Transition and Boundary Layer in Non-Euclidean Plates*, Phys Rev E **80**, 016602 (2009).

[121] E. Sharon and E. Efrati, *The Mechanics of Non-Euclidean Plates*, Soft Matter **6**, 5693 (2010).

[122] A. M. Abdullah, K. Nan, J. A. Rogers, and K. J. Hsia, *Mismatch Strain Programmed Shape Transformation of Curved Bilayer-Flexible Support Assembly*, Extreme Mech Lett **7**, 34 (2016).

[123] S. Li, D. M. Vogt, D. Rus, and R. J. Wood, *Fluid-Driven Origami-Inspired Artificial Muscles*, Proc Natl Acad Sci U S A **114**, 13132 (2017).

[124] T. van Manen, S. Janbaz, and A. A. Zadpoor, *Programming the Shape-Shifting of Flat Soft Matter*, Materials Today **21**, 144 (2018).

[125] S. J. Jeon and R. C. Hayward, *Simultaneous Control of Gaussian Curvature and Buckling Direction by Swelling of Asymmetric Trilayer Hydrogel Hybrids*, Soft Matter **16**, 688 (2020).

[126] C. F. Gauss, *General Investigations of Curved Surfaces* (Dover Publications, Inc., Mineola, NY, 2005).

[127] E. Siéfert, I. Levin, and E. Sharon, *Euclidean Frustrated Ribbons*, Phys Rev X **11**, (2021).

[128] I. S. Chun, A. Challa, B. Derickson, K. J. Hsia, and X. Li, *Geometry Effect on the Strain-Induced Self-Rolling of Semiconductor Membranes*, Nano Lett **10**, 3927 (2010).

[129] P. Cendula, S. Kiravittaya, I. Mönch, J. Schumann, and O. G. Schmidt, *Directional Roll-up of Nanomembranes Mediated by Wrinkling*, Nano Lett **11**, 236 (2011).

[130] M. M. Ripp, V. Démery, T. Zhang, and J. D. Paulsen, *Geometry Underlies the Mechanical Stiffening and Softening of an Indented Floating Film*, Soft Matter **16**, 4121 (2020).

[131] I. Tobasco, Y. Timounay, D. Todorova, G. C. Leggat, J. D. Paulsen, and E. Katifori, *Exact Solutions for the Wrinkle Patterns of Confined Elastic Shells*, Nat Phys **18**, 1099 (2022).

[132] Y. Timounay, R. De, J. L. Stelzel, Z. S. Schrecengost, M. M. Ripp, and J. D. Paulsen, *Crumples as a Generic Stress-Focusing Instability in Confined Sheets*, Phys Rev X **10**, 21008 (2020).

[133] Y. Timounay, A. R. Hartwell, M. He, D. E. King, L. K. Murphy, V. Démery, and J. D. Paulsen, *Sculpting Liquids with Ultrathin Shells*, Phys Rev Lett **127**, 108002 (2021).

[134] J. D. Paulsen, *Wrapping Liquids, Solids, and Gases in Thin Sheets*, Annu Rev Condens Matter Phys **10**, 431 (2019).

[135] J. D. Paulsen, V. Démery, C. D. Santangelo, T. P. Russell, B. Davidovitch, and N. Menon, *Optimal Wrapping of Liquid Droplets with Ultrathin Sheets*, Nat Mater **14**, 1206 (2015).

[136] J. D. Paulsen, V. Démery, K. Bu˘ Gra Toga, Z. Qiu, T. P. Russell, B. Davidovitch, and N. Menon, *Geometry-Driven Folding of a Floating Annular Sheet*, (2016).

[137] J. D. Paulsen, E. Hohlfeld, H. King, J. Huang, Z. Qiu, T. P. Russell, N. Menon, D. Vella, and B. Davidovitch, *Curvature-Induced Stiffness and the Spatial Variation of Wavelength in Wrinkled Sheets*, (n.d.).

[138] C. D. Coman and A. P. Bassom, *On the Wrinkling of a Pre-Stressed Annular Thin Film in Tension*, J Mech Phys Solids **55**, 1601 (2007).

[139] H. King, R. D. Schroll, B. Davidovitch, and N. Menon, *Elastic Sheet on a Liquid Drop Reveals Wrinkling and Crumpling as Distinct Symmetry-Breaking Instabilities*, Proceedings of the National Academy of Sciences **109**, 9716 (2012).

[140] W. Li, K. Hasinska, M. Seabaugh, S. Swartz, and J. Lannutti, *Curvature in Solid Oxide Fuel Cells*, J Power Sources **138**, 145 (2004).

[141] M. Chu, A. R. Hartwell, and J. Ahn, *Flame-Assisted Fuel Cell Boiler for Combined Heating and Micro-Power Generation*, in *Proceeding of the 16th International Conference on Flow Dynamics*, Vol. 28 (2019).

[142] A. R. Hartwell and J. Ahn, Novel Combined Heat and Power CHP System, 2020.

[143] D. J. L. Brett, A. Atkinson, N. P. Brandon, and S. J. Skinner, *Intermediate Temperature Solid Oxide Fuel Cells*, (2008).

[144] Y. Liu, S. I. Hashimoto, H. Nishino, K. Takei, M. Mori, T. Suzuki, and Y. Funahashi, *Fabrication and Characterization of Micro-Tubular Cathode-Supported SOFC for Intermediate Temperature Operation*, J Power Sources **174**, 95 (2007).

[145] R. J. Milcarek, K. Wang, M. J. Garrett, and J. Ahn, *Performance Investigation of Dual Layer Yttria-Stabilized Zirconia-Samaria-Doped Ceria Electrolyte for Intermediate Temperature Solid Oxide Fuel Cells*, Journal of Electrochemical Energy Conversion and Storage **13**, (2016).

[146] Z. Gao, L. V. Mogni, E. C. Miller, J. G. Railsback, and S. A. Barnett, *A Perspective on Low-Temperature Solid Oxide Fuel Cells*, Energy Environ Sci **9**, 1602 (2016).

[147] H. Huang, M. Nakamura, P. Su, R. Fasching, Y. Saito, and F. B. Prinz, *High-Performance Ultrathin Solid Oxide Fuel Cells for Low-Temperature Operation*, J Electrochem Soc **154**, B20 (2007).

[148] J. Ding, J. Liu, and G. Yin, *Fabrication and Characterization of Low-Temperature SOFC Stack Based on GDC Electrolyte Membrane*, J Memb Sci **371**, 219 (2011).

[149] B. Vanderstraeten, J. Berghmans, D. Tuerlinckx, B. Smit, E. Van't Oost, and S. Vliegen, *Experimental Study of the Pressure and Temperature Dependence on the Upper Flammability Limit of Methane/Air Mixtures*, J Hazard Mater **56**, 237 (1997).

[150] J. Malzbender, W. Fischer, and R. W. Steinbrech, *Studies of Residual Stresses in Planar Solid Oxide Fuel Cells*, J Power Sources **182**, 594 (2008).

[151] W. Jiang, Y. C. Zhang, W. Y. Zhang, Y. Luo, W. Woo, and S. T. Tu, *Growth and Residual Stresses in the Bonded Compliant Seal of Planar Solid Oxide Fuel Cell: Thickness Design of Window Frame*, Mater Des **93**, 53 (2016).

[152] W. Roger Cannon and T. G. Langdon, *Creep of Ceramics - Part 1 Mechanical Characteristics*, J Mater Sci **18**, 1 (1983).

[153] M. Sakai, H. Muto, and M. Haga, *Stress Relaxation of Polycrystalline Ceramics with Grain-Boundary Sliding and Grain Interlocking*, Journal of the American Ceramic Society **82**, 169 (1999).

[154] J. W. Fergus, R. Hui, X. Li, D. P. Wilkinson, and J. Zhang, *Solid Oxide Fuel Cells Materials Properties and Performance* (CRC Press, Boca Raton, FL, 2009).

[155] T. Nithyanantham, S. Biswas, S. N. Thangavel, and S. Bandopadhyay, *Studies on Phase Formation, Microstructure Development and Elastic Properties of Reduced NiO-8YSZ Anode Supported Bi-Layer Half-Cell Structures of Solid Oxide Fuel Cells*, Mater Res Bull **47**, 779 (2012).

[156] M. J. Jørgensen, S. Primdahl, C. Bagger, and M. Mogensen, *Effect of Sintering Temperature on Microstructure and Performance of LSM–YSZ Composite Cathodes*, Solid State Ion **139**, 1 (2001).

[157] I. Sabree, J. E. Gough, and B. Derby, *Mechanical Properties of Porous Ceramic Scaffolds: Influence of Internal Dimensions*, Ceram Int **41**, 8425 (2015).

[158] J. I. Gazzarri and O. Kesler, *Non-Destructive Delamination Detection in Solid Oxide Fuel Cells*, J Power Sources **167**, 430 (2007).

[159] Q. Fang, L. Blum, R. Peters, M. Peksen, P. Batfalsky, and D. Stolten, *SOFC Stack Performance under High Fuel Utilization*, Int J Hydrogen Energy **40**, 1128 (2015).

[160] A. R. Hartwell, C. VanNostrand, H. Kayton, Y. Murakami, H. Yakamura, and J. Ahn, *Internal Cathode Tubular Solid Oxide Fuel Cell Operating on Simulated Two-Stroke Internal Combustion Engine Exhaust*, in *Proceedings of the Nineteenth International Conference on Flow Dynamics* (2022).

[161] Y. Shi, C. Li, and N. Cai, *Experimental Characterization and Mechanistic Modeling of Carbon Monoxide Fueled Solid Oxide Fuel Cell*, J Power Sources **196**, 5526 (2011).

[162] W. Yao, Hydrogen and Carbon Monoxide Electrochemical Oxidation Reaction Kinetics on Solid Oxide Fuel Cell Anodes, 2013.

[163] A. Metcalf, T. Welles, Y. Murakami, H. Nakamura, and J. Ahn, *Unmanned Aerial Vehicle Solid Oxide Fuel Cell and Internal Combustion Engine Hybrid Powertrain: An Experimental and Simulation Centered Review*, in *Proceeding of the ASME 2022 POWER Conference* (Pittsburgh, Pennsylvania, 2022).

[164] A. R. Hartwell and J. Ahn, *Integration of Novel Geometry Solid Oxide Fuel Cells into a Residential Furnace/Boiler*, in *Proceedings of the ASME 2020 Power Conference (Power 2020)* (2020).

[165] S. W. Freiman and J. J. Mecholsky, *The Fracture of Brittle Materials* (John Wiley & Sons, Inc., Hoboken, NJ, USA, 2012).

[166] J. Ahn, P. D. Ronney, Z. Shao, and S. M. Haile, *A Thermally Self-Sustaining Miniature Solid Oxide Fuel Cell*, J Fuel Cell Sci Technol **6**, 0410041 (2009).

[167] J. Ahn, *Swiss Roll Heat Exchangers/Reactors and Solid-Oxide-Fuel-Cells Power Generation* (VDM Verlag Dr.Muller Aktiengesellschaft & Co. KG, Saarbrucken, 2008).

[168] M. Bianco, J. P. Ouweltjes, and J. Van herle, *Degradation Analysis of Commercial Interconnect Materials for Solid Oxide Fuel Cells in Stacks Operated up to 18000 Hours*, Int J Hydrogen Energy **44**, 31406 (2019).

[169] Z. Yang, *Recent Advances in Metallic Interconnects for Solid Oxide Fuel Cells*, International Materials Reviews **53**, 39 (2008).

[170] T. L. Cable, J. A. Setlock, S. C. Farmer, and A. J. Eckel, *Regenerative Performance of the NASA Symmetrical Solid Oxide Fuel Cell Design*, Int J Appl Ceram Technol **8**, 1 (2011).

[171] A. R. Hartwell and J. Ahn, *Utilizing Bilayer Shrinkage to Assemble Complex Ceramic Shapes*, in *Proceedings of the ASME 2022 International Mechanical Engineering Congress & Exposition (IMECE 2022)* (2022).

[172] Z. J. Wang, C. N. Zhu, W. Hong, Z. L. Wu, and Q. Zheng, *Cooperative Deformations of Periodically Patterned Hydrogels*, Sci Adv **3**, (2017).

[173] A. R. Hartwell, S. K. Elsayed, Z. Qin, and J. Ahn, *Using Simulation and Experiment to Develop a Design Methodology for Self-Shaping Solid Oxide Fuel Cell Multilayer Ceramic Composites*, in *Proceeding of the ASME 2023 POWER Conference* (2023).

[174] Q. Huang et al., *Shell Microelectrode Arrays (MEAs) for Brain Organoids*, Sci Adv **8**, 5031 (2022).

[175] F. Tietz, *Thermal Expansion of SOFC Materials*, Ionics (Kiel) **5**, (1999).

[176] S. Farhad, F. Hamdullahpur, and Y. Yoo, *Performance Evaluation of Different Configurations of Biogas-Fuelled SOFC Micro-CHP Systems for Residential Applications*, Int J Hydrogen Energy **35**, 3758 (2010).

[177] M. Gandiglio, A. Lanzini, M. Santarelli, M. Acri, T. Hakala, and M. Rautanen, *Results from an Industrial Size Biogas-Fed SOFC Plant (the DEMOSOFC Project)*, Int J Hydrogen Energy **45**, 5449 (2020).

[178] I. Ullah Khan, M. Hafiz Dzarfan Othman, H. Hashim, T. Matsuura, A. F. Ismail, M. Rezaei-DashtArzhandi, and I. Wan Azelee, *Biogas as a Renewable Energy Fuel – A Review of Biogas Upgrading, Utilisation and Storage*, Energy Convers Manag **150**, 277 (2017).

[179] M. J. Garrett, R. Falkenstein-Smith, R. J. Milcarek, and J. Ahn, *Biogas Combustion Characterization for Flame Fuel Cell Utilization*, in *10th U.S. National Combustion Meeting*, Vols. 2017-April (2017).

7. Curriculum Vitae

EDUCATION

Syracuse University
Ph.D. Mechanical and Aerospace Engineering **May 2023**
M.S. Mechanical and Aerospace Engineering **Dec. 2020**

State University of New York (SUNY) Polytechnic Institute
B.S. Nanoscale Engineering and B.S. Applied Mathematics **May 2018**

RESEARCH AND TEACHING INTERESTS

Research Interests: solid oxide fuel cells, 4D printing, multilayer ceramic composites, thin film deposition, energy systems, heating ventilation and air conditioning systems, combined heat and power, bioinspiration

Teaching Interests: thermodynamics, heat transfer, combustion, energy conversion, nanotechnology

AWARDS

- 1st Place Oral Presentation Competition Energy, Environment & Smart Materials **2023**
- Graduate Dean's Award for Excellence in Research and Creative Work **2023**
- First Place Graduate Non-Design Category at the 2023 New York State Green Building Conference Student Poster Competition **2023**
- Syracuse University Summer Dissertation Fellowship **2022**
- 3rd Place Syracuse University Engineering and Computer Science Research Day Poster Presentation **2022**
- 2nd Place Syracuse University Engineering and Computer Science Research Day Oral Presentation **2021**
- 3rd Place Syracuse University Engineering and Computer Science Research Day Pitch Competition **2020**
- Syracuse University Graduate Fellowship **2019 – 2020**
- 1st place Syracuse University Research for Undergraduates Summer Symposium **2017**
- Undergraduate Fellowship for Excellence in Nanoscale Science and Engineering **2014 – 2018**
- SUNY College of Nanoscale Science and Engineering President's List **2014 – 2018**

RESEARCH EXPERIENCE

Syracuse University, COMER Lab
Advisor: Dr. Jeongmin Ahn
Research Assistant **2018 – Current**

- Established an interdisciplinary research group consisting of four faculty members from three different Syracuse University departments
- Developed novel manufacturing techniques involving 4D printing of ceramics, thin film deposition, and production of fuel cell stack components
- Developed a novel geometry of solid oxide fuel cell to permit direct integration into combustion chambers

- Analyzed performance of solid oxide fuel cells in simulated combustion chambers using 4-point probe method, electrochemical impedance spectroscopy, and mass spectroscopy
- Determined impact of geometry on multilayer ceramic composite failure using scanning electron microscopy and finite element modeling
- Investigated doping of mycelium with heavy metals as material for use in solid oxide fuel cells and batteries
- Authored grant proposals for submission to intramural and intermural funding organizations including National Science Foundation (NSF), Department of Energy, and New York State Energy Research and Development Authority (NYSERDA)
- Worked on classified joint project with Lockheed Martin
- Prepared NYSERDA grant in partnership with Hydronic Shell

Lab Manager **2022 – Current**

- Advised, trained, and managed undergraduate and graduate researchers
- Compiled all lab procedures and recipes into centralized digital record
- Implemented improved organization and communication standards by updating signage and temporary written notices
- Maintained university safety standards and adopted new digital chemical inventory
- Coordinated materials and equipment purchasing
- Led lab tours for visiting faculty, students, and businesses

FirePower

Chief Technical Officer, Syracuse, NY **2019 – Current**

- Promoted commercialization of a resilient and high efficiency combined heat and power system consisting of a solid oxide fuel cell stack and boiler
- Carried out customer discovery as part of the NYSERDA Entrepreneur in Residence program and the NSF Innovation Corps program
- Performed interviews with industry technicians, sales representatives, contractors, and customers to establish product viability and identify market need

CNSE at SUNY Polytechnic Institute/Knolls Atomic Power Laboratory
Advisor: Dr. Nathanial Cady

Undergraduate Research Assistant **2017 – 2018**

- Investigated a method for fabricating a film using chemical bath deposition to replicate Chalk River Unidentified Deposit
- Characterized deposited film using scanning electron microscopy and atomic force microscopy
- Communicated with a team of professional engineers from the Knolls Atomic Power Laboratory on project advancements during monthly meetings

CNSE at SUNY Polytechnic Institute
Advisor: Dr. Nathanial Cady, Dr. Magnus Bergkvist

Undergraduate Research Assistant **2014 – 2018**

- Designed a three-dimensional model of a synthetic blood brain barrier using OnShape
- Operated Minitech 3-axis computer numerical controlled router (CNC). Work included initial machine installation, development of techniques to zero router to work surface, and optimization of tool movement for microscale manufacturing
- Developed a method of manufacturing microfluidic channels using CNC machining

- Produced microscale biomimetic polymer scaffolds using photolithography
- Designed photolithography exposure masks using KLayout to improve physical durability of scaffold

Syracuse University Soft Matter Program
Advisor: Dr. Joseph Paulsen
Undergraduate Research Assistant **Summer 2017**
- Investigated the deformation behaviors of ultrathin films
- Improved thin film manufacturing method via the addition of a sacrificial layer
- Used design of experiment methodology to examine effects of material dimensions and liquid properties on behaviors observed
- Recorded and analyzed data from over 100 films of unique dimensions using photo-processing and plotting software
- Adapted mathematical models to incorporate unique phenomena seen with non-Euclidean geometries

CNSE at SUNY Polytechnic Institute
Advisor: Dr. Carl Ventrice
High School Research Assistant **Summer 2014**
- Assisted with experiments using ultra-high vacuum chambers and sputtering techniques to examine graphene quality and growth
- Helped manufacture a system used to generate hydrogen plasma to remove oxide layer from extreme ultraviolet photolithography optical components
- Manufactured parts used in ultra-high vacuum systems

TEACHING EXPERIENCE

Syracuse University
Teaching Mentor – Teaching Assistant Orientation Program **2022**
Syracuse University Graduate School
- Introduced international and domestic graduate students beginning teaching assistant positions to fundamental teaching methodologies
- Led workshop on Science, Technology, Engineering, and Mathematics (STEM) teaching assistant responsibilities, problem-solving techniques, and methodologies to promote active learning in the classroom
- Led microteaching exercise to give teaching assistants feedback on teaching persona, communication skills, and usage of technology

Syracuse University
Teaching Assistant – Thermodynamics **2021 – 2022**
Dr. Jeongmin Ahn
- Prepared and presented lectures on power cycles and introductory thermodynamics concepts
- Created and instructed weekly recitation sections, graded and created homework assignments and examinations, assisted students during office hours

Syracuse University
Teaching Assistant – Statics **2021**
Dr. Edward Bogucz

- Created and instructed weekly recitation sections, graded homework assignments, assisted students during office hours

Syracuse University
Teaching Assistant – Introduction to Space Flight **2020**
Dr. Amit Sanyal
- Assisted students with course questions during office hours, graded homework, tests, and projects, assisted in making solution manuals as well as exams which could be administered virtually

Syracuse University
Teaching Assistant – Fuel Cell Science and Technology **2018 – 2022**
Dr. Jeongmin Ahn
- Instructed weekly lab sections, introduced graduate and undergraduate students to the manufacturing and testing processes related to solid oxide fuel cells, evaluated final project presentations

Syracuse University
Teaching Assistant – General Physics **2019**
Dr. Walter Freeman
- Instructed weekly recitation sections, offered individual help in a physics clinic, graded homework and exams

SUNY University at Albany
Tutor – Calculus I-II, Elementary Statistics, Physics I-II **2016 – 2017**
- Instructed undergraduate students within the SUNY Albany athletics program

PROFESSIONAL MEMBERSHIPS

- Member, American Society of Mechanical Engineers
- Member, Microscopy Society of America

REFEREED JOURNAL PUBLICATIONS

A. R. Hartwell, C. A. Wilhelm, T. S. Welles, R. J. Milcarek, J. Ahn, Effects of Synthesis Gas Concentration, Composition, and Operational Time on Tubular Solid Oxide Fuel Cell Performance. *Sustainability*. **14**, 7983 (2022).

A. R. Hartwell, T. S. Welles, J. Ahn, The Anode Supported Internal Cathode Tubular Solid Oxide Fuel Cell: Novel Production of a Cell Geometry For Combined Heat And Power Applications. *Int J Hydrogen Energy*. **46**, 37429–37439 (2021).

Y. Timounay, **A. R. Hartwell,** M. He, D. E. King, L. K. Murphy, V. Démery, J. D. Paulsen, Sculpting Liquids with Ultrathin Shells. Phys Rev Lett. **127**, 108002 (2021).

PATENTS

J. Ahn, **A. R. Hartwell,** Bilayer Shrinkage to Assemble Complex Ceramic Shapes. U.S. patent is filed (2022).

J. Ahn, **A. R. Hartwell,** Inside-out Anode Supported Microtubular Solid Oxide Fuel Cells. U.S. patent application is filed (2019).

TECHNICAL REPORTS

A. R. Hartwell, J. Ahn, "Novel Combined Heat and Power CHP System." New York State Energy Research and Development Authority Technical Report, Report Number 20-23 (2020).

CONFERENCE PROCEEDINGS

A. R. Hartwell, S. K. Elsayed, Z. Qin, J. Ahn, "Using Simulation and Experiment to Develop a Design Methodology for Self-Shaping Solid Oxide Fuel Cell Multilayer Ceramic Composites" in *Proceedings of the ASME 2023 POWER Conference (2023).*

A. R. Hartwell, C. VanNostrand, H. Kayton, Y. Murakami, H. Yakamura, J. Ahn, "Internal Cathode Tubular Solid Oxide Fuel Cell Operating on Simulated Two-Stroke Internal Combustion Engine Exhaust" in *Proceedings of the Nineteenth International Conference on Flow Dynamics* (2022).

A. R. Hartwell, J. Ahn, "Utilizing Bilayer Shrinkage to Assemble Complex Ceramic Shapes" in *Proceedings of the ASME 2022 International Mechanical Engineering Congress & Exposition (IMECE 2022)* (2022).

A. R. Hartwell, J. Ahn, "Internal Cathode Tubular Solid Oxide Fuel Cell Operating on Model Combustion Exhaust" in *Proceedings of the ASME 2022 Power Conference (POWER 2022)* (2022).

A. R. Hartwell, J. Ahn, "Complex Material Behavior Seen With Novel Internal Cathode Tubular Solid Oxide Fuel Cells" in *Proceedings of the ASME 2021 International Mechanical Engineering Congress & Exposition (IMECE 2021)* (2021).

A. R. Hartwell, J. Ahn, "Integration of Novel Geometry Solid Oxide Fuel Cells into a Residential Furnace/Boiler" in *Proceedings of the ASME 2020 Power Conference (Power 2020)* (2020).

A. M. Willsey, **A. R. Hartwell,** T. S. Welles, D. Park, P. D. Ronney, J. Ahn, "Investigation of Mycelium Growth Network as A Thermal Transpiration Membrane for Thermal Transpiration Based Pumping and Power Generation" in *Proceedings of the ASME 2020 Power Conference (POWER 2020)* (2020), vols. 2020-August.

M. Chu, **A. R. Hartwell,** T.S. Welles, J. Ahn, "Flame-Assisted Fuel Cell Boiler for Combined Heating and Micro-Power Generation" in *Proceeding of the 16th International Conference on Flow Dynamics* (2019), vol. 28.

A. R. Hartwell, J. Ahn, "Development of An Anode Supported Tubular Solid Oxide Fuel Cell with Internal Cathode" in *Proceedings of the 16th International Conference on Flow Dynamics* (2019), vol. 16.

CONFERENCE PRESENTATIONS AND POSTERS

A. R. Hartwell, S. K. Elsayed, Z. Qin, J. Ahn, "Using Simulation and Experiment to Develop a Design Methodology for Self-Shaping Solid Oxide Fuel Cell Multilayer Ceramic Composites" ASME 2023 POWER Conference, Long Beach, CA, August 2023, *in preparation.*

A. R. Hartwell, S. K. Elsayed, Z. Qin, J. Ahn, "Ceramic Origami: Utilizing Bilayer Shrinkage to Form Intricate 3D Ceramic Objects" 2023 Engineering and Computer Science Research Day, Syracuse, NY, March 2023: ***1st place of Oral Competition.***

A. R. Hartwell, "Retrofitting Boilers with Solid Oxide Fuel Cell Stacks to Improve Efficiency and Reduce Emissions" 2023 New York State Green Building Conference, Syracuse, NY, March 2023: ***1st place of Poster Competition***.

A. R. Hartwell, C. VanNostrand, H. Kayton, Y. Murakami, H. Yakamura, J. Ahn, "Internal Cathode Tubular Solid Oxide Fuel Cell Operating on Simulated Two-Stroke Internal Combustion Engine Exhaust" Nineteenth International Conference on Flow Dynamics, Virtual, November 2022.

A. R. Hartwell, J. Ahn, "Utilizing Bilayer Shrinkage to Assemble Complex Ceramic Shapes" ASME International Mechanical Engineering Congress and Exposition (IMECE), Columbus, OH, in preparation, November 2022.

A. R. Hartwell, J. Ahn, "Internal Cathode Tubular Solid Oxide Fuel Cell Operating on Model Combustion Exhaust" 2022 ASME Power Conference, Pittsburgh, PA, July 2022.

A. R. Hartwell, J. Ahn, "Introduction of a Multilayered Cathode for Improved Internal Cathode Tubular Solid Oxide Fuel Cell Performance", Research Day, Syracuse, NY, March 2022: ***3rd place of Poster Competition***.

A. R. Hartwell, J. Ahn, "Complex Material Behavior Seen With Novel Internal Cathode Tubular Solid Oxide Fuel Cells" ASME International Mechanical Engineering Congress and Exposition (IMECE), Virtual, November 2021.

N. P. Slabaugh, **A. R. Hartwell**, T. S. Welles, J. Ahn, "Self-Bending Bi-Layer Ceramics for Use in Solid Oxide Fuel Cells", SOURCE: Summer Research Symposium, Syracuse, NY, August 2021.

K. E. Fields, T. S. Welles, **A. R. Hartwell**, J. Ahn, "Ambient Electromagnetic Radiation Inducing Corrosion of Biocompatible Hip Implants", SOURCE: Summer Research Symposium, Syracuse, NY, August 2021.

A. R. Hartwell, J. Ahn, "Development of Inside Out Solid Oxide Fuel Cells for Combined Heat and Power Systems", Research Day, Syracuse, NY, March 2021: ***2nd place of Energy, Environment and Smart Materials***.

A. R. Hartwell, J. Ahn, "Turning Fuel Cells Inside Out and The Chaos that Ensues", Research Day, Syracuse, NY, November 2020.

A. R. Hartwell, J. Ahn, "Turning Trash and Poop into Power: Novel Geometry Solid Oxide Fuel Cells", Research Day, Syracuse, NY, November 2020: ***3rd place of Student Pitch Competition***.

A. M. Willsey, **A. R. Hartwell,** T. S. Welles, D. Park, P. D. Ronney, J. Ahn, "Investigation of Mycelium Growth Network as A Thermal Transpiration Membrane for Thermal Transpiration Based Pumping and Power Generation" 2020 ASME Power Conference, Virtual, August 2020.

A. R. Hartwell, J. Ahn, "Integration of Novel Geometry Solid Oxide Fuel Cells into a Residential Furnace/Boiler" 2020 ASME Power Conference, Virtual, August 2020.

A. R. Hartwell, J. Ahn, "Development of An Anode Supported Tubular Solid Oxide Fuel Cell with Internal Cathode" The 16th International Conference on Flow Dynamics, Sendai, Japan, November 2019.

M. Chu, **A. R. Hartwell,** T.S. Welles, J. Ahn, "Flame-Assisted Fuel Cell Boiler for Combined Heating and Micro-Power Generation" The 16th International Conference on Flow Dynamics, Sendai, Japan, November 2019.

A. R. Hartwell, H. E. Khalifa, J. Ahn, "High Efficiency Combined Heat and Power Generation System", 17th Annual New York Green Building Conference, Syracuse, NY, October 2019.

A. R. Hartwell, J. Ahn, "Development of a Molten Antimony Solid Oxide Fuel Cell", The 7th International Building Physics Conference, Syracuse, NY, September 2018.

A. R. Hartwell, Y. Timounay, J. D. Paulsen, "Wrinkling of a Curved Ultrathin Film on a Flat Liquid Surface", American Physical Society March Meeting, Los Angeles, CA, March 2018.

A. R. Hartwell, Y. Timounay, J. D. Paulsen, "Wrinkling of a Curved Ultrathin Film on a Flat Liquid Surface", Council on Undergraduate Research Symposium, Alexandria, VA, October 2017.

A. R. Hartwell, Y. Timounay, J. D. Paulsen, "Wrinkling of a Curved Ultrathin Film on a Flat Liquid Surface", Syracuse University Research for Undergraduates Summer Symposium, Syracuse, NY, August 2017.

A. R. Hartwell, "Development and Manufacturing of a Synthetic Blood Brain Barrier", State University of New York/City University of New York Sponsored Research and Creative Works Poster Symposium, Albany NY, January 2016.